Ground-penetrating radar imaging of depositional and diagenetic features in an Upper Miocene carbonate reservoir analog, SE Spain

by

Katharine Marie Knoph
B.S., Lake Superior State University, 2009

Submitted to the graduate degree program in Geology
and the Graduate Faculty of the University of Kansas
in partial fulfillment of the requirements for the degree of
Master of Science

_____
Dr. George Tsoflias, Co-chairperson

_____
Dr. Evan Franseen, Co-chairperson

_____
Dr. Bob Goldstein, Co-chairperson

Date defended: _____

The Thesis Committee for Katharine Marie Knoph certifies
that this is the approved version of the following thesis:

Ground-penetrating radar imaging of depositional and diagenetic features in an Upper Miocene carbonate reservoir analog, SE Spain

Committee:

_____
Dr. George Tsoflias, Co-chairperson

_____
Dr. Evan Franseen, Co-chairperson

_____
Dr. Bob Goldstein, Co-chairperson

Date approved: _____

ABSTRACT

Optimal hydrocarbon recovery from microbialite-oolite reservoirs can be limited by complex facies geometries and porosity distribution. This study integrates ground-penetrating radar (GPR) and detailed outcrop data for 3D mapping of porosity distribution and stratigraphic architecture within Upper Miocene microbialite-oolite sequences (Terminal Carbonate Complex) of southeastern Spain.

Twenty kilometers of 2D and 3D GPR data of differing frequencies (25, 50, and 100 MHz) were acquired throughout the survey site, an area approximately 400 m x 300 m. Two-dimensional GPR profiles were collected along a grid covering the entire survey area, allowing imaging of depositional and diagenetic variability over a broad area. Two densely spaced 3D grids allow further detailed characterization and comparison of paleotopographic high and low areas.

Results of this study illustrate that GPR can image stratigraphic features such as sequence boundaries and tight thrombolite bodies. Reflections are primarily influenced by porosity variations within the strata. Three of the GPR facies, recognized on the basis of reflection signatures (strong, weak, or no internal reflections), are linked predominantly to porosity variations in facies. Each GPR facies has been identified and delineated in each frequency data set. GPR facies distribution illustrates a large-scale trend of lower porosity in the updip portion of the survey area.

GPR successfully imaged some depositional features (i.e., sequence boundaries and some thrombolites), however, in many instances, reflections correlate to variations in porosity that vary laterally and vertically on a several-meter scale in 3D and commonly cut across sequence boundaries. The abrupt lateral changes in GPR character are inconsistent with their being controlled by depositional processes; instead diagenesis and potentially fractures appear to strongly influence GPR signal. These observations indicate that porosity characteristics in the study area are associated with both depositional and diagenetic processes. Although GPR has traditionally been used to image stratigraphic features, these results indicate GPR can be important for imaging diagenetic features as well. As such, GPR can be a valuable tool for imaging porosity heterogeneity and developing conceptual models that portray 3D variations in both stratigraphy and porosity. Resultant insights may be important for comprehensive understanding of porosity development and distribution in this system and subsurface carbonate reservoir analogs.

ACKNOWLEDGEMENTS

Support for this project was provided by the Geophysical Society of Kansas (GSKS), the AAPG Foundation, the SEPM Foundation, the Society of Independent Earth Scientists (SIPES) Foundation, the Kansas Geological Foundation (KGF), the University of Kansas, The Kansas Geological Survey (KGS), Haas Professorship, Chevron, Hess, and ExxonMobil FC^2. I would like to thank Matt Baker, KU graduate student, for assistance in data collection and Dr. Mike Taylor, KU, for providing the DGPS instrumentation. Also, I would like to thank my advisors, Drs. Bob Goldstein, Evan Franseen, and George Tsoflias, for their guidance and support throughout the project. Thanks as well to Dr. Gene Rankey for input and insights at key points in this study. Most of all, I would like my family, especially my parents, for their incredible and continual support throughout my life. All of my success can be attributed to them for giving me the best upbringing imaginable and teaching me to have strong values including a good work ethic, honesty, and fortitude. Thank you so much, I am forever grateful.

TABLE OF CONTENTS

LIST OF FIGURES AND TABLES

FIGURES

TABLES

CHAPTER 1: INTRODUCTION

Successful exploration and production from subsurface reservoirs requires understanding of complex facies geometries and porosity that are influenced by a combination of depositional and diagenetic processes. Commonly, subsurface geologic data are derived primarily from seismic reflection surveys and wells. Industry seismic reflection surveys typically image features greater than 10 m in thickness and at least 10s of meters across (Berkhout, 1984; Sheriff, 1997; Yilmaz, 2001), whereas wells provide detailed information on vertical changes, but from only a small radius around the wellbore. To complement these types of data, outcrop analog studies have facilitated recognition of small-scale vertical and lateral changes that may not be detected in seismic or well data, but can be important for reservoir characterization and effective hydrocarbon recovery. Subsurface reservoirs, however, require prediction in three-dimensions (3D), information that commonly cannot be obtained from outcrop investigations alone. Integration of ground-penetrating radar (GPR) and outcrop data provides a unique opportunity to extend outcrop studies into the third dimension, ultimately improving understanding of stratigraphic architecture and porosity distribution. Furthermore, high-resolution data, such as GPR data obtained in this study, can be important for understanding the nature and controls on reservoir architecture. This is especially true for understanding reservoirs with complex stratal geometries and diagenetic patterns that may strongly influence characteristics of reservoirs (Watney, 1980; Knight et al., 1997).

Ground-penetrating radar (GPR) has been used widely as a tool for investigating characteristics of the shallow subsurface. Geologic applications of GPR include aquifer

fluid-flow modeling, pollution detection and mapping, fracture detection (Grasmueck et al., 2004), active faults and sinkhole hazard detection (Reicherter and Reiss, 2001). The foci of geologic studies range from revealing the internal stratigraphy of ancient (Bristow et al., 2007) and active dunes (Hugenholtz et al., 2007), lacustrine deltas (Stevens and Robinson, 2007), and paleovalley fill (Hickin et al., 2007; Rother et al., 2007) to characterization of siliciclastic (Corbeanu et al., 2001, Zeng et al., 2004) and carbonate reservoir analogs (Pratt and Miall, 1993; Aspiron and Aigner, 2000; Grasmuek and Weger, 2002; Dagallier et al., 2000; Aspiron et al., 2009; Jorry and Bievre, 2011). Over the past decade, numerous GPR surveys have complemented outcrop studies (e.g. Pratt and Miall, 1993; Franseen et al., 1997a; Martinez et al., 1998; Nielson et al., 2004; Van den Bril et al., 2007; Jorry and Bievre, 2011) by extending stratal information beyond outcrop faces and improving understanding of stratigraphic architecture in three-dimensions. Although variations in porosity have been theorized to cause reflections in some studies (Rust and Russell, 2001; Franseen et al., 2007; Van den Bril et al., 2007; Jorry and Bievre, 2011), imaging of porosity distribution in carbonate successions utilizing GPR has not been the primary focus of many studies.

In this context, the purpose of this study is to develop an understanding of 3D distribution of porosity and depositional facies at several scales in a microbialite-oolite reservoir analog (Upper Miocene Terminal Carbonate Complex, TCC; La Molata, Spain) through the integration of multi-frequency GPR and outcrop data. The study area is ideal for a GPR survey due to excellent exposures surrounding the entire survey area, the dry climate of the area and the simple mineralogy of the succession. This study explores three fundamental questions: 1) What is the nature of variability in GPR signal? 2) How

does reflection character relate to depositional and diagenetic features? 3) Do GPR data reveal geologic trends within each frequency and across several spatial scales?

To address these questions, twenty kilometers of GPR data of three frequencies (25, 50, and 100 MHz) were acquired throughout a survey site (12,000 m^2). Profiles adjacent to well-exposed, near-vertical outcrops allow comparison of GPR data with depositional facies and rock fabrics. Two-dimensional (2D) GPR profiles from a grid (line spacing of 20 m) covering the entire survey area facilitate imaging of 3D facies geometries and porosity distribution over a broad area. Nested within the 2D grid are two smaller densely spaced grids with 5 m line spacing that permit further detailed characterization and comparison of specific areas of interest.

Results illustrate that some GPR reflections correlate to depositional features such as sequence boundaries. The majority of reflections, however, are caused by variations in porosity that may, or may not, correspond to depositional features. Distinct GPR facies defined on the basis of reflection signatures (strong, weak, or no internal reflections) correlate predominantly to porosity variations within depositional facies, but most GPR facies are not uniquely indicative of one depositional facies. In many instances, GPR facies cut across stratigraphy, and can be related to diagenetic processes affecting porosity. Therefore, GPR data capture porosity characteristics associated with both depositional and diagenetic processes. As such, GPR can be a valuable tool for imaging porosity heterogeneity in carbonate systems and developing conceptual and quantitative models that portray variations in stratigraphy and porosity in 3D. Resultant insights may be important for comprehensive understanding of porosity development and distribution in this system and subsurface carbonate reservoir analogs.

CHAPTER 2: GEOLOGIC SETTING

The western Mediterranean region was characterized by North-South (N-S) compression that began in the Cretaceous as the African plate collided with the Iberian plate to the North (Rehault et al., 1985). This N-S compression continued until approximately 9 Ma (Sanz de Galdeano and Vera, 1992), when rotation of the African plate caused a change in direction of compression to NW-SE. The change in direction of compression led to transtensional deformation of the region, leading to formation of strike-slip faults and pull-apart basins and extrusion of volcanics (Rehault et al., 1985; Montadert et al., 1978; Sanz de Galdeano and Vera, 1992).

The study site is located in southeastern Spain in the Cabo de Gata region near the coastal village of Las Negras, on the southern margin of the Almeria Basin (Figure 2.1). A major sinistral strike-slip fault, the Carboneras Fault, lies to the northwest and separates the Neogene volcanic basement of the Cabo de Gata region from the Mesozoic-Paleozoic metamorphic basement of the Betic Cordillera (Lopez-Ruiz and Rodriguez-Badiola, 1980; Montenant et al., 1987; Montenant and Ott D'Estevou, 1990; Serrano, 1992).

The volcanic basement, dated at 17 to 6 Ma (Lopez-Ruiz and Rodriguez-Badiola, 1980; Serrano, 1992) formed an archipelago in the Cabo de Gata region during the Middle to Late Miocene (Esteban and Giner, 1980; Esteban, 1996). The complex topography of the volcanic basement, on which carbonates were deposited, was likely a combined result of subaerial and marine erosion, faulting and original volcanic topography (Esteban, 1979; Esteban and Giner, 1980; Sanz de Galdeano and Vera, 1992;

Esteban, 1996; Franseen et al., 1998). In the study area, the basement consists of isolated volcanic highs that formed in association with development of the approximately 11 million year old Rodalquilar caldera (Rytuba et al., 1990). Carbonate production occurred predominantly on the flanks of local volcanic highs and accumulated on the flanks, or in interconnected basins, paleovalleys and straits of the archipelago (Esteban and Giner, 1980; Sanz de Galdeano and Vera, 1992; Esteban, 1996; Johnson et al., 2005).

Volcanic activity predated deposition of the stratigraphic units on which this study is focused (Franseen et al., 2003). Locally, the youngest volcanic rocks yield an $^{40}Ar/^{39}Ar$ date of 8.5±0.1 Ma (Goldstein and Franseen, 1995; Franseen and Goldstein, 1996; Franseen et al., 1998).

Previous studies have documented the Miocene exposures of the study area (Esteban and Giner 1980; Franseen and Mankiewicz 1991; Franseen et al. 1993; Esteban et al., 1996; Franseen et al., 1998; Johnson et al., 2005; Lipinski, 2009). The carbonate strata in the field area are divided into 5 depositional sequences (Figure 2.2) controlled by 3rd-to 4th-order scale relative changes in sea-level, with higher frequency events superimposed (Franseen et al., 1993, 1998).

The Terminal Carbonate Complex (TCC; Esteban, 1979) is the uppermost sequence and the focus of this study. It overlies an unconformity that caps DS3, a photozoan reef complex. The unconformity represents a significant relative fall in sea level thought to be the landward expression of the Messinian Salinity Crisis, in which a thick sequence of evaporites were deposited in the Mediterranean basin due to relative sea level fall, lack of a deep connection to the Atlantic Ocean, and intense evaporation (Esteban, 1979; Esteban and Giner, 1980; Dabrio et al., 1981; Martin et al., 2003; Martin and Braga, 1994;

Franseen et al., 1997). Significant erosional topography formed on the unconformity before deposition of the TCC (Franseen et al., 1993; Goldstein and Franseen, 1995; Lipinski, 2009).

After deposition of evaporites in the Mediterranean Basin, major flooding of basin margins resulted in deposition of the TCC, the uppermost Miocene sequence, along the basin margins (Dronkert, 1976; Esteban and Giner, 1980; Dabrio et al., 1981; Riding et al., 1991; Franseen et al., 1993; Braga et al., 1995; Franseen et al., 1998). The TCC is composed of microbialite and oolite-dominated strata (with local photozoan reefs). Exposures in the study area contain four carbonate sequences that drape paleotopography on the underlying unconformity. The four sequences were deposited in association with high-amplitude (greater than 50-80 m), high-frequency glacioeustatic changes (Lipinski, 2009). Each sequence displays similar cyclic patterns of deposition (Franseen et al., 1993; Goldstein and Franseen, 1995; Lipinski, 2009). A detailed description of the stratigraphy of each of the four sequences comprising the TCC is provided in the section below.

Following deposition of the TCC, the Strait of Gibraltar opened and local Pliocene marine deposition took place in marginal basins nearest the Mediterranean Sea (Esteban and Giner, 1980; Esteban, 1996; Franseen et al., 2010). Broad uplift in the Pliocene and later resulted in the definitive withdrawal of the sea from the coastal marginal basins (Esteban and Giner, 1980; Sanz de Galdeano and Vera, 1992, Esteban, 1996).

Although there has been uplift, the rocks in the area of study internally have not been deformed significantly, as evidenced by numerous preserved horizontal geopetal

fabrics, geometries of strata, regional mapping, and the small amount of displacement (less than a few meters) along most faults (Esteban and Giner, 1980; Franseen, 1989; Franseen and Mankiewicz, 1991; Franseen and Goldstein, 1996; Lipinski, 2009). Thus, present-day outcrops largely preserve Miocene paleotopography, allowing a unique opportunity to evaluate the role of paleotopography on depositional and post-depositional processes (Franseen and Mankiewicz, 1991; Franseen et al., 1993).

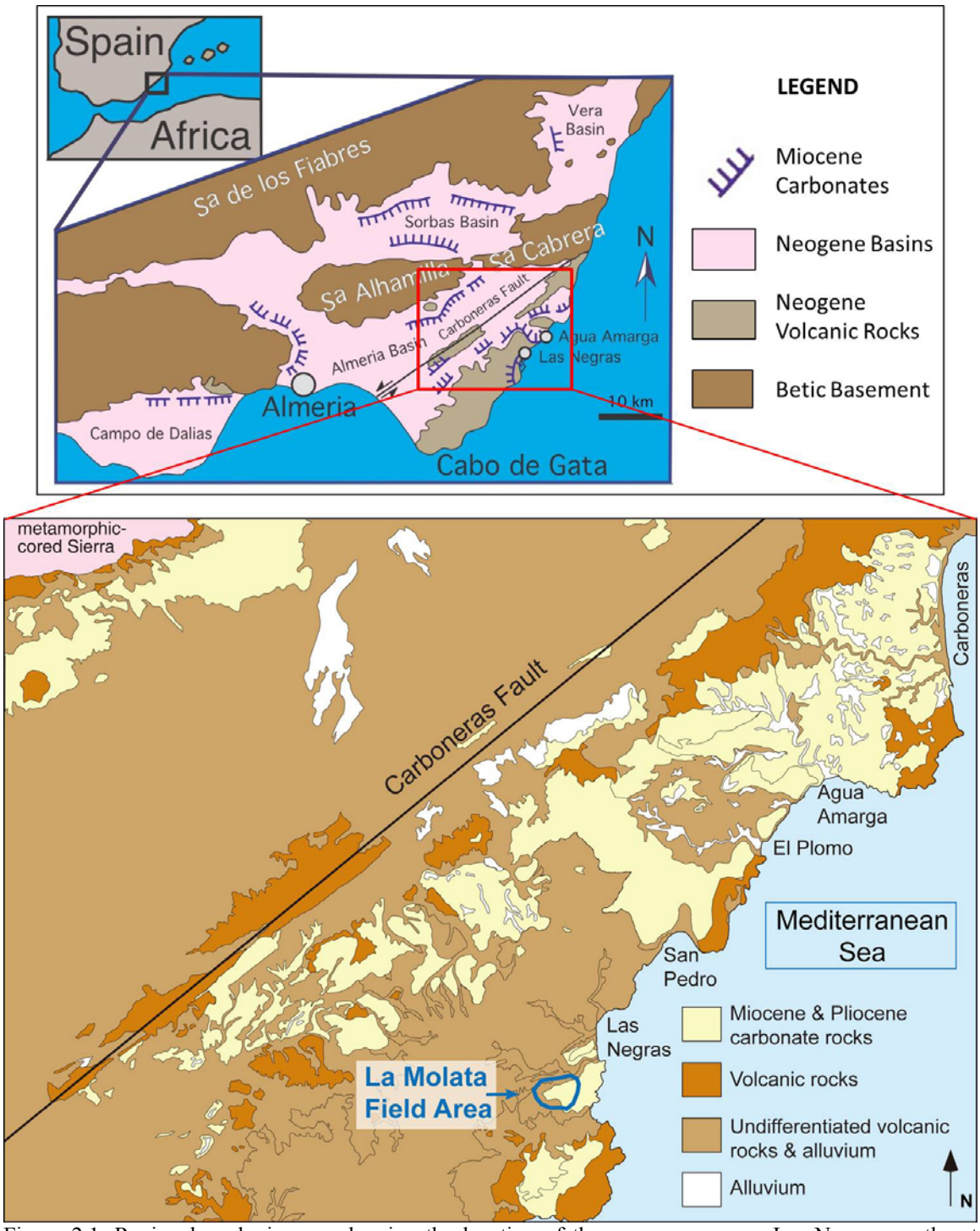

Figure 2.1. Regional geologic map showing the location of the survey area near Las Negras, southeast Spain. The field site, La Molata, is outlined in blue. Modified from Franseen et al. (1998).

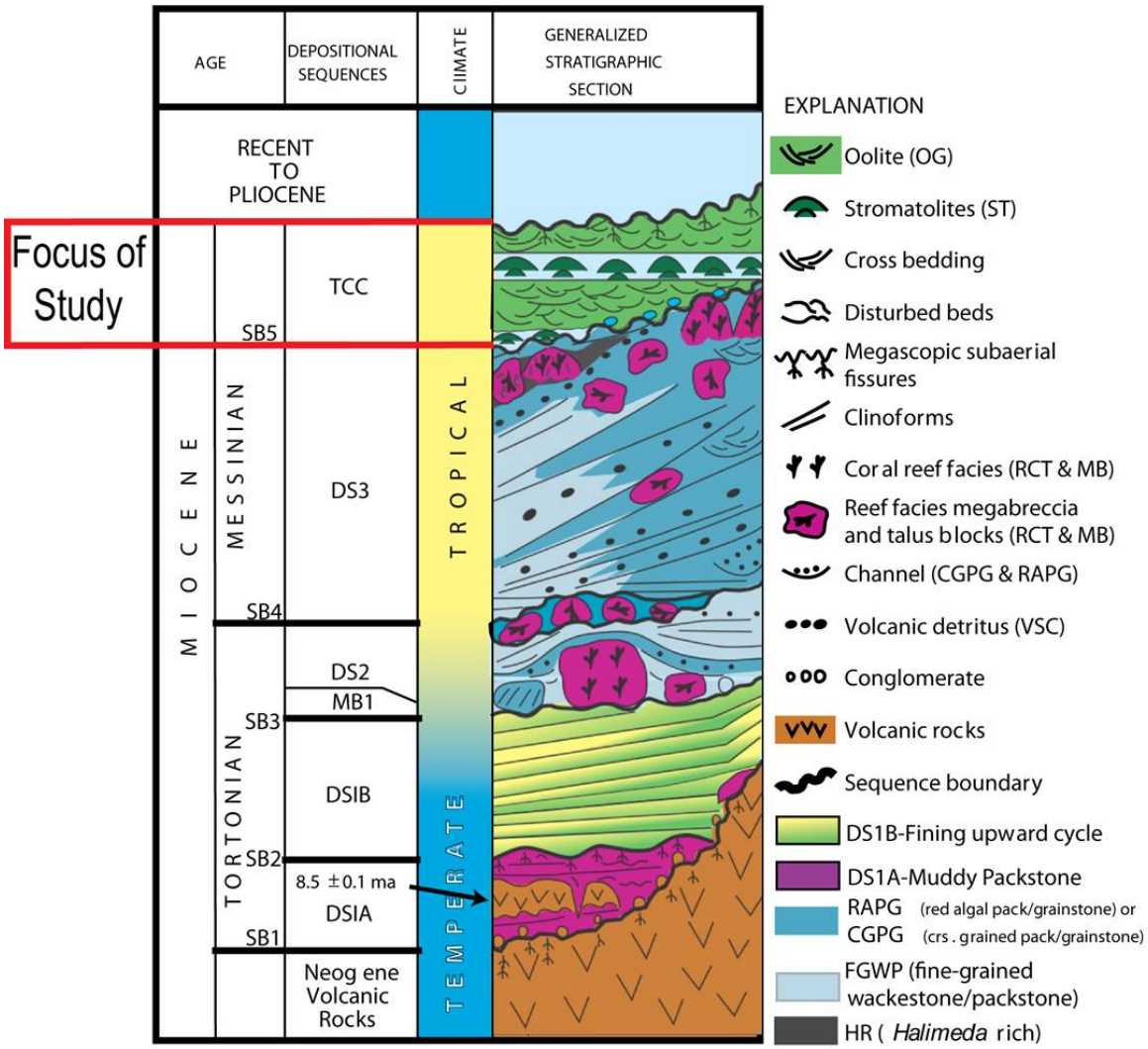

Figure 2.2. General stratigraphic section of the Las Negras Area with the TCC, the focus interval of this study, highlighted in red. A change from heterozoan-dominated facies (DS1A and DS1B) to later photozoan-dominated facies indicates a change in climate from temperate to tropical. The TCC forms a capping succession consisting primarily of microbialites and oolites that compose the last unit deposited in the Miocene. Modified from Franseen et al. (1996).

CHAPTER 3: STRATIGRAPHIC ARCHITECTURE

The TCC is composed of four carbonate sequences that are primarily made up of oolites and thrombolites (unstratified microbial buildups) that were deposited in association with high-amplitude, high-frequency glacioeustatic changes (Figure 3.1) (Esteban, 1996; Franseen et al., 1998; Brachert et al., 1998). The sequences include evidence of restricted and normal marine environments (Dronkert, 1976; Rouchy and Saint Martin, 1992; Franseen et al., 1993; Franseen and Goldstein, 1996). Each is relatively thin (ranging from 1.3 m to 12.8 m, with an average thickness of 4 m to 8 m in most places). Typically, sequences drape paleotopography and exhibit similar attitude at any one location (Franseen et al., 1998; Lipinski, 2009). The total thickness of the TCC at the La Molata field site is approximately 30 m.

The paleotopography onto which the TCC was deposited on a surface sloping gently to the east (Figure 3.3). The highest point in the northwest portion of the survey area is 208 m and the elevation drops approximately 30 m to the east. Instead of a uniformly dipping surface, two paleovalleys are present in the eastern part of the survey area.

Each of the four sequences, which will be referred to hereafter as Sequences 1 (stratigraphically lowest) through 4 (stratigraphically highest), displays similar character. The sequences can be considered cyclical when examined vertically as each sequence typically begins with a stromatolitic unit at its base overlain by local thrombolite deposits followed by trough cross-bedded ooid grainstones. The trough cross-bedded ooid grainstone deposits in many instances are interbedded with thrombolite deposits and fill

in areas between individual thrombolites. Planar bedded ooid grainstones containing volcanic rock fragments comprise the uppermost portions of each sequence. The uppermost meter of the sequences commonly displays evidence of subaerial exposure in the form of fenestral fabric, alveolar textures, fissures, caliche-coated grains, micritized grains, truncated grains, laminated crusts, and pendant micrite cements (Franseen et al., 1993; Whitesell, 1995; Goldstein and Franseen, 2005; Lipinski, 2009; Z. Li, personal communication, 2011). Ongoing dissertation research by Zhaoqi Li, University of Kansas, also reveals further evidence of subaerial exposure by the presence of abundant fenestrae, meniscus cements as well as rhizoliths (Z. Li personal communication, 2011). In addition to vertical cyclic heterogeneity, a great deal of lateral variability is present. For example, Lipinski (2009) found that at low elevations, thrombolite boundstones are thicker and more laterally continuous than at higher elevations.

As the focus of this study was not on unraveling stratigraphic history, this study leverages the previous studies that have carefully examined the sedimentologic and stratigraphic character of each of the four TCC sequences (Franseen et al., 1993; Whitesell, 1995; Lipinski, 2009). These studies indicate the following characteristics of each sequence, and their general interpretations (see Lipinski (2009) for more detailed descriptions). Although the TCC contains four sequences, only the upper two sequences are described below as they were the focus of this study due to limitations of the depth of penetration of the GPR.

Sequence 3

Sequence 3 is the thickest of the sequences, ranging from 6.3 to 12.8 m (Figures 3.1, 3.2; Lipinski, 2009). It is present throughout the La Molata survey area. Basal

stromatolite deposits of this sequence commonly range from 5 to 15 cm in thickness (but can reach 20 to 30 cm thickness in a few rare instances), although they are discontinuous throughout the survey site. Thrombolite boundstone is not common in this sequence, and where present, forms small, isolated mounds approximately 1 m wide by 1 m thick. The boundaries between the thrombolites and the overlying ooid grainstone are generally sharp, rather than interfingered, as in many of the other sequences. Ooid grainstone comprises the majority of Sequence 3, and is more massive in the lower parts of the sequence and grades upward into trough cross-bedded ooid grainstone. Within the trough cross-bedded ooid grainstone, rare, isolated *Porites* boundstone reef patches approximately 1 m high by 1 m wide are present. Volcaniclastic-rich planar bedded ooid grainstone comprises the uppermost portion of the sequence. In a few areas, fenestral ooid grainstone caps the sequence.

Sequence 4

Sequence 4 is present only in the lower elevations along the eastern half of the survey area and is likely not preserved in its entirety in any location (Figures 3.1, 3.2; Lipinski, 2009). The thickest part of Sequence 4 in the study area is 6.2 m. The basal stromatolite layer of Sequence 4 is the most continuous stromatolite of the four sequences. It is approximately 10 to 15 cm thick in most areas, but reaches a maximum thickness of 40 cm in some places, and is present throughout most of the survey area. The stromatolite commonly is overlain by discontinuous thrombolite boundstone bodies. These units can extend laterally 10s of m, but can also occur as isolated bodies less than 2 to 3 m wide. The preserved thickness of the thrombolite units reaches up to 4 m, and they can comprise most of the sequence. Overlying the thrombolite is cross-bedded ooid

grainstone containing gastropod fragments in places. The boundary between the thrombolite bodies and the overlying ooid grainstone is sharp in some locations and gradational in others.

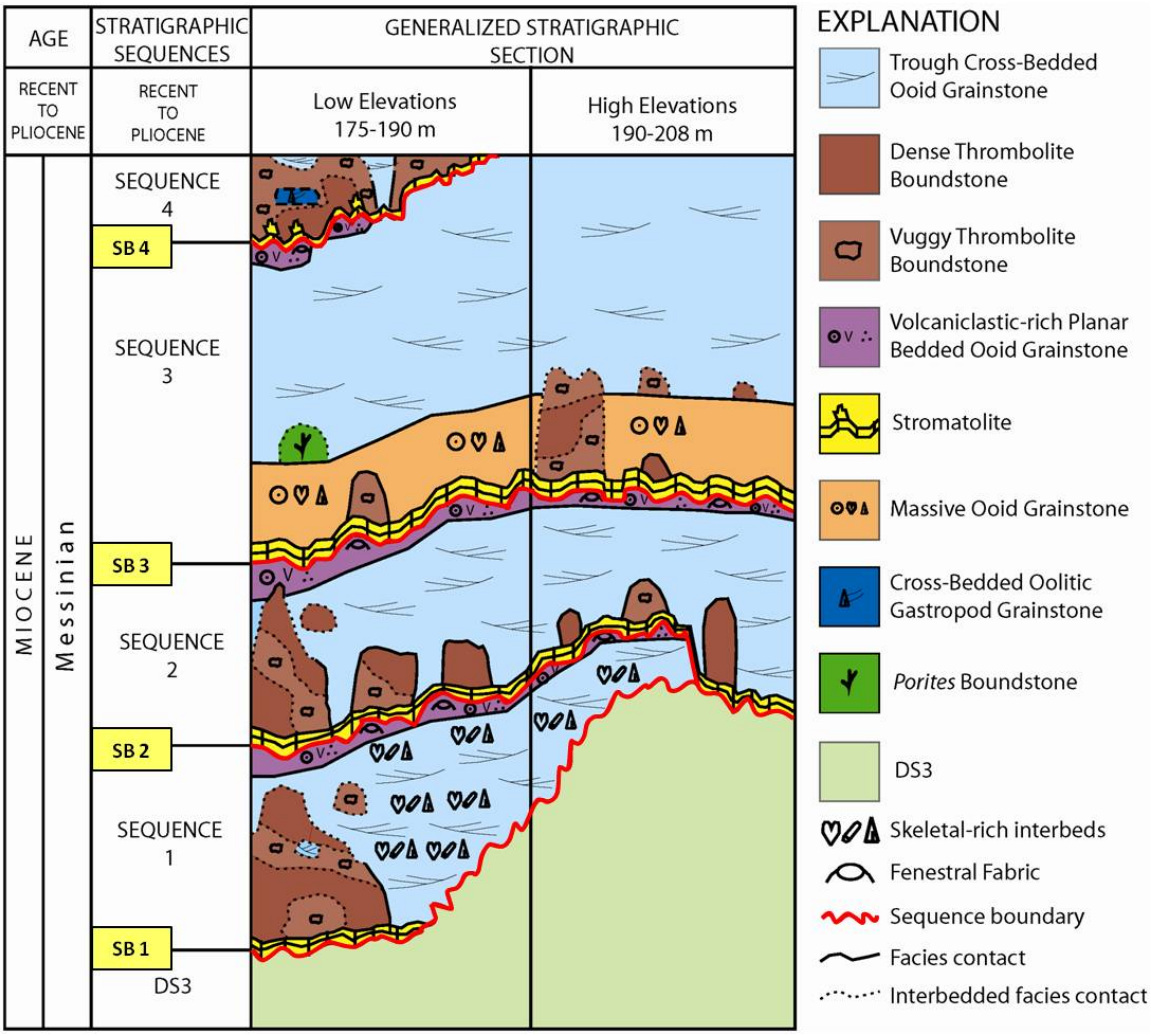

Figure 3.1. General stratigraphic sections of the TCC of La Molata displaying lithofacies variability with changes in paleotopography. At intermediate elevations, sequences have a build-and-fill architecture (Franseen and Goldstein, 2004; Franseen et al., 2007b), characterized by a relief-building phase followed by a relief-filling phase, with the relatively thin sequences draping paleotopography. Microbialites, primarily thrombolites, are more abundant at lower elevations than higher elevations, and have been interpreted to dominate deposition during relative rises in sea level. In contrast, ooid grainstone filled in topographic relief during relative falls in sea level. The alternating building-and-filling phases are the most probable explanation for the development of the thin, topography-draping sequences found at the study site. Note SB denotes the positions of sequence boundaries 1 through 4. Modified from Lipinski (2009).

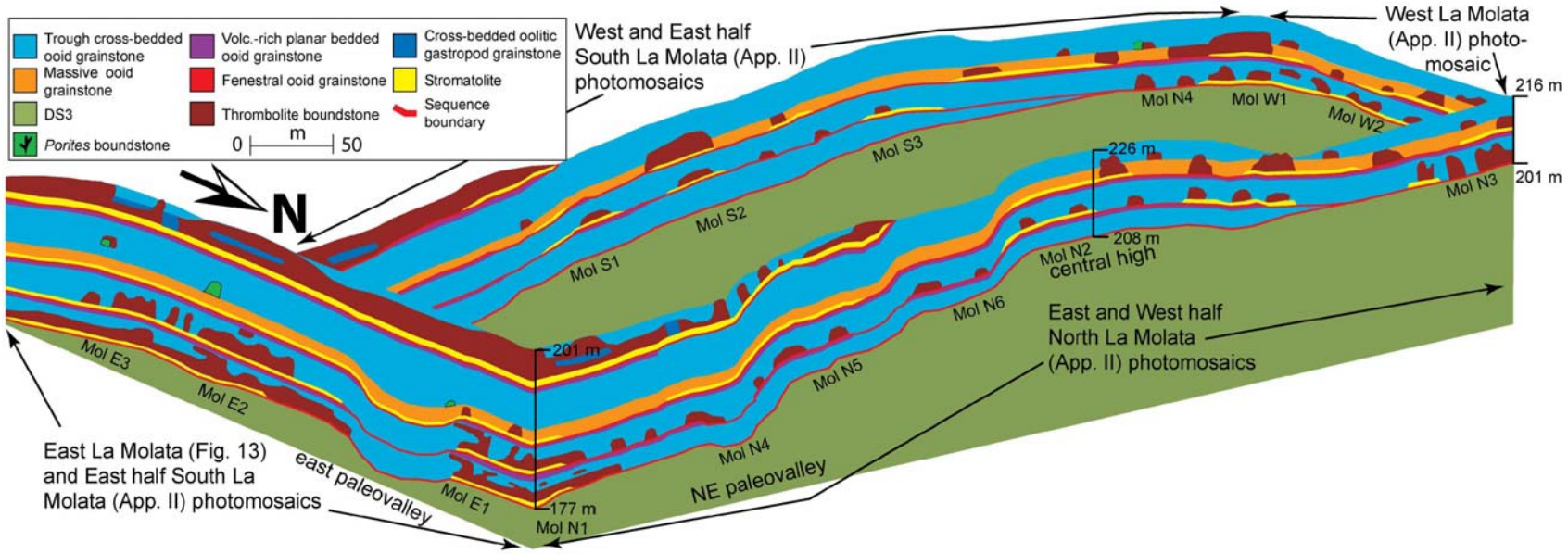

Figure 3.2. Fence diagram for the La Molata Field area displaying the distribution and geometries of lithofacies. Sequences drape and locally onlap paleotopography and maintain relatively uniform thickness across the area. Oolites are volumetrically the most abundant lithofacies. Thrombolite boundstones are laterally extensive and thicker at the low elevations. Stromatolites are laterally more extensive at the low elevations (Lipinski, 2009).

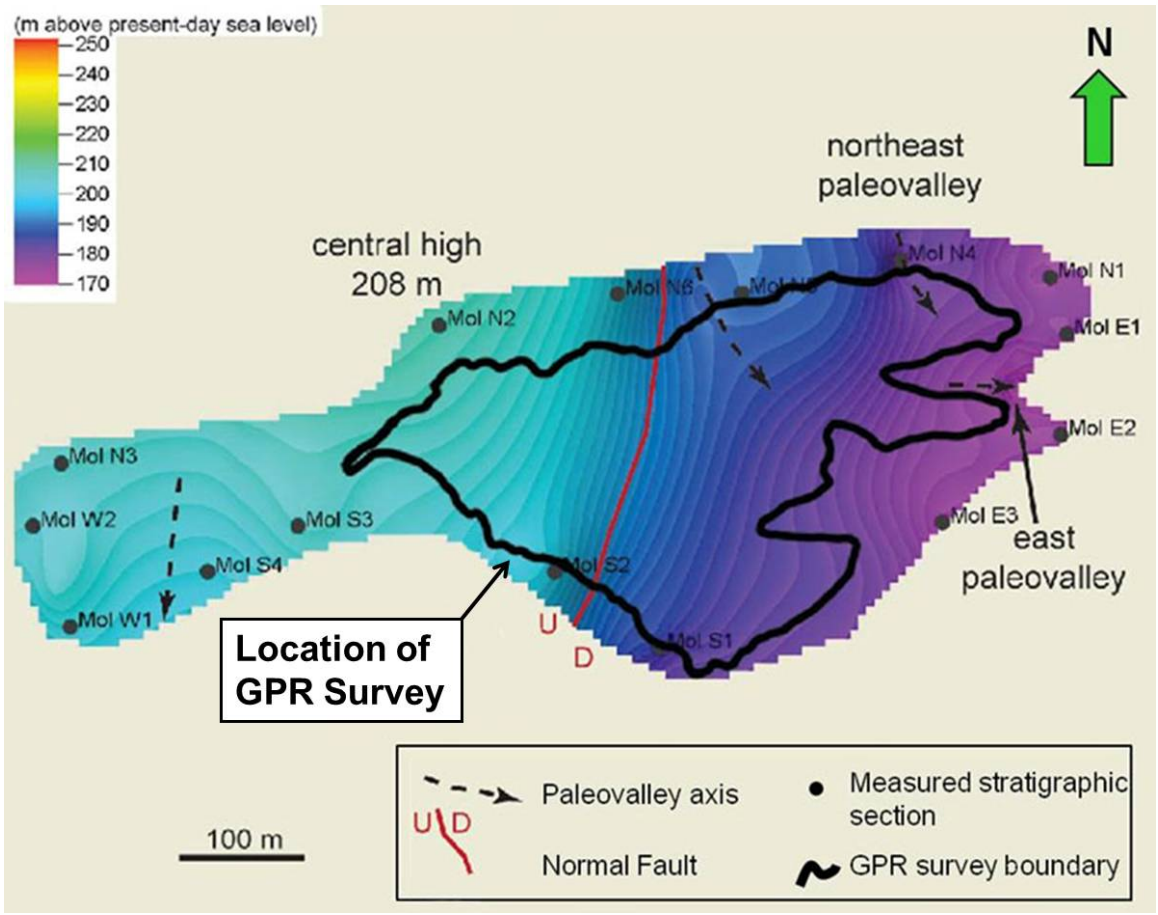

Figure 3.3. Paleotopographic basement map of the surface on which the TCC was deposited. This map was generated from measured sections along the perimeter of the survey area. Notice the central high point of 208 m along the northern boundary and the gradual decrease in elevation of approximately 30 m to the east and southeast. The location of the GPR survey is outlined in black. Modified from Lipinski (2009).

CHAPTER 4: METHODS

Fieldwork was conducted at La Molata from May to June in the summer of 2010 and included collection of nearly 20 km of GPR data, detailed description of outcrops and collection of 72 hand samples for thin section analysis. Processing of the GPR data was carried out immediately upon return (summer and fall of 2010) and included the application of temporal and spatial filters, migration, gain and topographic corrections. Following processing, resolution of the three different frequencies was determined and outcrop data, hand samples and thin sections were analyzed and used to calibrate the GPR data. In this section, a basic overview of the principles of GPR and a description of the survey site is followed by detailed explanations of the methods of data acquisition, processing and calibration to rock samples.

4.1: Principles of Ground-Penetrating Radar

GPR reflection surveys use high-frequency electromagnetic (EM) waves in the range of 10 to 1000 MHz to image the shallow subsurface. Data collection is rapid, non-invasive, and cost effective when compared to other methods of subsurface characterization such as drilling and excavation. Subsurface information, such as sedimentary structures, location of voids, and depth of water table can be determined from the response of EM waves propagating and reflecting in the subsurface (Davis and Annan, 1989; Neal, 2004).

Radar reflections occur at interfaces characterized by contrasting dielectric properties including electrical conductivity, dielectric constant and magnetic permeability (Davis and Annan, 1989; Neal, 2004; Annan, 2005). In geologic media, electrical conductivity is important because it controls the attenuation of radar waves, velocity of

propagation and interface reflectivity (Davis and Annan, 1989; Neal, 2004). Dielectric constant is a critical GPR parameter because it controls the propagation velocity of electromagnetic waves and the reflection coefficients at interfaces (Davis and Annan, 1989; Daniels, 1996; Martinez and Byrnes, 2001; Neal, 2004). For lossless media, the half-space reflection coefficient, R, for a normal incident plane wave is:

$$R = [(\varepsilon_1)^{1/2} - (\varepsilon_2)^{1/2}] / [(\varepsilon_1)^{1/2} + (\varepsilon_2)^{1/2}] \quad (1)$$

where ε_1 is the dielectric constant of the upper medium and ε_2 is the dielectric constant of the lower medium (Davis and Annan, 1989). This equation can be used to determine the strength of reflections at interfaces of media with differing dielectrical properties (i.e. different bulk dielectric constants). In sedimentary rocks, radar reflections commonly are generated as EM waves impinge on bedding planes, which are frequently characterized by variations in lithology, porosity, grain size and orientation or packing of sediment (Van den Bril et al., 2007; Jorry and Bievre, 2011). Carbonate successions that may include rock fabric variations may occur between bedding planes due to both depositional and diagenetic heterogeneity can be even more complex (Budd et al., 2006; Pranter et al., 2006).

Changes in petrophysical properties that may account for varying dielectric properties (and thus differing reflection strengths) can arise from changes in mineralogy or water content. The TCC contains strata composed primarily of limestone and dolomite with very little mineralogic variation. The succession is above the water table with little evidence of major amounts of vadose water. Some stratigraphic units are rich in volcanic rock fragment that have been altered to clay minerals, but these are volumetrically minor.

A final possible influence on GPR signals are changes resulting from variations in medium porosity (discussed below). Previous studies have shown that in areas with little mineralogic variability, contrasts in bulk material dielectric constant may be related to variations in porosity (Rust and Russell, 2001; Van den Bril et al., 2007). Carbonate rock has a bulk dielectric constant of 6-8 measured at 100 MHz; air has a dielectric constant of 1 measured at 100 MHz (Davis and Annan, 1989; Martinez and Byrnes, 2001). Units with varying amounts of porosity above the water table will have different dielectric constants, and, if contrasts are great enough, will generate reflections. Many mixing formulas estimate the dielectric response of heterogeneous media; an overview of these formulas can be found in Shen (1985), Shen et al., (1985) and Greaves et al., (1996). The complex refractive index method (CRIM) is one such example that can be used to relate the dielectric constant of a sample to its porosity. For a heterogeneous medium containing three components (rock, water and air), the bulk dielectric constant, ε_c, can be determined using the following equation developed by Shen (1985):

$$\sqrt{\varepsilon_c} = \phi S_w \sqrt{\varepsilon_w} + (1- \phi)\sqrt{\varepsilon_g} + \phi(1- S_w)\sqrt{\varepsilon_a} \quad (2)$$

where ϕ is sample porosity, S_w is water saturation and $\varepsilon_{w,}$ ε_g and ε_a are the dielectric constants of pore water, dry sample grains and air, respectively. In situations in which water saturation and matrix mineralogy remain the same, porosity is the only factor that causes changes in the bulk dielectric constant, ε_c. The dielectric constant value obtained using this equation can then be inserted into Equation 1 to determine the reflection coefficient. Clay minerals, quartz silt, and residual water, although minor components in volume in the study area compared to air and carbonate, also can provide sufficient dielectric constant contrasts (bulk dielectric constants of clay, silt, and fresh water are 5-

40, 5-30, and 80, respectively; Davis and Annan, 1989) to cause reflections, especially at sequence boundaries in the study area, where altered volcaniclastic sediments are concentrated.

GPR survey resolution (vertical and horizontal) and depth of imaging are related to the frequency and velocity of the EM waves propagating through media (Davis and Annan, 1989; Martinez and Byrnes, 2001). Higher frequencies yield greater resolution but attenuate more rapidly, and therefore they are less effective at imaging with increasing depth. To achieve imaging at several resolution and depth scales, three GPR frequencies (25, 50, and 100 MHz) were collected in this study.

Interpretation of radar data depends on recognition of radar facies that are then interpreted in the context of sedimentology and stratigraphy (Bristow et al., 2000; Bristow and Jol, 2003; Roberts et al., 2003). This study compares radar facies to adjacent, well-exposed outcrops, allowing evaluation of the capability of GPR to image geometries, sedimentary facies, and porosity distribution in three dimensions within the survey area.

4.2: Survey Site Description

The GPR survey was conducted on the present-day upper surface of La Molata, a hill capped by approximately 30 m of the TCC (Figure 4.1). 'La Molata' translates to 'the molar' and as can be seen, the hill resembles a molar tooth. All four sequences of the TCC are preserved at the study site, although erosional truncation has removed part of the upper two sequences in the western part of the area. The survey area is relatively flat, varying only 30 m in elevation over the 400 m by 300 m site. A topographic high is located along the northwestern boundary and elevation gradually decreases to the east

and southeast (Figure 4.2). Present-day topography mimics topography at time of deposition, and has facilitated investigation of paleotopographic influence on depositional and post-depositional processes (Franseen and Mankiewicz, 1991; Franseen et al., 1993).

Well-exposed, near-vertical outcrops around the perimeter of the survey area are critical to interpretation of these GPR data. Correlation of radar signatures to nearby outcrops allow data from the GPR survey to be calibrated to lithology. Further facilitating the utility of the study site for the GPR survey is the gentle topography (Figure 4.2), arid climate and minimal development of soil, all of which contribute to more effective electromagnetic signal penetration.

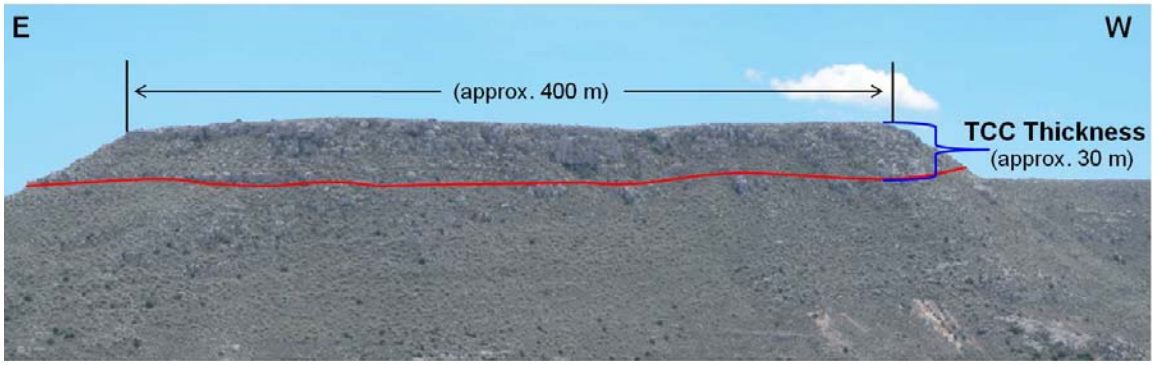

Figure 4.1. La Molata survey area showing the surface on which GPR survey was conducted. The TCC comprises approximately 30 m of the crest of the hill and contains all four sequences in most areas. Photo modified from Lipinski (2009).

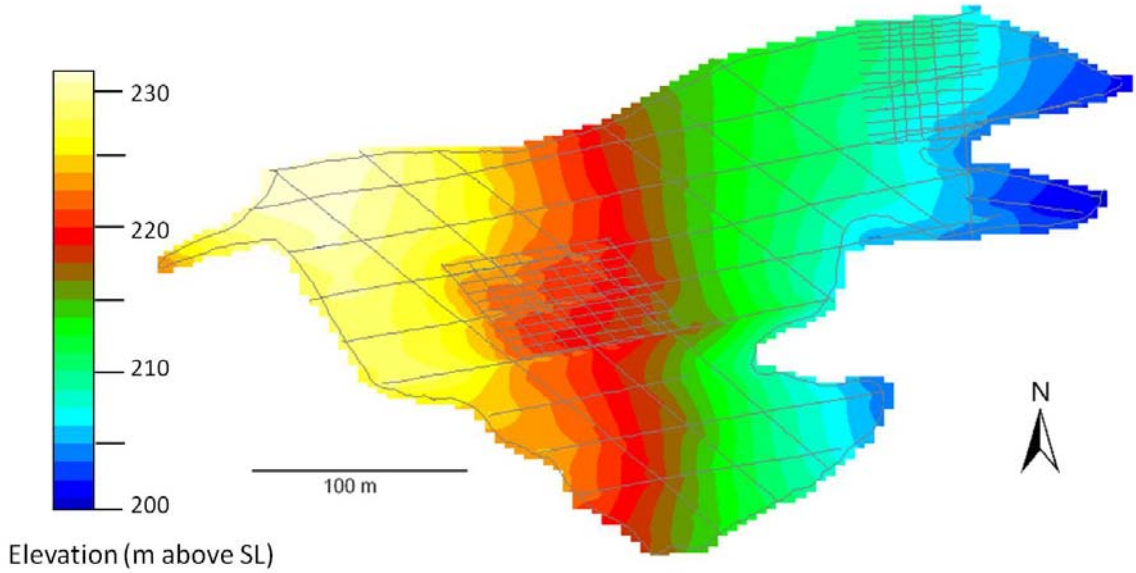

Figure 4.2. Contour map of the present-day topography of the top of La Molata within the survey area. Note the generally flat surface, with only 30 m change in elevation across a lateral distance of approximately 400 m. The relief and slope angle of the modern surface is similar to the paleotopographic basement map of the TCC generated by Lipinski (2009) (Figure 4.2). Similarly, topographic lows on the surface occur in the same locations as the paleovalleys described by Lipinski (2009).

4.3: Data Acquisition

Nearly twenty kilometers of GPR data were acquired at the La Molata field location as 2D and pseudo-3D grids (Figure 4.3). GPR profiles were collected with a Sensors and Software pulseEKKO PRO GPR system, utilizing a 1000 V transmitter and three different sets of antennas with center frequencies of 25, 50 and 100 MHz.

Two-dimensional profiles were collected along the perimeter of the survey area within 1 m to 2 m of well-exposed, near-vertical outcrops bounding the survey area, providing groundtruth for the radar images. Transects were located close enough to the cliffs to provide direct correlation with exposures, but far enough to avoid edge effects. To obtain coverage of the entire survey area, 2D profiles were acquired along a grid with line spacing of approximately 20 m. Profiles of each of the three frequencies were acquired along the perimeter of the survey area along all 2D transects, allowing comparison of radar signatures among the different data sets.

Additionally, closely spaced higher resolution pseudo-3D grids (Figure 4.3) were acquired with 50 and 100 MHz antennas for detailed characterization of areas of specific interest. Grid locations were chosen to facilitate investigation of paleotopographic influence on depositional and post-depositional processes. Grid A, located on a paleotopographic high (western part of survey site) is 50 m by 70 m in size and has a line spacing of 5 m with 10 m spaced intersecting cross lines. Grid B, located on a paleotopographic low (eastern part of survey site) is 50 m by 50 m in size and has a line spacing of approximately 5 m with 5 m spaced cross lines. Optimal areas for 3D grids were determined by identifying locations in the 2D profiles that exhibited good data quality and were also located on relatively flat areas with minimal vegetation.

Profiles were collected in common-offset mode (transmitter-receiver separation remained fixed) as they were moved along the survey lines. Antennas were kept parallel to each other and were oriented perpendicular to the direction of movement along transects, with the transmitter located in the rear and the receiver in the front.

GPR transect locations were chosen to attain the straightest possible transects, while avoiding surface obstacles, such as thick vegetation, rocks, and patches of soil. Site preparation included removing loose rocks and stamping down large bushes along antenna paths, thus enhancing antenna coupling with the ground and reducing above ground airwave reflections. This preparation also allowed relatively consistent lateral antenna movement, ensuring even trace spacing. Antennas were positioned manually to record each trace as they were moved at regular increments along each survey line (Figure 4.4). A fixed separation between the antennas was maintained by attaching a rope to the antenna handles and also by carefully placing the antennas on marked survey lines. The digital data recorder allowed the traces to be viewed in the field as they were collected, ensuring the system was working properly.

Data acquisition parameters varied with each survey (Table 4.1). Trace spacing along profiles was determined by antenna frequency; 1 m, 0.5 m and 0.25 m trace spacings were used for the 25, 50, and 100 MHz antennas, respectively. Antenna separation was 4 m for the 25 MHz antennas, 2 m for the 50 MHz antennas, and 1 m for the 100 MHz antennas. Each trace was stacked 32 times and a sampling interval of 0.8 nanoseconds was used for all three frequencies. Vertical stacking increases signal-to-noise ratio of data, allowing faint and deeper reflections to be imaged (Annan, 2005). Record length varied between the different sets of antennas, but was generally between

1200 ns to 1400 ns for the 25 and 50 MHz antennas and 600 ns to 800 ns for the 100 MHz antennas.

To record the precise location of the profiles and account for surface topography, each transect was surveyed with a Trimble 5800 RTK differential global positioning system (DGPS) system. The position of each survey line was recorded every 0.5 m with the DGPS. Measurements have horizontal accuracy of 1 cm and vertical accuracy of 2 cm (Trimble Users Guide, 2010). Accurate spatial positioning of the GPR profiles obtained with the DGPS is crucial when multiple intersecting grid lines are acquired over rugged topography. Furthermore, precise coordinates of the profiles were essential in locating targets of interest along outcrops, allowing direct correlation of GPR data with specific stratal features.

Table 4.1. Summary of the survey parameters used for each of the three frequencies.

Frequency (MHz)	Trace Spacing (m)	Antenna Separation (m)	Sampling Interval (ns)	Record Length (ns)
25	1	4	0.8	1200-1400
50	0.5	2	0.8	1200-1400
100	0.25	1	0.8	600-800

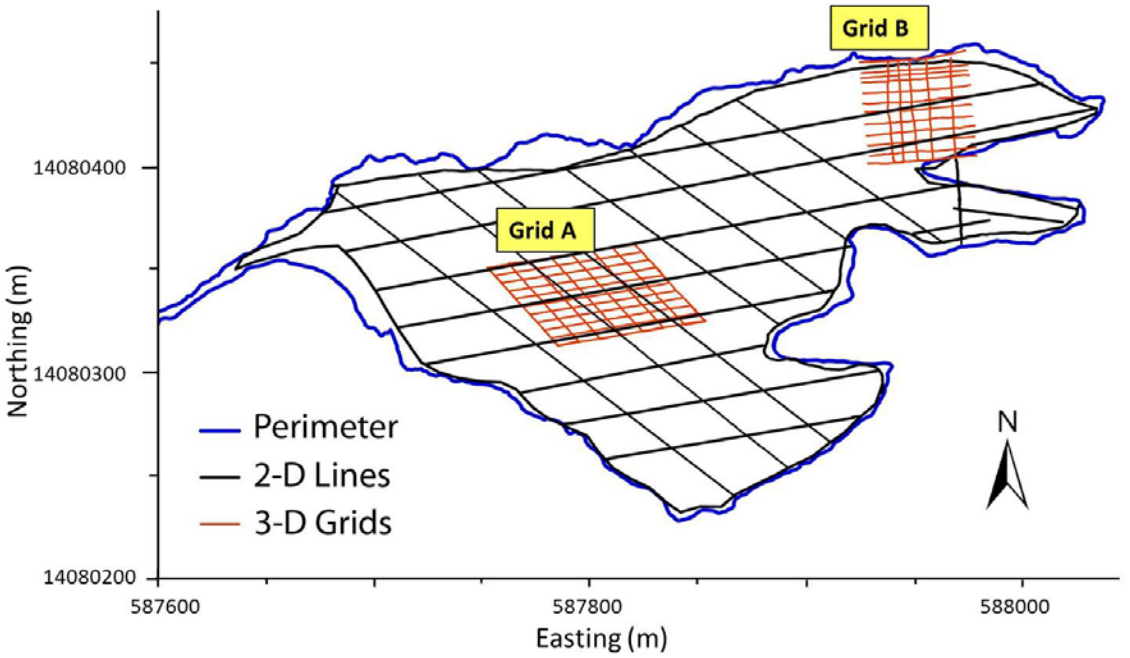

Figure 4.3. Map of study site showing location of GPR transects. 2D profiles (black lines) were collected with all three frequencies along the perimeter and along a grid covering the entire survey area with a line spacing of 20 m. Two pseudo-3D grids (Grids A and B, red lines) with 5 m by 5 m line spacing were collected in areas of different present-day and paleo-elevations to provide further detail of heterogeneity within the system and investigate paleotopographic influence on stratigraphic architecture. Grids A and B are approximately 50 m by 50 m in size.

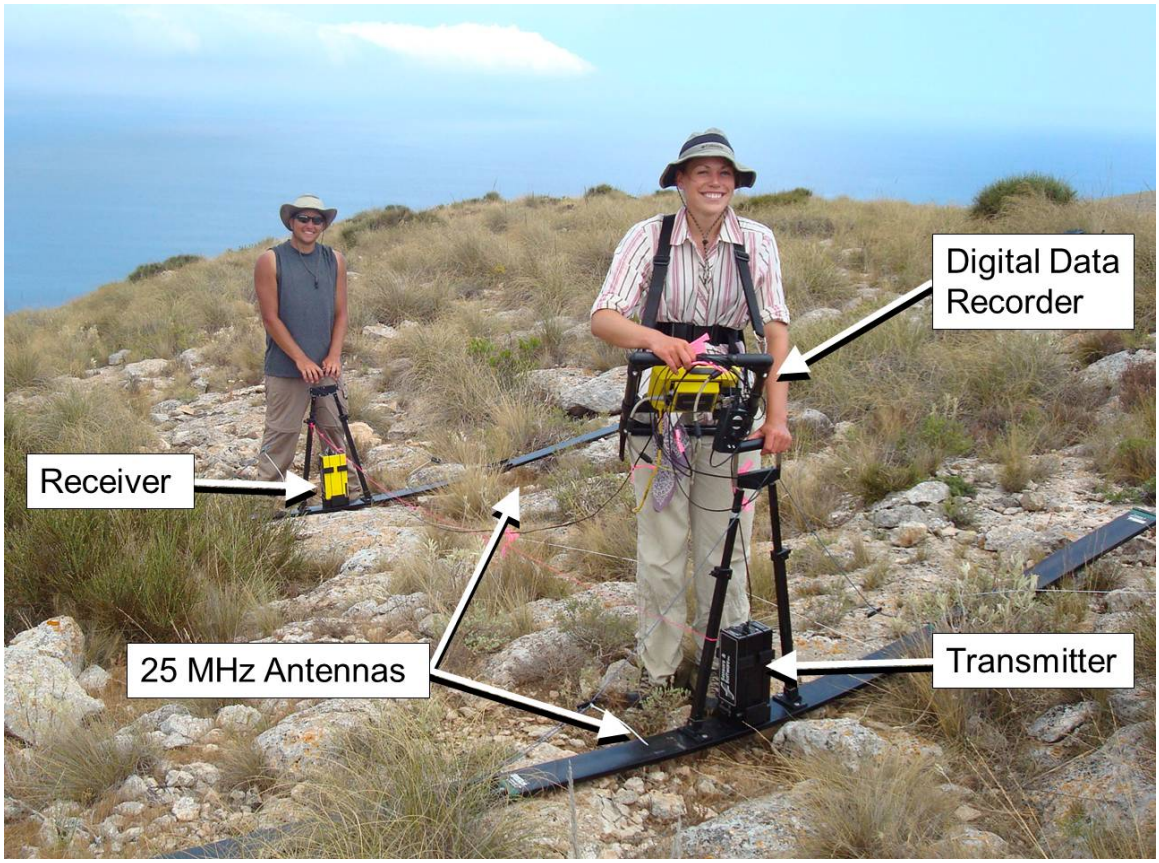

Figure 4.4. GPR system configuration and data collection, summer 2010. Antennas were manually positioned to record each trace as they were moved at regular increments along transects. Note the survey area includes loose rocks and vegetation that made antenna coupling with the ground challenging. Photo courtesy of George Tsoflias.

4.4: Data Processing

Following geophysical data acquisition, GPR data were processed in the lab (Table 4.2) using Sensors and Software's EKKOView Deluxe software. Experiments using a variety of processing methods and parameters provided insights on means to obtain the optimal data quality. Ultimately, several sets of data processed in different ways allowed retrieval of the most information from the profiles. Processing included both high and low-pass filtering, velocity analysis and migration, amplitude gain and topographic corrections.

The first step in data processing was application of a high-pass filter to remove low-frequency noise from the traces. GPR data commonly are affected by antenna bias, which is noise generated by DC offset; low-frequency noise is also induced between the transmitting and receiving antennas, due to their close proximity to each other (Annan, 2005). This noise, or low-frequency energy, is associated with electrostatic and inductive fields and decays rapidly with distance from the antennas. The noise commonly is referred to as 'WOW' and can be suppressed by applying a high-pass temporal filter. This step frequently is referred to as the 'DEWOW' process.

Following the removal of low-frequency noise, high-frequency noise was removed from the profiles using a low-pass frequency filter. The cutoff point varied depending upon the frequency of the data. The 25 and 50 MHz data were cut at 10% of the Nyquist frequency, which is half the sampling frequency of the signal and includes the highest frequency that the sampled signal can unambiguously represent (Yilmaz, 2001). This step resulted in preserving frequencies lower than 62.5 MHz in the 25 and 50

MHz data sets. The 100 MHz data were cut at 20% of the Nyquist frequency, which resulted in retaining frequencies lower than 125 MHz in the data set.

After the removal of high-frequency noise from the profiles, a spatial filter, commonly referred to as background removal, was applied to remove background noise (constant temporal noise). The background filter was computed using all traces in each profile. Background noise appears in GPR data as coherent noise that originates from ambient noise. Given the remoteness of the survey area, the majority of background noise was likely caused by the GPR system. Background noise typically shows up as horizontal banding or ringing in GPR data and can be readily identified because it appears at the same times across the profiles and has relatively consistent amplitude (Figure 4.5). This noise masked reflection data, especially in the lower parts of the profiles, where the signal-to-noise ratio was low. Although horizontal banding was present in the lower sections of all three frequencies, it was most prominent in the 25 MHz profiles (Figure 4.5A).

The background removal filter was most effective at enhancing the imaging quality of the 25 MHz data (Figure 4.5B), but it did not appear to have much of an effect on the higher frequency data sets. Analysis of the 25 MHz data before and after the background subtraction allowed more information to be retrieved from the lower portions of the profiles. Before background subtraction, a prominent horizon at approximately 12 m below the surface that was clearly evident in the 50 MHz data could not be easily differentiated from the background noise in the 25 MHz data. After background subtraction, the prominent horizon at 12 m was visible, although it was much fainter and difficult to trace in areas compared to the 50 MHz data. Background subtraction did,

however, facilitate recognition of faint reflections in the lower parts of the profiles. Therefore, examination of the 25 MHz profiles before and after this processing step was useful in interpretation of the data.

Following filtering, data were migrated using a constant velocity of 0.09 m/ns obtained by fitting diffraction hyperbolas in each of the data sets. This velocity was confirmed by measuring the time to a prominent reflection easily traceable on all profiles throughout the survey area that correlated to a stratigraphically significant horizon on the outcrop (discussed in detail later). Migration improved the imaging quality of the data significantly by collapsing diffraction hyperbolas and correcting the dip angles of steeply-dipping reflections and moving them to their true subsurface positions (Figure 4.6).

Next, the amplitude was adjusted using spherical and exponential compensation (SEC) gain, which corrected for spherical spreading losses and the exponential dissipation of energy. This gain is a composite of a linear time gain and an exponential time gain (Sensors and Software, 2006). The application of SEC gain enhances amplitudes by the same amount, and as such, information on relative amplitude differences between traces is maintained. This step is different from the commonly used Automatic Gain Control (AGC), which normalizes every trace and is not particularly useful for recognizing or preserving amplitude differences between traces (Figure 4.7).

Various amplitude gains were applied to improve imaging quality of reflections for interpretation. Weak reflections required application of stronger amplitude gains to enhance them, making geometries of these reflections more apparent, whereas stronger reflections required little to no amplitude gain to be most easily recognized.

The final step in the processing sequence was applying topographic corrections to each trace along profiles to correct for the variable topography of the survey area. Topography files were generated from the DGPS data and applied to the profiles using a velocity of 0.09 m/ns.

A non-traditional processing routine was applied to the data. The application of a DEWOW filter is usually the first step in data processing, but in one of the processing sequences, the DEWOW filter was applied to the data after migration. The resulting GPR images correlate more accurately to outcrop exposures than profiles in which the DEWOW filter was applied before migration, suggesting that the low frequency "WOW" signal contains useful subsurface imaging information.

The profiles in which the DEWOW filter was applied following migration contain amplitudes in some areas closest to the surface that appear to have been dampened to the degree that they have amplitudes of zero (Figure 4.8). Upon closer examination, these areas of apparent zero amplitude are actually areas that had very strong amplitudes that had been clipped, making them appear as areas with no amplitudes.

These areas of apparent zero amplitude correlate well with geologic features, namely the thrombolite bodies that have very low porosity (discussed in detail below). Although the contribution of the low frequency "WOW" signal to the zero amplitude reflections is not fully understood, the data suggest that there is some geologic control on the radar data. This processing may prove to be a new method of detecting certain geologic or petrophysical features, at least in this data set. This step needs to be investigated further to determine what actually happened to the data through the application of the DEWOW filter after the migration step.

Following processing, GPR profiles were converted to SEG-Y format and imported into a seismic interpretation software package (Seismic Micro-Technology's Kingdom Suite). Standard seismic interpretation methods were used to correlate reflections between profiles, allowing 3D interpretation of the entire survey area.

Table 4.2. Processing sequence for the GPR data. Note that some of the parameters vary depending on the frequency of the data.

Process	**Purpose**	**Parameters**
Stack	Enhance signal-to-noise ratio	Each trace stacked 32 times
DEWOW filter	Remove low-frequency noise induced by antennas	Manufacturer-optimized high-pass filter applied
Background noise removal	Remove horizontal 'banding' or constant temporal noise	Averaged noise from entire profiles. Only applied to 25 MHz data
Low-pass filtering	Remove high-frequency noise	100 MHz data cut at 125 MHz. 50 and 25 MHz data cut at 62.5 MHz.
Migration	Collapse diffraction hyperbolas and move steeply dipping reflectors to correct subsurface locations	Velocity of 0.9 m/ns determined by fitting diffraction hyperbolas
Amplitude gain	Correct for GPR signal attenuation with time, maintain relative changes in amplitude throughout each profile	Spreading and Exponential Compensation (SEC) gain
Topography correction	Account for highly variable topography	DGPS elevation measured every 0.5 m along transects

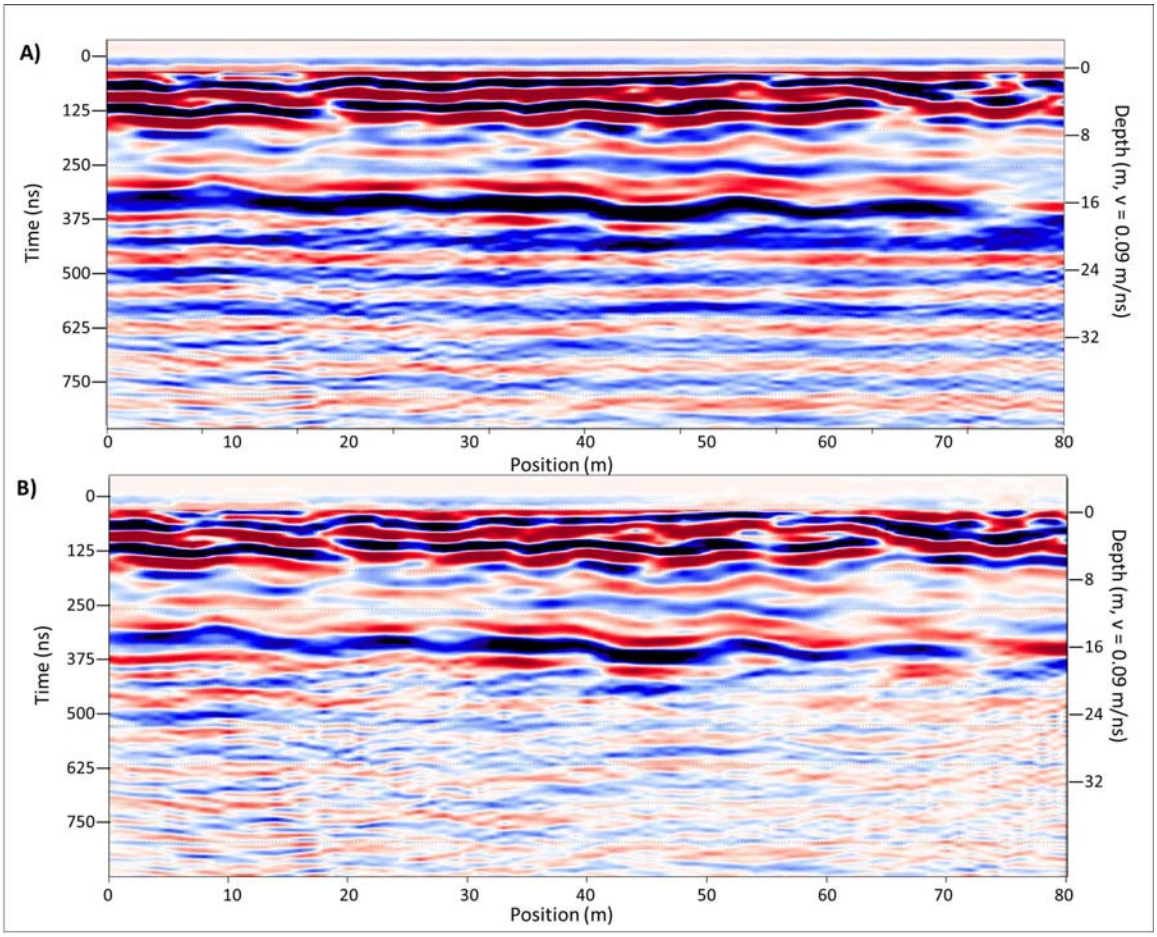

Figure 4.5. Character of GPR data before and after removal of background noise. A.) 25 MHz profile before background subtraction. Note prominent horizontal banding (constant temporal noise) is most prominent in the lower portion of the profile. B.) After application of a background removal filter, background noise was markedly decreased, allowing faint reflections in the lower parts of the profile to be more easily recognized.

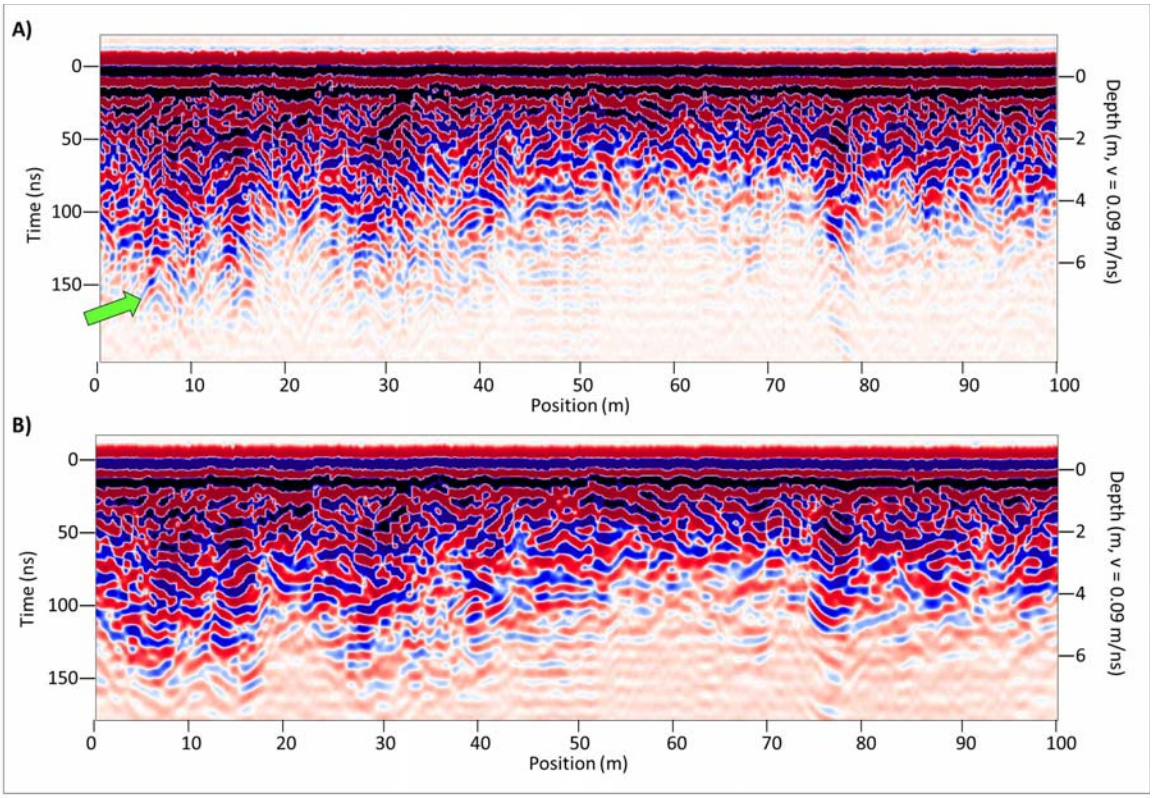

Figure 4.6. Effect of migration on GPR data on a representative 100 MHz profile. A.) Unmigrated profile; green arrow points to a diffraction hyperbola. B.) Migrated profile using a migration velocity of 0.09 m/ns. Note diffraction hyperbolas have been collapsed and steeply dipping reflections have been adjusted to their true subsurface locations. The migration step greatly improved the quality of the data by allowing imaging of complex subsurface geometries.

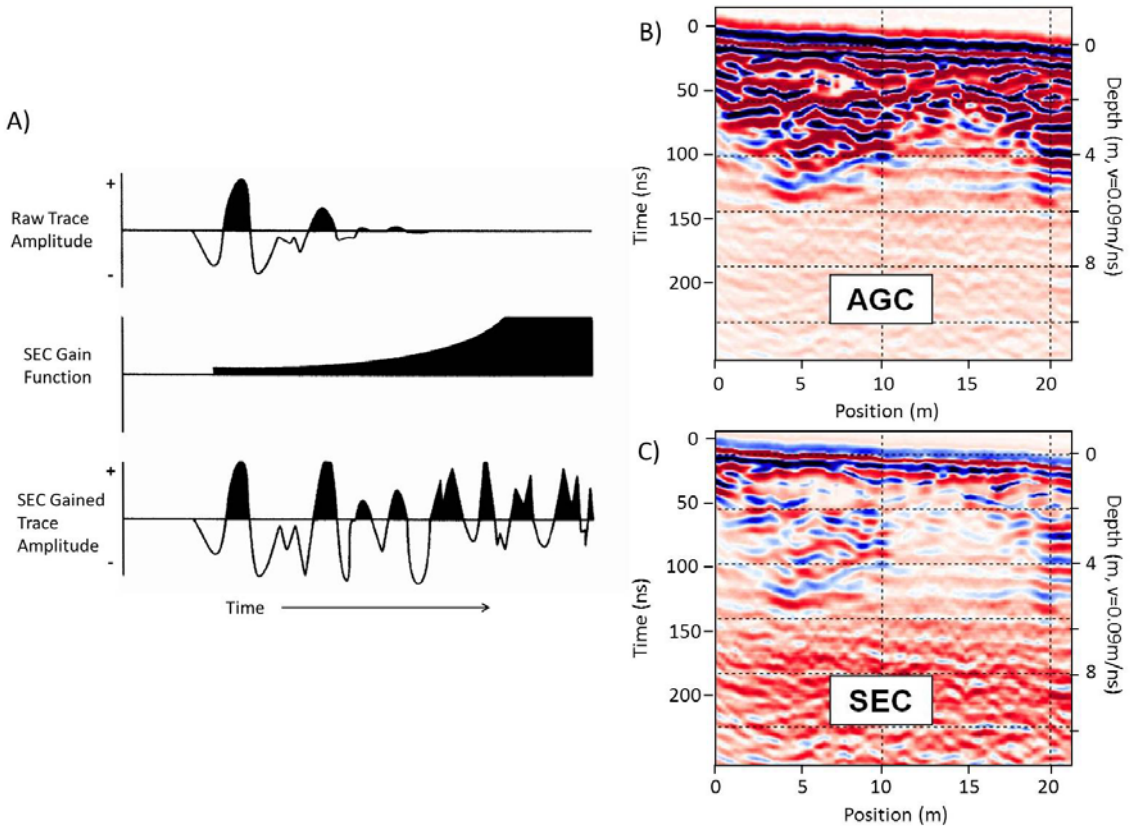

Figure 4.7. A.) The SEC gaining process scales each point in an ungained trace (top) by corresponding points in the SEC gain function (middle), resulting in a trace with more consistent amplitudes with time (bottom). (Modified from Sensors and Software, 2006). B.) 100 MHz profile after AGC has been applied. C.) Same 100 MHz profile after SEC gain applied. The application of an SEC gain enhances the amplitudes of weaker reflections from greater times (greater depths), emphasizing reflections and enhancing their interpretability. Note that the SEC gain is an exponential function and that the same gain function is applied to each trace throughout the profiles, maintaining relative signal strengths.

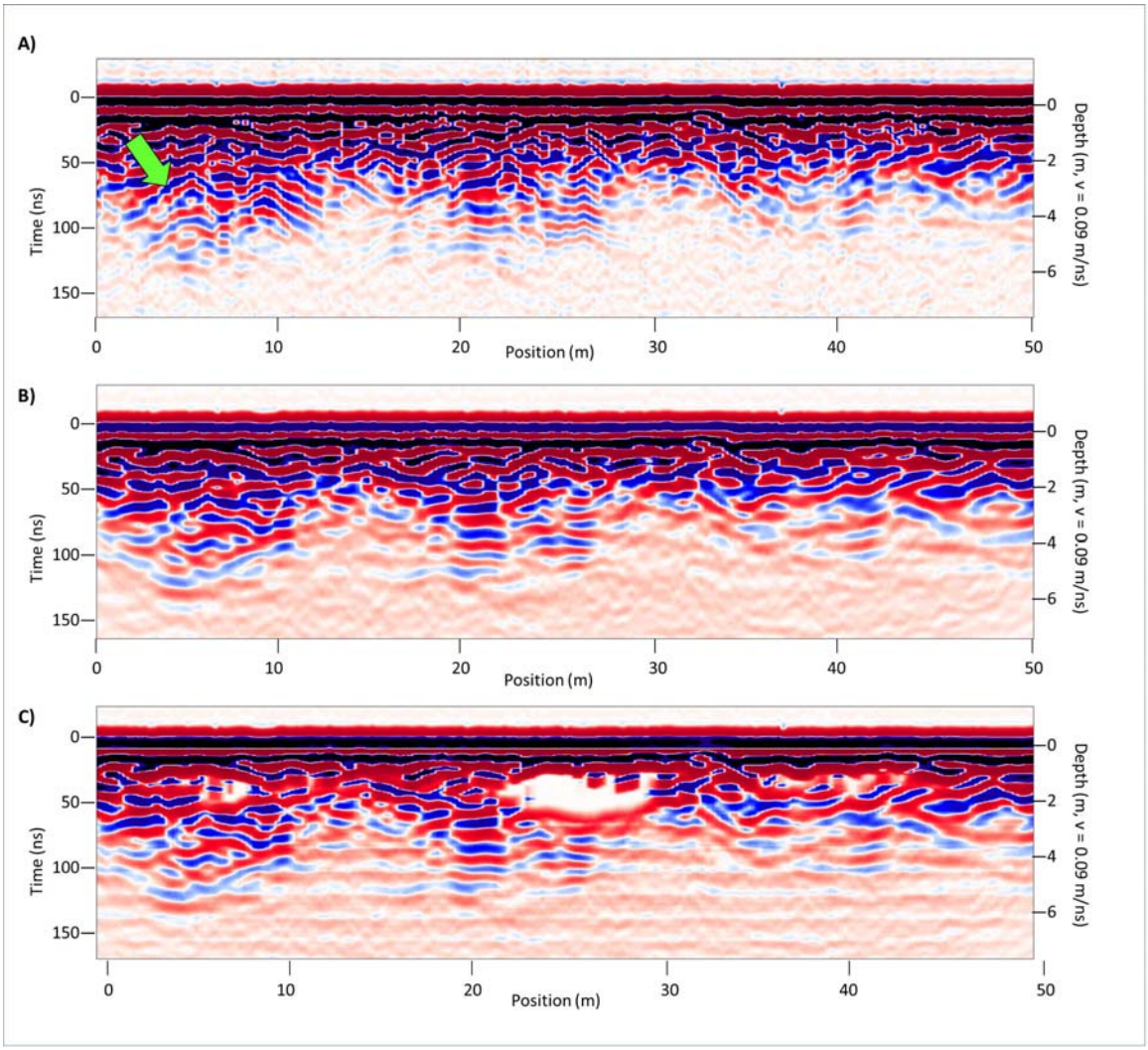

Figure 4.8. Effect of application of DEWOW before and after migration. A.) Unmigrated profile (100 MHz), note diffraction hyperbolas (green arrow) and steeply dipping reflections. B.) Migrated profile with DEWOW applied *before* migration. C.) Migrated profile with DEWOW applied *after* migration. Note the bright white area in the center of the profile appears to be completely devoid of reflections.

4.5: Resolution Identification

After completing data processing, the resolution of each of the three frequencies was determined, as knowledge of the size of features that can be resolved with each data set is essential for accurate interpretation of the data. Resolution is the ability of the data to differentiate two reflections that are close to each other in time and defines the maximum size of feature that can be unambiguously imaged (Davis and Annan, 1989). It is dependent on wavelength, which is a function of frequency and velocity. The equation for resolution is $\lambda = v/f$, where λ = wavelength, v = velocity, and f = frequency. Resolution of GPR data is typically considered to be approximately one-quarter of a wavelength (Davis and Annan, 1989; Neal, 2004; Annan, 2005). Therefore, the theoretical resolution of the three different frequencies (25, 50 and 100 MHz) using a velocity of 0.09 m/ns is approximately 0.9 m, 0.45 m and 0.225 m, respectively. Because resolution is not determined solely by frequency, actual resolution may vary depending on changes in velocity, with lower velocity media having shorter wavelengths (greater resolution) than higher velocity media (Davis and Annan, 1989; Lines and Newrick, 2004; Bristow, 2009). Furthermore, theoretical resolutions are rarely obtained because the dominant frequency recorded by the receiving antenna is typically lower than the transmitted frequency because of signal attenuation. Actual resolution values were obtained by determining the dominant frequency of each data set through examination of average amplitude spectra (Figure 4.9).

The actual resolutions (one-quarter wavelength of the peak frequencies) were found to be between 70 and 80% of the theoretical values. This degradation is likely due to energy losses associated with imperfect coupling with the ground and signal

attenuation in the subsurface. As a result, the estimated resolution of the 25, 50, and 100 MHz antennas is approximately 1.12 m, 0.59 m and 0.31 m, respectively (Table 4.3). These values represent the minimum thickness of a layer or size of geometric feature that can be resolved at each frequency.

Table 4.3. Resolution of the three different frequencies determined from dominant frequencies of data sets.

Transmitted Frequency (MHz)	**Dominant Frequency Recorded (MHz)**	**Wavelength (m)**	**Resolution (m)**
25	20	4.50	1.12
50	38	2.37	0.59
100	72	1.25	0.31

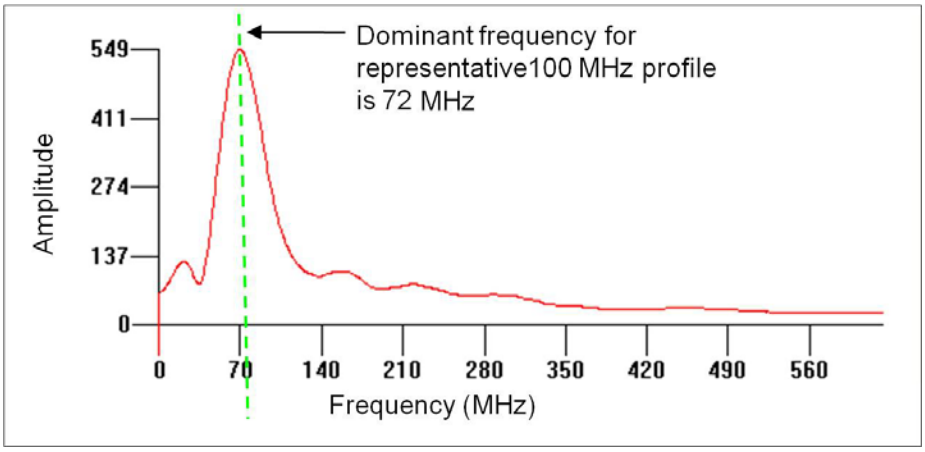

Figure 4.9. Average amplitude spectrum of a representative 100 MHz profile. Note that the dominant frequency, denoted with green dashed line, is approximately 72 MHz, less than the 100 MHz input signal.

4.6: Outcrop Description and Sampling

Identification of specific events and radar signatures was aided by basic processing of GPR data carried out during data collection. *In situ* groundtruth of the radar data was provided by comparing outcrops in the field to GPR signatures along the perimeter of the survey area. Correlation of radar reflections to the facies and textural characteristics of the adjacent outcrop was the most critical step in the interpretation of the data, as correlations from the profiles nearest the perimeter provided calibrations for interpretation of profiles from the interior of the survey area, away from outcrops.

The numerous lithofacies in the survey area have been characterized by Lipinski (2009). This study utilizes this framework, and evaluates the four primary carbonate lithofacies (ooid grainstone, dense thrombolite boundstone, vuggy thrombolite boundstone, and stromatolite) for comparison to GPR data (Table 4.4; Figure 4.10). Additionally, at the top of each sequence, some ooid grainstone units contain volcaniclastic grains which influence the GPR signature. This thickness of the volcaniclastic-rich ooid grainstone capping Sequence 3 ranges in thickness from 15 cm to 40 cm, with an average thickness of approximately 30 cm, which is nearly twice the thickness of the volcaniclastic-rich ooid grainstone capping Sequence 4.

One depositional facies, ooid grainstone, most commonly is trough cross-bedded and grades upward to planar-bedded volcaniclastic-rich ooid grainstone that is capped by fenestral ooid grainstone (Figure 4.10A, B). Ooid grainstone deposits range in thickness from 0.5 m to more than 12 m and may be laterally extensive for 10s of meters, although in some instances deposits are less than 1 m across, filling between thrombolite bodies.

Another depositional facies, thrombolite boundstone, typically displays a dark gray to brown, clotted, micritic texture (Figure 4.10A, C). Deposits commonly include ooids and peloids as well as skeletal fragments including gastropods, bivalves, calcareous red algae, benthic foraminifera and serpulid worms. Thrombolite units range in thickness from 0.3 m to 4 m and may be 0.5 m to 10s of meters wide. The geometries of these bodies may be mound-like to loaf-shaped and even columnar in form. The boundaries between thrombolite units and adjacent ooid grainstone units may be sharp or gradational; many of the thrombolite units include ooid grainstone interbeds.

Still another depositional facies, stromatolite, is finely laminated, have alternating coarse-fine laminae and may be planar, undulating or wavy in form (Figure 4.10D). Rarely, they exhibit domal or digitate morphologies. Stromatolite units range in thickness from 0.05 m to 0.7 m, with an average thickness of 0.2 m to 0.3 m.

In addition to detailed description of outcrops, 62 rock samples representing a range of variability in lithofacies and porosity were collected for thin section analysis. These samples were collected systematically from the perimeter of the survey area to include varying GPR signatures. A DGPS was used to record the location of each sample and also the position of sequence boundaries, providing accurate measurements to which the GPR data could be correlated. Rock samples from areas of GPR transects were within 1 to 2 m of the GPR data. Samples were collected from all portions of the survey area, although some areas were more densely sampled than others (see Figure 5.9) to tightly constrain GPR data to depositional facies. Once a field relationship was established between hand samples and GPR data, it was used to relate GPR facies to lithology throughout the study site. Hand specimens include a wide range of rock textures ranging

from coarse-grained oolitic grainstone with interparticle to oomoldic porosity to thrombolites with varying amounts of porosity. Of the hand samples collected for this study, 27 are thrombolite, 24 are ooid grainstone and 11 are stromatolite.

Table 4.4. Lithofacies of Lipinski (2009) compared to lithofacies utilized in this study, and their sedimentologic characteristics. Note lithofacies of this study consider many of the previously defined lithofacies as a single type for comparison to GPR data.

Lithofacies defined by Lipinski (2009)	**Lithofacies utilized in this study**	**Characteristics**
Massive ooid grainstone	Ooid grainstone	Trough cross-bedding dominates much of the ooid grainstone; may be interbedded with thrombolite and include skeletal fragments (gastropods, bivalves, serpulid worms) and peloids. Planar cross-bedding and volcanic rock fragments are more common in the uppermost portions of sequences and commonly display evidence of subaerial exposure (fenestrae, meniscus cements and rhizoliths).
Trough cross-bedded ooid grainstone		
Cross-bedded oolitic gastropod grainstone		
Volcaniclastic-rich planar-bedded ooid grainstone		
Fenestral ooid grainstone		
Dense thrombolite boundstone	Dense thrombolite boundstone	Clotted, micritic texture; may include ooids and skeletal fragments. Low porosity.
Vuggy thrombolite boundstone	Vuggy thrombolite boundstone	Clotted, micritic texture; may include ooids and skeletal fragments. Common vuggy porosity.
Stromatolite	Stromatolite	Fine, planar to wavy laminae, digitate in some areas.

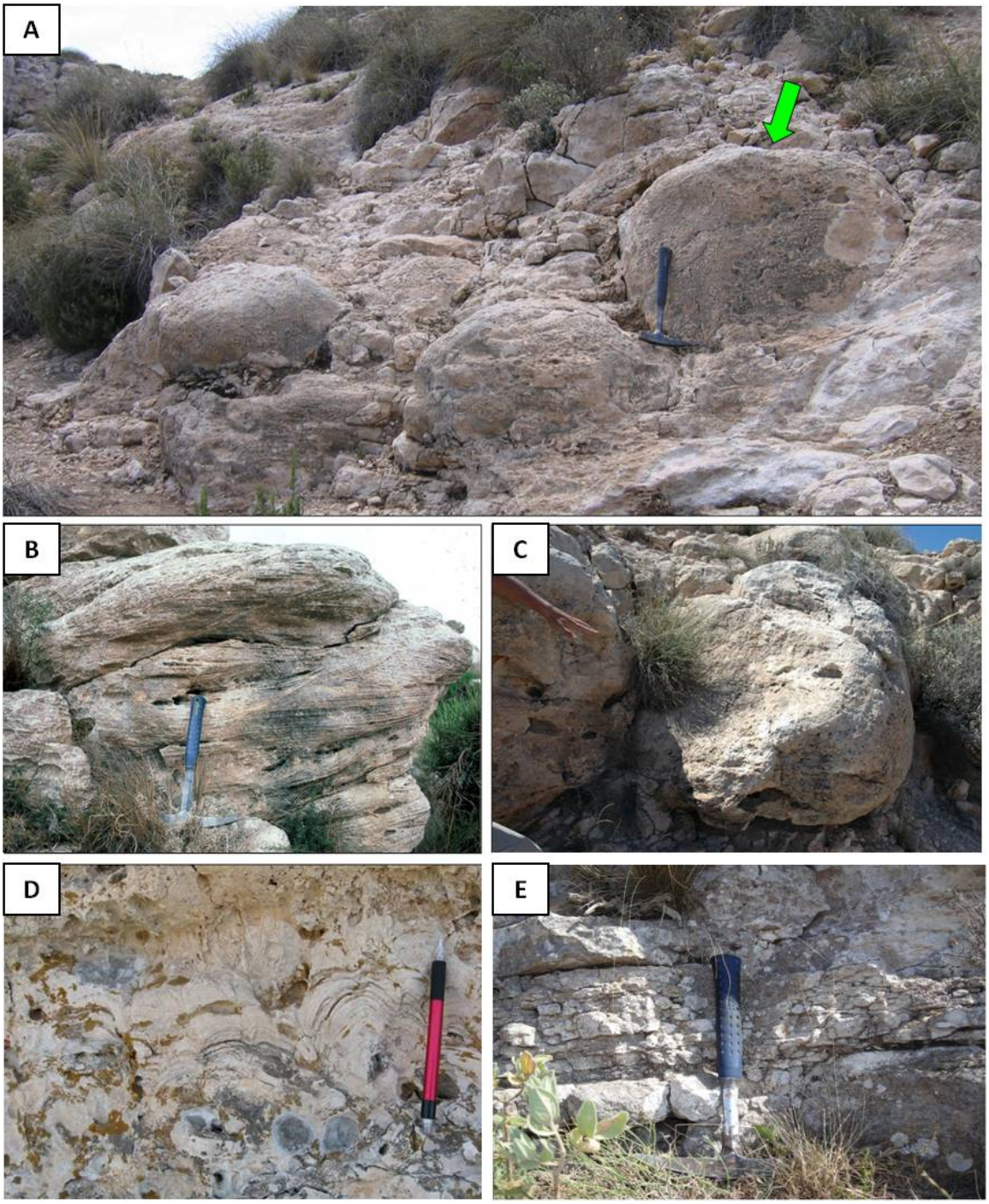

Figure 4.10. Representative outcrop photos of key lithologies. A) Detail of outcrop showing the various lithofacies found in the TCC. Green arrow points to one of the three rounded thrombolite units in the foreground; ooid grainstone is surrounding the thrombolites. B) Trough cross-bedded ooid grainstone. Note complex cross bed sets and truncations, and the differential weathering that reflects different degrees of cementation. C.) Thrombolite boundstone. Note the bulbous morphology emphasized by weathering on the outcrop; hand for scale. In the outcrop, depositional fabric is a cryptic, clotted, micritic texture. D) Stromatolite with undulating to wavy laminations; note pencil for scale. E.) Volcaniclastic-rich ooid grainstone; this friable unit commonly weathers to gentle slopes on outcrops.

4.7: Petrographic Analysis of Rock Fabrics

A total of 62 thin sections were prepared and examined to provide detailed information on rock fabrics. Petrographic analysis included description of depositional aspects including texture, grain type, size and sorting. Additionally, rock fabric features such as pore type (moldic, interparticle and vuggy), pore size, cementation and mineralogy were explored. Thin sections were prepared using standard techniques. Samples were impregnated with blue epoxy and analyzed with JMicroVision ™ image analysis software to quantify porosity (Figure 4.11). The image processing technique of thresholding was used to evaluate porosity; blue colored, epoxy-filled portions of samples were taken to be porosity. A total of 12 photomicrographs from each sample provide fundamental petrographic data for porosity analysis. The average porosity from each of the 12 photomicrographs was used to determine average porosity of each sample. Thin section data as they correlate to radar reflections, specifically variations in porosity, are important to understanding GPR signatures (discussed in detail in Chapter 6.1).

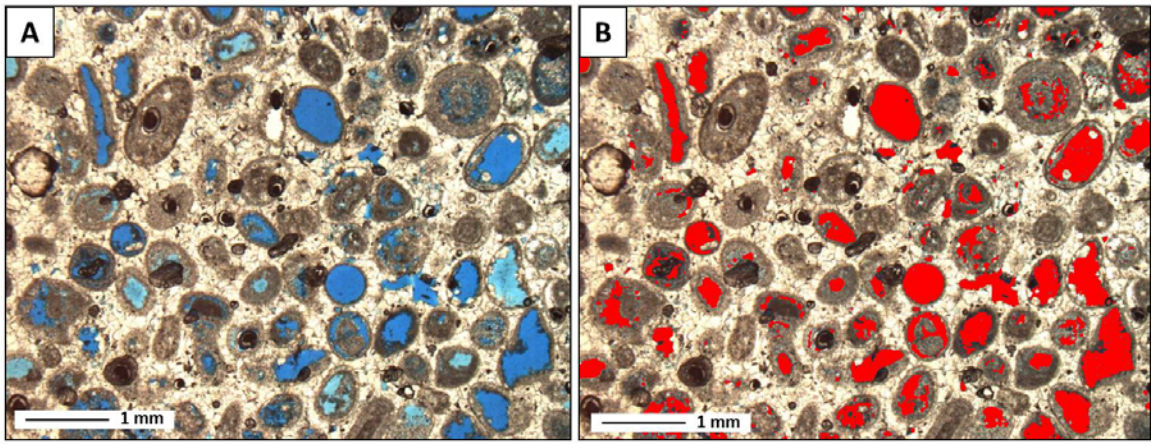

Figure 4.11. Appearance of porosity in thin section before and after using image analysis software. A.) Ooid grainstone impregnated with blue epoxy. B.) Same ooid grainstone sample with pores highlighted in red. Image analysis software allowed easier visualization of pore size, shape and distribution, and quantification of porosity. This sample has 23.1% porosity.

CHAPTER 5: RESULTS

5.1: Rock Fabrics

Stratigraphy and depositional facies are first-order influences on rock fabric, but in this succession, the strata have been impacted by various processes of diagenesis as well. The combination of depositional and diagenetic processes creates highly variable rock fabrics among and within depositional facies across the study area. The purpose of this section is to provide qualitative and quantitative data on the variability of rock fabrics present in each of the three dominant lithofacies that make up the succession (ooid grainstone, thrombolite boundstone, and stromatolite); a later section (Section 5.3) will discuss how these relate to GPR data. Although diagenesis has impacted the survey area, the focus of this study is to describe the present-day rock fabrics and relations to GPR, not to elucidate the complex diagenetic processes and history. Likewise, the complex diagenetic history of the study area is currently the focus of on-going dissertation research by Zhaoqi Li.

Ooid Grainstone

Ooid grainstone displays a wide range of variability both in depositional and diagenetic textures (Figure 5.1A-C). Ooids range in diameter from 0.1 mm to 0.5 mm; the majority are approximately 0.3 mm in size. Ooid grainstones range from well- to poorly sorted and contain variable amounts of skeletal fragments. Ooid grainstones have been impacted by diagenesis; many have been completely recrystallized and porosity has been enhanced in some grainstone and reduced markedly in others. Porosity of ooid grainstone samples ranges from 9.4 to 46.6%, with an average porosity of 17.7 (n = 24). Pore types in ooid grainstone include moldic, intergranular and vuggy; the dominant pore type in

most samples is moldic, from the dissolution of ooids and skeletal grains. Variation is at the scale of the entire survey area, sequences, individual trough cross-bed sets, beds, laminae, and even single thin sections (Figure 5.2).

Most ooid grainstones consist of calcite and dolomite with little mineralogic variability. The exceptions are volcaniclastic-rich ooid grainstone units found at the top of sequences. These units appear to impact radar signals, as illustrated below.

Dense and Vuggy Thrombolite Boundstone

Thrombolite boundstones are recognized by clotted, micritic textures (Kennard and James, 1986; Planavsky and Ginsburg, 2009). In the study area, thrombolites display micritic textures that are commonly heavily recrystallized (Figure 5.1D, E). Although dense thrombolite boundstone units have low porosity, the vuggy thrombolite boundstone units include solution-enlarged vugs. Diameter of vugs ranges up to 10 mm in size, although most appear to be in the range of 0.2 to 0.5 mm. Similar to ooid grainstones, there is a large range of variability in porosity within and among thrombolite bodies. Porosity of thrombolite units ranges from 3.9 to 29.9%, with an average porosity of 13.0% (n = 27).

Stromatolite

Stromatolites are also heterogeneous and have a wide range of textures and porosity. Stromatolitic laminations are typically about 0.1 mm thick and may be laminar, wavy, or crinkly. Some stromatolites are digitate, with small branches protruding from the surface. Nonetheless, many have been recrystallized to the point that individual laminations are indistinguishable, and are recognized only by undulating form in outcrop.

Average porosity of stromatolite samples is 12.6% although it ranges from 3.5 to 24.5% (n = 11). Porosity is moldic and vuggy, and pores are typically less than 0.1 mm in diameter. Dissolution commonly enhances or creates porosity along laminations (Figure 5.1F).

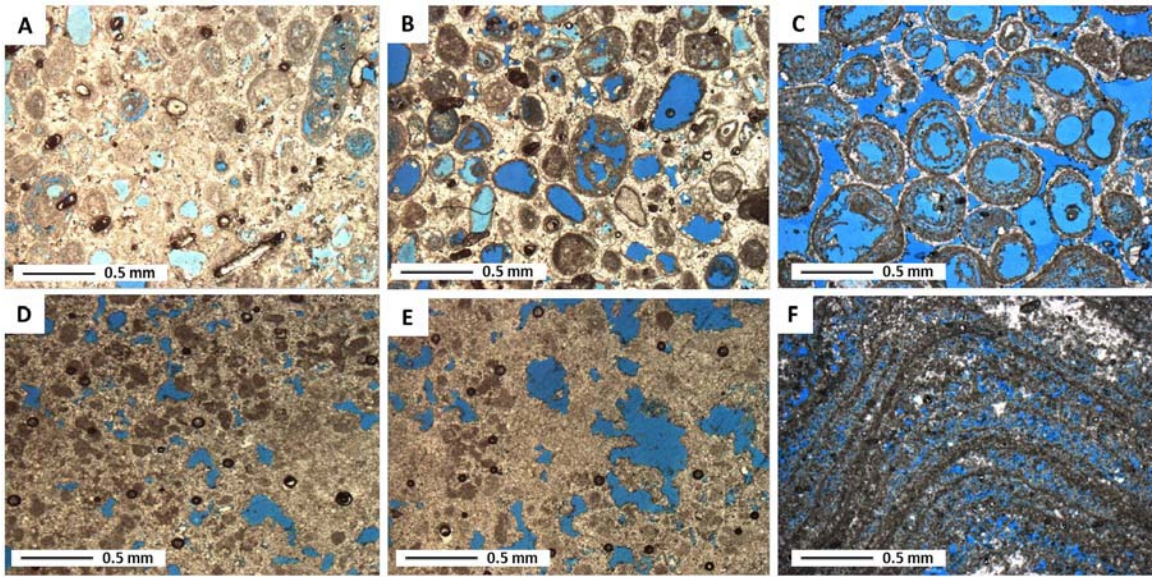

Figure 5.1. Representative photomicrographs the three major facies illustrating the variability in rock fabrics. In each, the blue color represents open porosity. A) Well cemented, recrystallized ooid grainstone with low porosity (8.8%). B) Ooid grainstone with intermediate porosity (15.5%), C) Ooid grainstone with high porosity (43%). D) Moderately recrystallized thrombolite with low porosity (dense thrombolite boundstone) (7.1%). E) Thrombolite with intermediate porosity (vuggy thrombolite boundstone) (17.1%). F) Stromatolite with intermediate porosity (18.2%). Note the great range of porosity, both within and among different lithofacies. Qualitatively, these photomicrographs illustrate that diagenesis is the dominant control on porosity in this succession, not primary depositional texture.

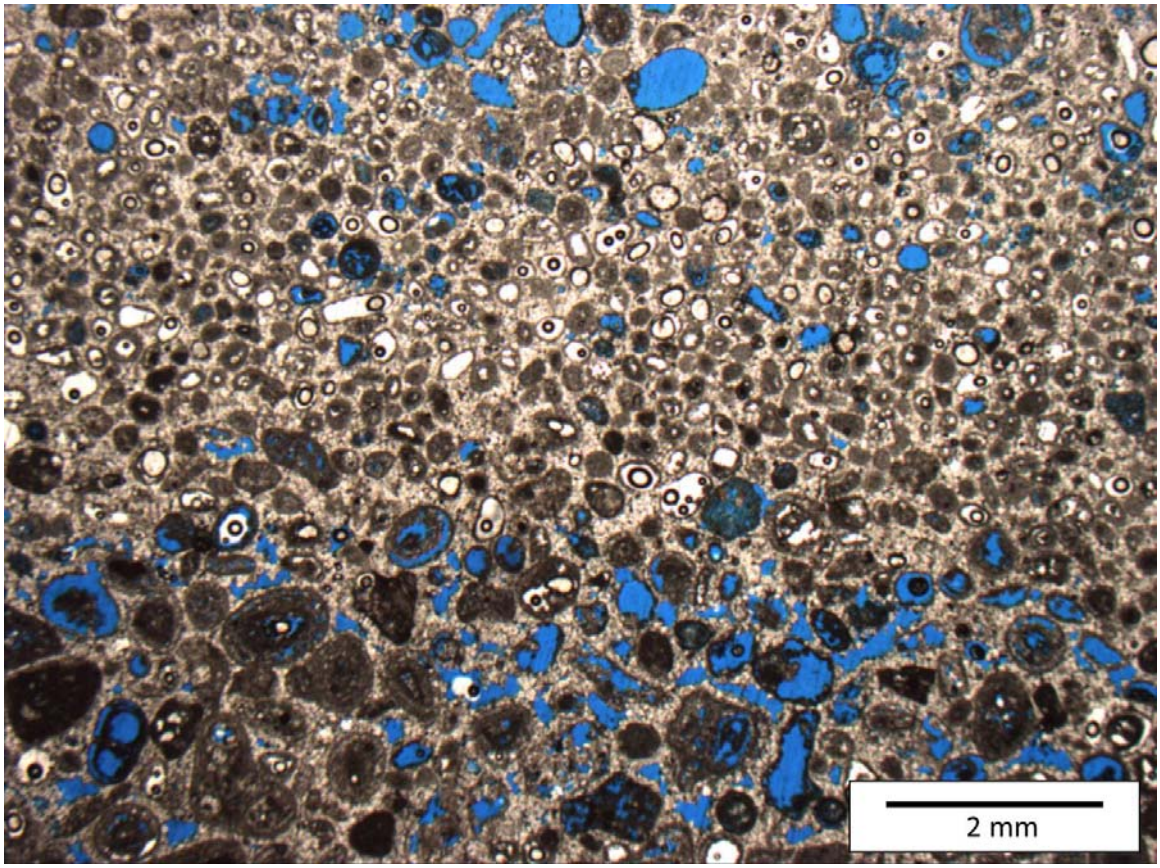

Figure 5.2. Thin section photomicrograph of ooid grainstone displaying abrupt variation in grain size, shape, sorting, and sharp changes in preserved (open) porosity. (Blue color is epoxy filling pore space.) This variation is present from the thin section scale, to between individual beds and bed sets of this depositional facies.

5.2: Character of GPR Signatures

The 25 and 50 MHz antennas penetrated to a depth of approximately 12 m and provide a vertical resolution of 1.12 m and 0.59 m, respectively. The 100 MHz antennas penetrated the subsurface to approximately 6 to 8 m and had a vertical resolution of 0.31 m. Despite different resolutions, characteristics of radar data are similar among the three frequencies, as discussed in detail below.

Although all three frequencies included similar signatures in the same locations along profiles, the character of the reflections varies markedly both laterally and vertically. In some areas, reflections were very strong, and in others, reflections were much weaker or appeared absent; in some cases, these were accompanied by changes in continuity and geometry. Four GPR facies, recognized on the basis of reflection signatures (strong, weak, or no internal reflections) are evident in data and define geometric bodies (Figure 5.4).

GPR Facies A is recognized by the absence of internal reflections. These areas are evident on the profiles as mostly discontinuous, patchy white bodies (Figure 5.4A). GPR Facies A can cover a lateral extent of between 2 m to more than 30 m and range in thickness from 0.5 m to 4 m. This facies is more common in downdip areas of the survey area.

GPR Facies B is characterized by weak internal reflections (Figure 5.4B). These reflections are discontinuous and are undulating to wavy. GPR Facies B is ubiquitous in all survey lines in the updip parts of the survey area, where it is continuous across tens of meters and may reach up to 11 m in thickness. Downdip, this facies is discontinuous and

patchy, extending across widths of approximately 20 m, and rarely exceeding a thickness of 8 m.

GPR Facies C exhibits strong internal reflections, most of which are wavy and discontinuous (Figure 5.4C). This facies is most common in the downdip parts of the survey area. The lateral extent of GPR Facies C seldom is greater than 40 m and typically has a thickness of 6 m to 10 m, but reaches a maximum thickness of 12 m.

GPR Facies D is represented by one stratigraphically important and widespread feature observed in in the 25 MHz and 50 MHz data at a depth of approximately 12 m is a strong, continuous reflection evident throughout the survey area (Figure 5.4D). This prominent event is the only reflection that can be traced continuously throughout the survey area. The 100 MHz data did not image strata at this depth, so do not include this GPR signature.

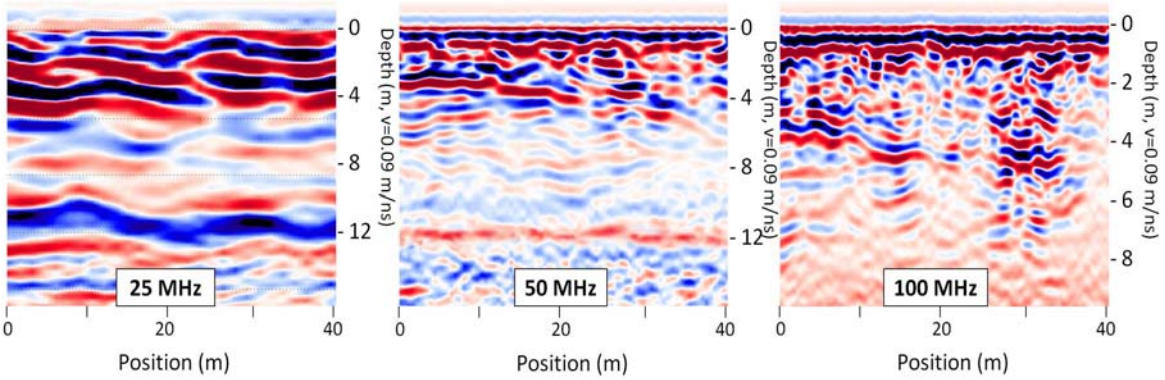

Figure 5.3. Representative profiles from each of the three frequencies used in this study showing the varying depths of penetration. Note that the 25 and 50 MHz data both penetrated to a depth of approximately 12 m, whereas the 100 MHz imaged to a depth of approximately 6 to 8 m (Note depth scale is different for 100 MHz data).

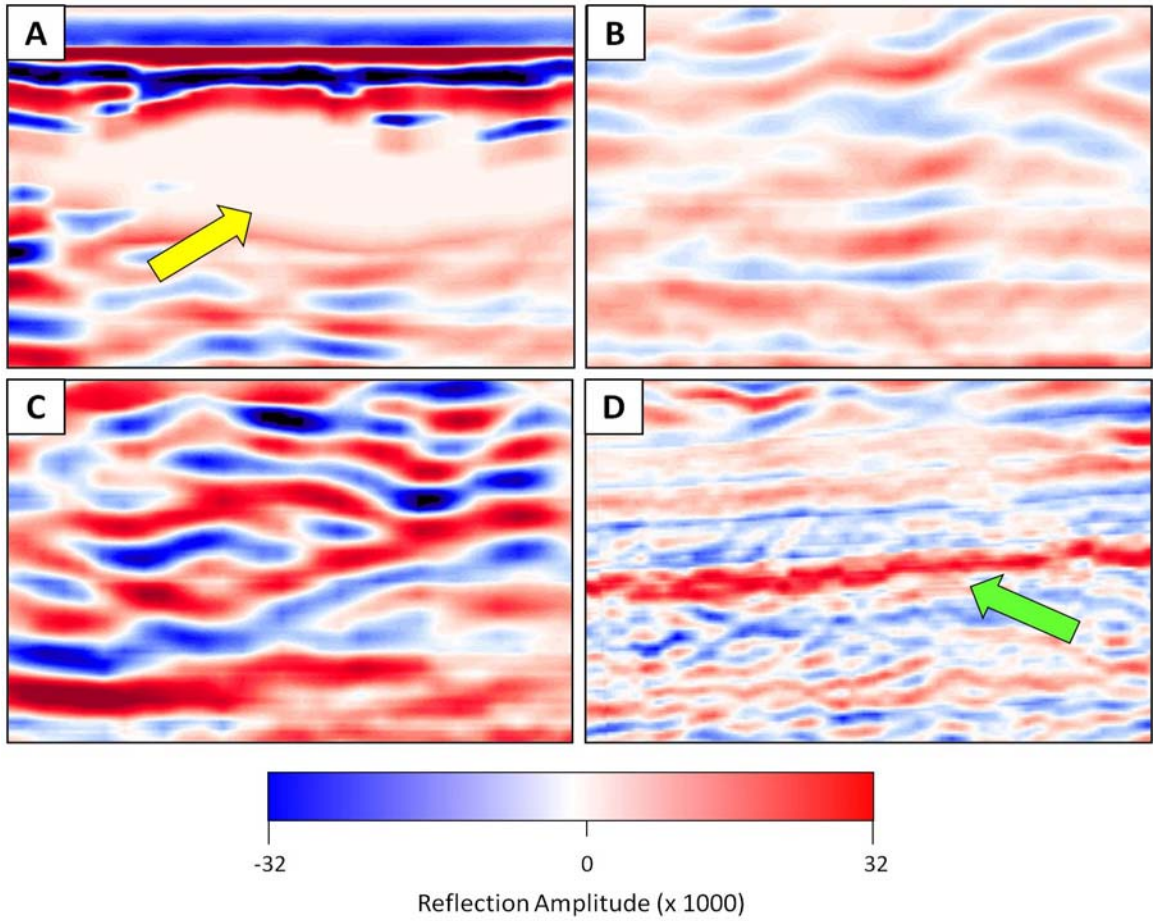

Figure 5.4. Representative lines illustrating different GPR facies (GPR Facies A-C). The first three GPR facies are defined by the character of reflections in all frequencies (50 MHz data shown). A) Zones exhibiting no internal reflections (yellow arrow), B) Zones exhibiting weak internal reflections, C) Zones exhibiting strong internal reflections, D) Another GPR facies (D), is characterized by the strong, continuous reflection (green arrow), evident only in the 25 and 50 MHz data. This reflector is present across the study area and forms the base of the study interval.

5.3: Calibration of GPR Facies to Depositional and Diagenetic Attributes

Well-exposed, near-vertical cliffs surrounding the survey area provide the opportunity to calibrate radar data with geologic features (Figure 5.5). Correlation of radar signatures with variation along the outcrop face revealed that GPR facies correlate with depositional facies in some instances at several scales and frequencies (Figures 5.6, 5.7).

The closest association between radar character and depositional features occurs with the strong, continuous reflector described above (GPR Facies D; Figure 5.4D). This reflection represents a prominent event in the GPR data at a depth of approximately 12 m that correlates with a layer of volcaniclastic-rich ooid grainstone that directly underlies Sequence Boundary 3. This unit is continuous along the outcrop and ranges in thickness from 20 cm to 60 cm, with an average thickness of approximately 30 cm. On the outcrop, the volcaniclastic-rich grainstone unit is nonresistant and very friable, with volcanic rock fragments in some areas altered to clay minerals. Signal attenuation across this interface is so great that it inhibited imaging of stratigraphy below this horizon in both the 25 and 50 MHz data (see Figures 5.6, 5.7). This prominent reflection forms the base of the study interval.

Although there is a close correspondence between stratigraphy and this strong, continuous reflection, the GPR facies above it (GPR Facies A-C), in sequences 3 and 4, do not show the same association with distinct depositional facies. Instead, they are influenced additionally by rock textures related to diagenetic overprinting (cementation or dissolution). Analysis of outcrop, slab and thin section samples reveals the following qualitative relationships:

- *GPR Facies A*, zones exhibiting no internal reflections, correlate to thrombolite bodies that typically have very low porosity.
- *GPR Facies B*, characterized by weak internal reflections, correlates to units with moderate porosity, independent of depositional facies. Facies B can be made up of oolite, thrombolite or stromatolite units.
- *GPR Facies C*, recognized by strong internal reflections, generally correlates with high, but variable, porosity units. The most common lithology correlating to GPR Facies C is ooid grainstone, although thrombolite and stromatolite units are found in association with this facies locally.

These relations between geologic features and radar facies are qualitatively evident at several scales throughout the study site. These associations can be refined and quantitatively explored, as well. To do so, petrographic analysis provides quantitative data on types and amounts of porosity of samples systematically collected to evaluate the range of variability in GPR signature.

A plot of porosity for each radar facies reveals that porosity is qualitatively distinct among the GPR facies (Figure 5.8). For example, the mean porosity values for rocks corresponding to the occurrence of GPR Facies A, B and C are 7.9%, 15.0% and 22.5%, respectively (Table 5.1.)

The differences can be quantified by nonparametric statistical analysis (Mann-Whitney U). This technique is useful for testing whether group means are the same across a number of groups with non-normal distributions. Tests of these data reveal that porosity

for each GPR facies are statistically distinct, at a significance level of greater than 99% ($p < 0.0001$).

GPR Facies A, characterized by weak to absent internal reflections, always correlates to thrombolite units with low porosity. Within this facies, porosity values for the 25 and 75% quartiles are 4.9% and 11.9%, respectively, with a mean porosity of 7.9%. Thus, the thrombolite bodies that make up GPR Facies A include little variability in porosity, with a standard deviation of 3.5%.

Zones exhibiting weak reflections, GPR Facies B, correlate primarily to units that have intermediate porosity. Porosity for the 25% quartile is 11.3% and the 75% quartile is 16.4%, with an average value of 15.0%. Lithologically, GPR Facies B includes all depositional facies, with 40% representing ooid grainstone, 37% are thrombolite and 23% are stromatolite. These data emphasize the absence of a simple relationship between depositional facies and GPR Facies B.

GPR Facies C, defined by strong reflections, typically correlates with units with high porosity, although variability exists within and between stratal units of this facies. Strata of GPR Facies C have mean porosity of 22.5%, and porosity for the 25 and 75% quartiles are 18.5 and 25.7, respectively. The dominant lithology correlating with areas of strong reflections is ooid grainstone, which comprises more than 52% of the samples. The remainder of samples from Facies C consists of 28% thrombolite and 19% stromatolite. As is the case with GPR Facies B, the diversity of depositional facies correlating to GPR Facies C shows there is not a simple relationship between depositional facies and GPR Facies B.

In sum, the results illustrate that whereas GPR Facies A shows a strong relationship between radar facies and depositional facies (correlating always to tight thrombolite units), lack of a systematic relation between depositional facies and GPR Facies B and C indicate that GPR Facies B and C cannot be used to image depositional facies (Table 5.2.) Instead, each radar facies includes statistically different porosity, an attribute which may be independent of depositional facies (compare with Figure 5.1).

An additional factor that could influence reflection strength, which define the GPR facies, is contrasts at interfaces; larger contrasts in dielectric properties at interfaces cause stronger reflection amplitudes (Davis and Annan, 1989; Lines and Newrick, 2004; Neal, 2004). Visual comparison of porosity from a densely sampled interval (Figure 5.9) clearly demonstrates the relationship between porosity and porosity variability and GPR facies. For example, areas of low porosity correlate with GPR Facies A. Areas with intermediate porosity and only moderate changes in porosity correspond to GPR Facies B. In contrast, areas of high or highly variable porosity correlate with GPR Facies C. These data unambiguously indicate the importance of porosity, which may or may not be related to depositional facies, on GPR character.

To more rigorously explore the influence of porosity contrasts on GPR facies, porosity changes between stratigraphically (vertically) adjacent samples were tallied within and among GPR facies (Figure 5.10, Table 5.3). A plot of the absolute value of changes in porosity across interfaces of samples from GPR Facies B and C (Figure 5.10) reveals that they are qualitatively distinct. The purpose of this analysis is to illustrate variability in porosity and variability in radar signature and their relations, not the cause

of any one particular reflection. Samples were not collected with that purpose in mind, nonetheless, co-rendering these data illustrate several important relationships.

For example, GPR Facies B is characterized by intermediate reflection strength, and includes strata with a mean porosity change between adjacent samples of 6.6% and a standard deviation of 5.3%. In marked contrast, GPR Facies C, represented by strong reflections, has a mean porosity change of 12.5% with a standard deviation of 7.7. Collectively, changes in porosity across interfaces above and within GPR Facies C are greater than those of GPR Facies B. These data are consistent with the interpretation that variations in reflection strength are caused by changes in porosity as EM waves travel through the succession.

These qualitative relations can be explicitly tested. Quantitative analysis (nonparametric Mann-Whitney) reveals that populations of measured variations in porosity (Figure 5.10) between GPR Facies B and C are statistically distinct at a significance level of greater than 99% ($p < 0.0029$), consistent with the qualitative trends. (GPR Facies A included too few transitions to statistically test for relationships.)

An additional quantitative analysis was carried out to determine the relation between porosity and GPR reflection amplitude magnitude. Quantitative data of the reflection amplitude magnitude correlating to thin section samples were obtained by calculating the root mean square (RMS), which is the square root of the mean of the squares of the values (Equation 3), of the reflection amplitude for each thin section sample to determine the relationship between porosity and the magnitude of reflection amplitude (Figure 5.11).

$$R_{rms} = \sqrt{(R_1^2 + R_2^2 + \ldots\ldots + R_n^2 / n)} \quad (3)$$

where R is the magnitude of the reflection amplitude and n is the number of values. To determine the RMS of the magnitude of the reflection amplitude, the location of the thin section samples on the 50 MHz GPR profiles was identified on each GPR profile. Then, the RMS of the reflection amplitudes was calculated from a time interval corresponding to a thickness of 0.9 m and containing three adjacent traces (1.5 m lateral distance).

A source of uncertainty in this analysis is that the GPR averages properties within an interval that is one quarter of a wavelength, which is 0.61 m for 50 MHz data (refer to chapter 4.6, *Resolution Identification*). Another major assumption is that the thin section properties are the same for the interval as well. These uncertainties may explain why there is not a strong correlation, however, there is a trend illustrating that typically the greater the magnitude of the reflection amplitude, regardless of rock type (Figure 5.11B), the greater the corresponding porosity value will be.

Table 5.1. Summary of relations between GPR facies and porosity.

GPR Facies	Number of Samples	Mean Porosity	Standard Deviation	25% Quartile	75% Quartile
A	11	7.9	3.5	4.9	11.9
B	30	15.0	6.7	11.3	16.4
C	21	22.5	8.9	18.5	25.7

Table 5.2. Summary of relationship between GPR facies and depositional facies. Note that GPR Facies A correlates to dense thrombolite in every instance, whereas there is no clear relationship between GPR Facies B and C and depositional facies.

GPR Facies	Number of samples	% Dense thrombolite samples	% Vuggy Thrombolite samples	% Ooid grainstone samples	% Stromatolite samples
A	11	100	0	0	0
B	30	0.7	30.0	40.0	23.3
C	21	0.5	28.5	52.4	19.0

Table 5.3. Statistical summary of porosity contrasts between stratigraphically adjacent samples within and among GPR facies. In this table, data are based on absolute values of the differences between samples and the immediately overlying samples. Note GPR Facies C has a greater mean change in porosity and standard deviation. GPR Facies A included too few transitions to statistically test for relationships.

GPR Facies	Number of Samples	Mean Change in Porosity	Standard Deviation	25% Quartile	75% Quartile
B	17	6.6	4.9	3.7	7.1
C	19	12.5	7.7	8.1	17.7

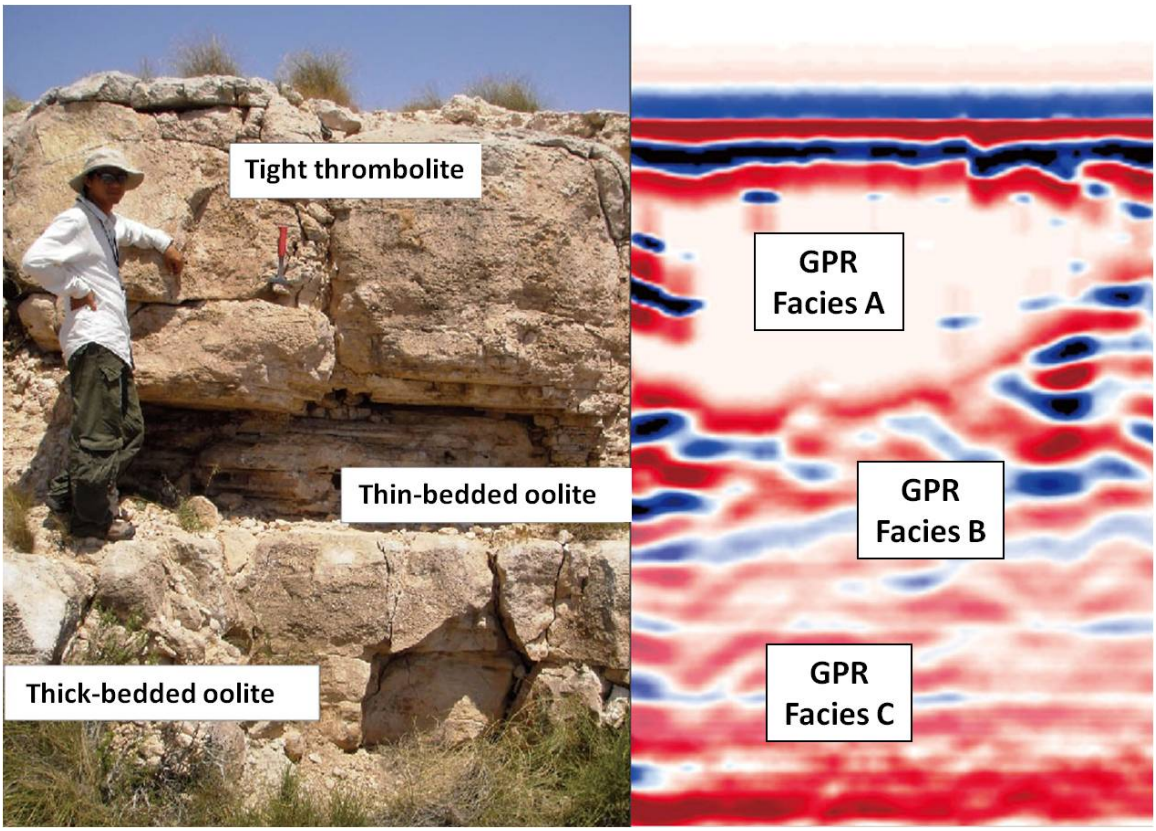

Figure 5.5. Example of calibration of 100 MHz GPR profile to the outcrop. The massive portion of the outcrop nearest the surface correlates well with GPR Facies A (very low porosity - tight thrombolite). Bedded oolite underlying the thrombolite body causes intermediate to strong reflections. Correlation of the radar reflections to the outcrop was critical for accurate interpretation of the profiles away from outcrops.

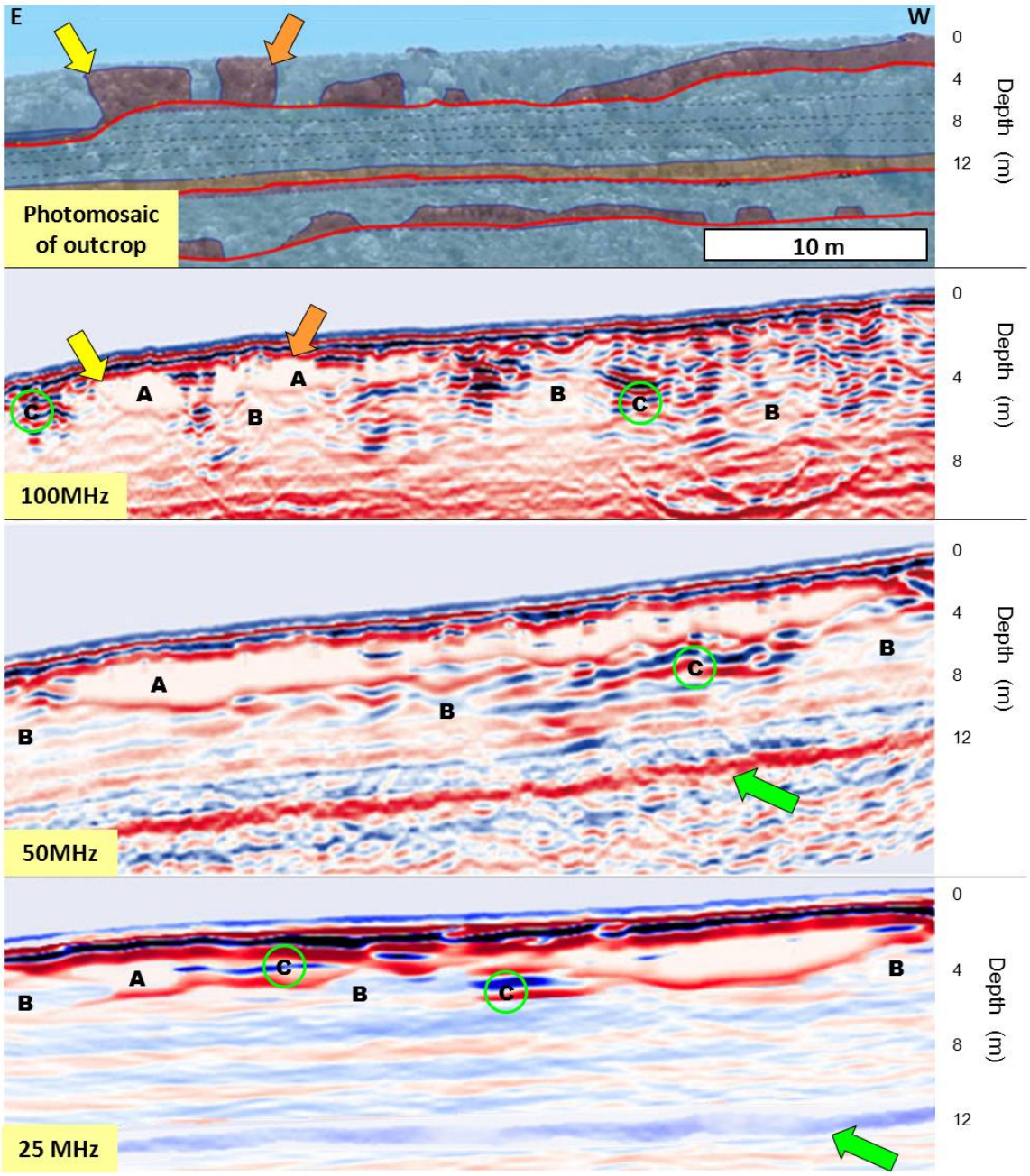

Figure 5.6. Relations between outcrop-scale lithologic changes and GPR facies. Outcrop photomosaic (Lipinski, 2009) compared to corresponding GPR profiles and radar facies (A, B, C-with green circles), from all three frequencies. The photomosaic is highlighted with different colors to emphasize varying lithologies (brown = thrombolite, light blue = oolite.) The individual thrombolite bodies correspond closely with GPR Facies A (very low porosity - tight thrombolite) in the 100 MHz profile. Yellow and orange arrows show thrombolite bodies that appear to change morphology subtly between the outcrop face and 2 m to the interior where the GPR profile was collected. The 50 and 25 MHz profiles offer lower resolution than the 100 MHz data, but are capable of penetrating deeper and imaging larger-scale features, such as sequence boundaries (e.g. prominent reflector (green arrow) at 12 m depth on 25 and 50 MHz profiles).

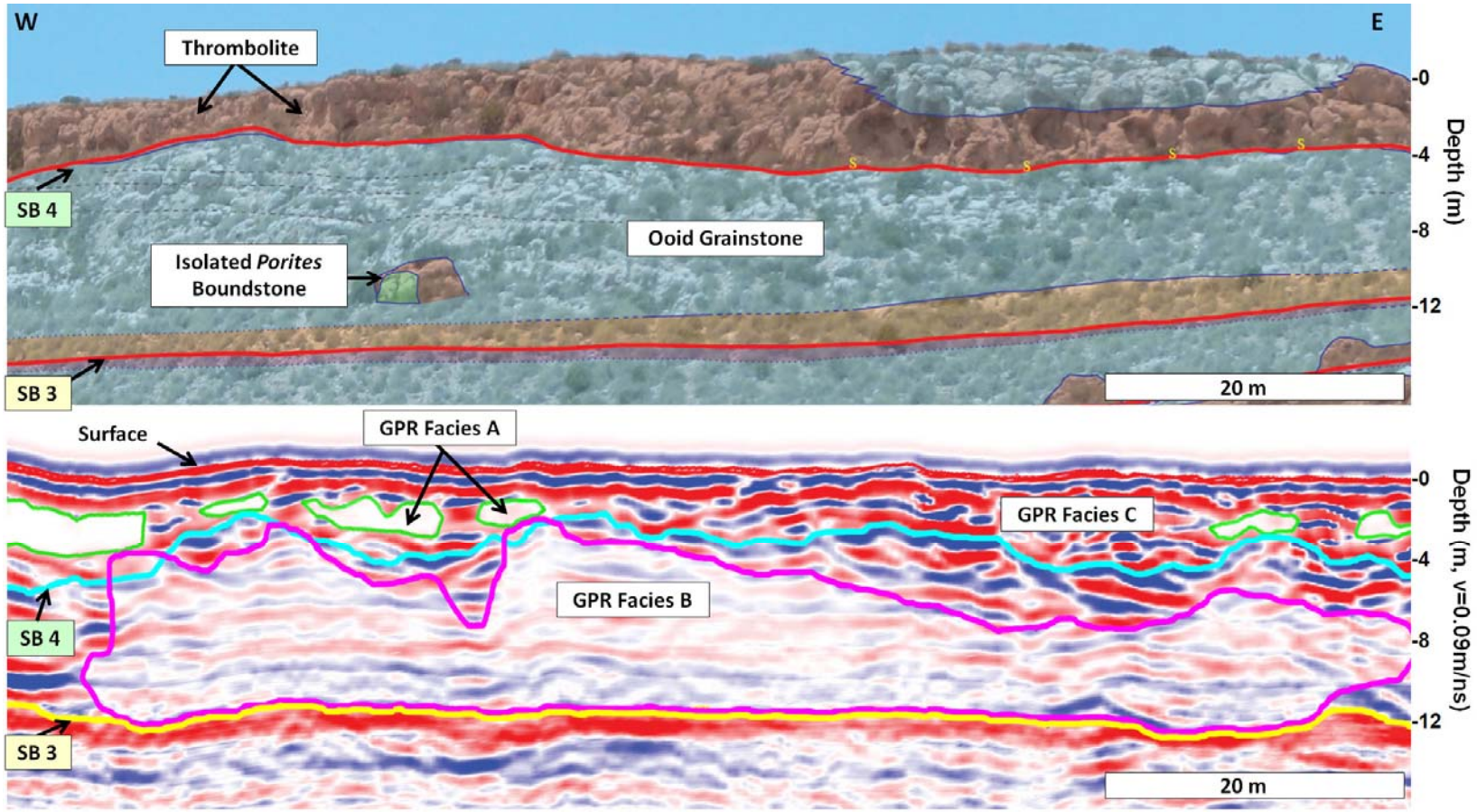

Figure 5.7. Comparison of a representative 50 MHz profile to outcrop. Outcrop photomosaic (Top; Lipinski, 2009) and corresponding GPR profile. Depositional facies are shaded on photo; brown represents thrombolite, blue represents ooid grainstone and sequence boundaries are shown in red. On GPR profile, Sequence Boundary 4 is shown in blue, Sequence Boundary 3 is shown in yellow, GPR Facies A is outlined in green, GPR Facies B is outlined in pink and GPR Facies C comprises the rest of the profile. Note there is a close correspondence between sequence boundaries, whereas there is not as close of relationship between GPR facies and depositional facies.

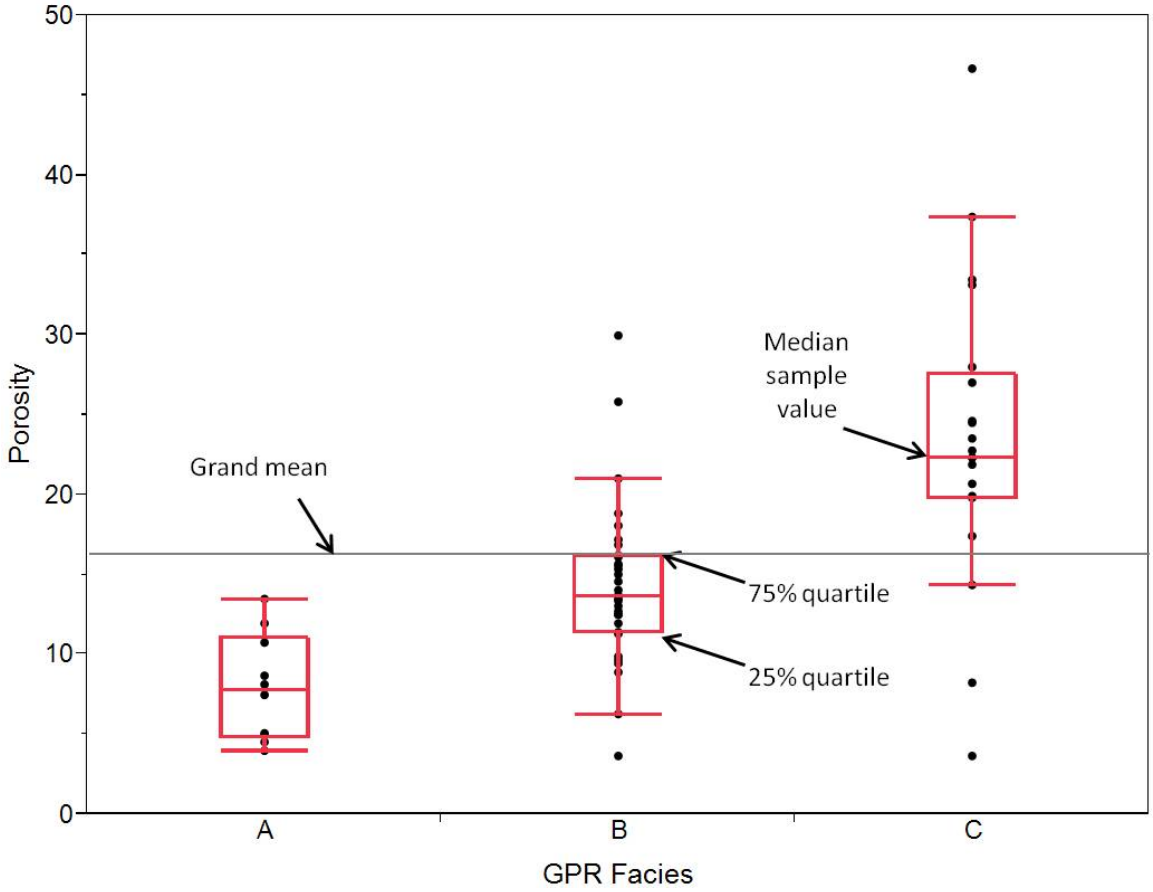

Figure 5.8. Relationship between porosity and radar facies. Data included in the red boxes falls in the interquartile range, which is the difference between the 1st and 3rd quartiles (25th and 75th quartiles). The bars on either side of the red boxes extend to the 5th and 95th percentiles. Note GPR Facies A includes lower values of porosity; whereas GPR Facies B and C typically have higher values of porosity. GPR Facies C has the most variability in porosity.

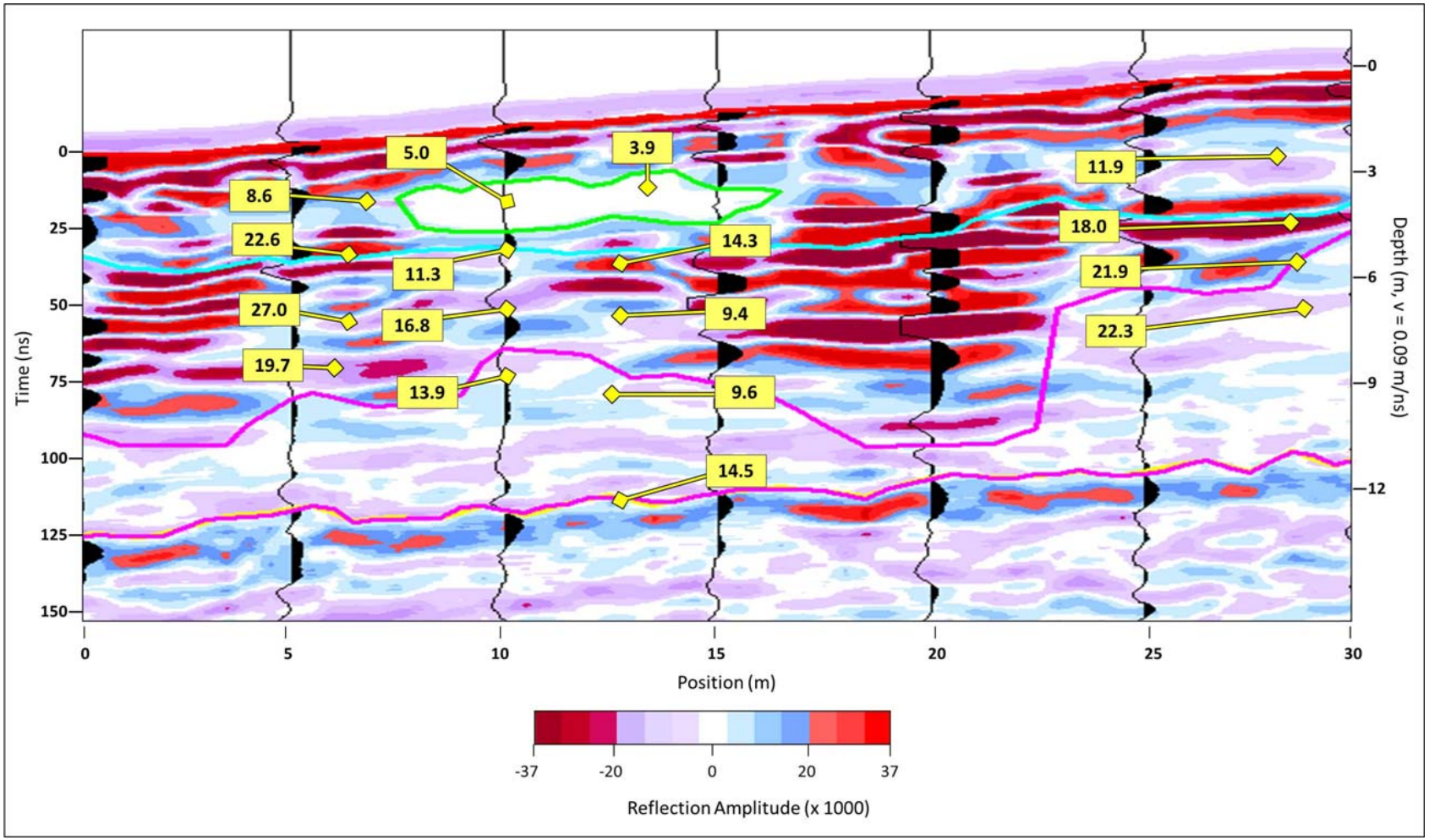

Figure 5.9. Relations between porosity and GPR facies, illustrated on a 50 MHz profile adjacent to an outcrop. On this plot, absolute values of reflections with high amplitude are shown in red colors and reflection with intermediate amplitude are shown in blue colors; low amplitude areas are white (GPR Facies A) and highlighted in green in the data. GPR Facies B is outlined in pink and GPR Facies C comprises the rest of the profile. Note that porosity, and variations in porosity, are lowest in areas with low amplitude. Intermediate porosity (typically between 10 and 20%) values are typically found in areas with moderate reflection strength (blues). Areas with strong reflections (reds) typically have high porosity or high changes in porosity.

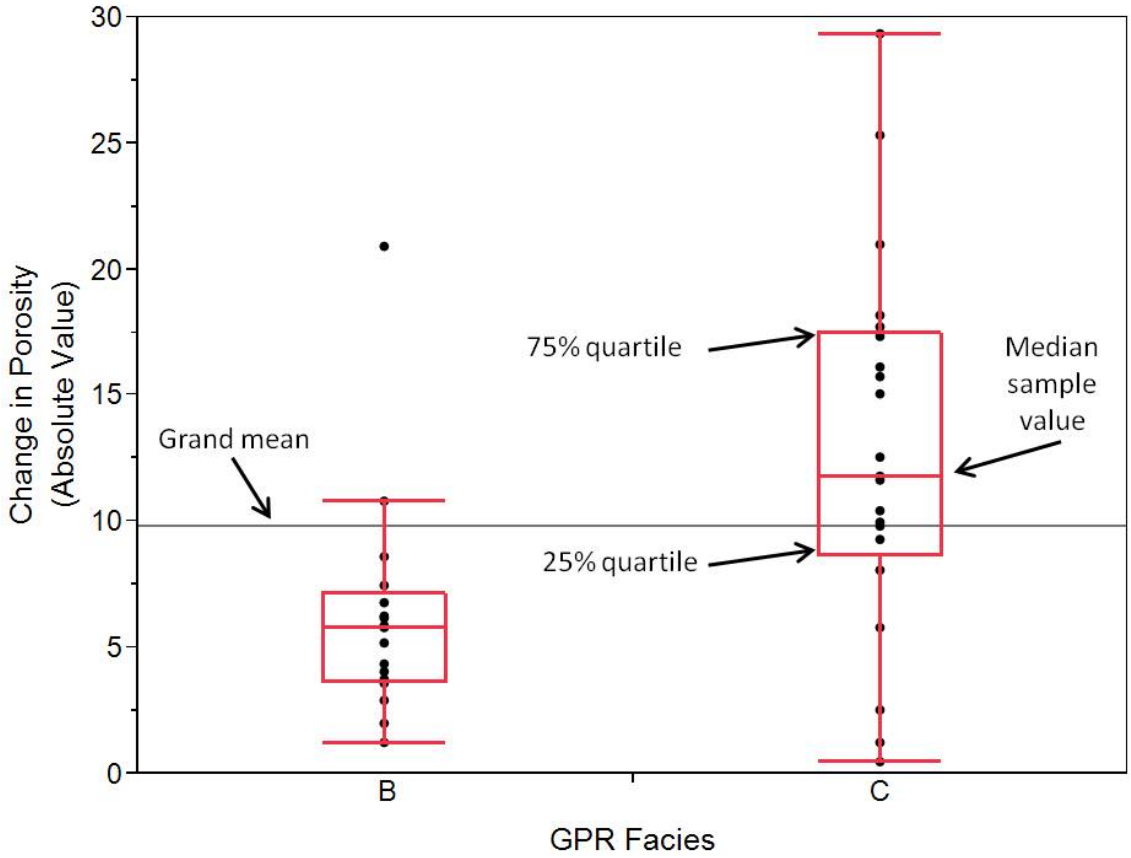

Figure 5.10. Relation between GPR facies and change in porosity between adjacent samples. Note that GPR Facies C has a greater overall range in changes in porosity in addition to a higher mean porosity change. Box and whisker bounds are the same as Figure 5.8. GPR Facies A included too few transitions to statistically test for relationships and is not illustrated.

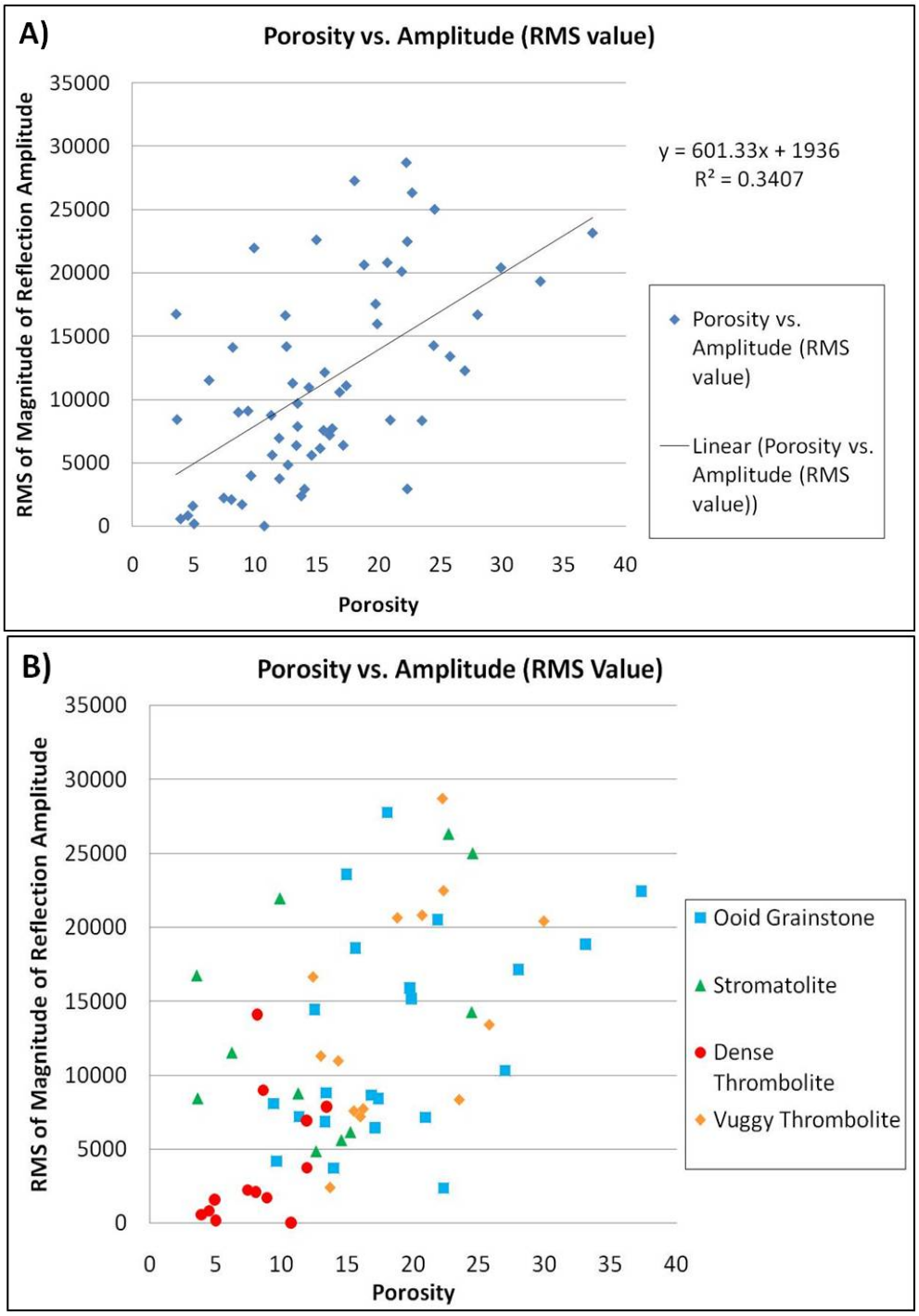

Figure 5.11. Relation between porosity and RMS of the magnitude of reflection amplitude for thin section samples. Note that outliers beyond the 5th and 95th quantiles were not included in these analyses. A.) Plot of porosity vs. RMS of reflection amplitude for thin section samples. Note there is a trend of greater porosity corresponding to greater RMS reflection amplitude magnitudes. B.) Plot of porosity vs. RMS of reflection amplitude for thin section samples showing the lithologies of each sample. Note that dense thrombolite samples tend to have low RMS reflection amplitude values (red dots) whereas the other lithologies display a wide range in porosity. The same general trend of greater porosity values corresponding to greater RMS reflection amplitude magnitudes is seen for all rock types.

5.4: Distribution of GPR Facies in 3D

To recognize and map GPR facies in 3D more systematically, a suite of objective, reproducible criteria (specifically, amplitude and continuity of reflections), were defined (Figure 5.12). The first step in mapping GPR facies was identifying correlations between prominent reflections and character in GPR profiles and geologic features evident on adjacent outcrops. These features were then correlated among profiles. The most prominent reflection, located at a depth of approximately 12 m, was mapped first in all 25 and 50 MHz profiles, and formed the base of the study interval at a consistent depth of approximately 12 m, which matches the depth of Sequence Boundary 3 as traced on outcrops along the perimeter of the survey site. This strong reflection can be found in all 25 and 50 MHz profiles throughout the entire area.

A less prominent, somewhat continuous reflection, located at depths ranging from 0 m to 6 m, was mapped in all frequencies as well. This reflection correlates to Sequence Boundary 4 and it was identified in the eastern part of all profiles throughout the survey area. To map this sequence boundary, the reflection correlating to this horizon was first located in profiles along the perimeter of the survey area, where GPR measurements were used to locate it in areas in which it was discontinuous or difficult to trace. Once the horizon was mapped in profiles along the perimeter it was tied to intersecting lines from the interior. This reflection corresponding to Sequence Boundary 4 would have been very difficult, if not impossible, to map if GPS measurements had not been collected along the outcrop.

These continuous reflectors that are tied to significant stratigraphic surfaces (sequence boundaries) provide a framework within which to analyze and map GPR

Facies A-C and compare them to geologic features. After mapping these major bounding reflections, the next step was mapping the lateral and vertical extent of the three GPR facies. Mapping in 3D revealed marked variations in the distribution and geometries of GPR facies throughout the survey area (Figures 5.13, 5.14) and that GPR facies vary spatially at several scales. At the largest scale, distribution of radar facies has a notable trend relating to topography (Figure 5.15). The updip portion of the survey area (western end) is dominated by weak reflections (GPR Facies B) with little variability in reflection strength. Downdip areas have more variation in radar signatures. This trend is observed in profiles of all frequencies throughout the survey area. An isopach map of GPR Facies B (Figure 5.16) clearly illustrates this trend.

The other GPR facies exhibit distinct patterns of distribution as well. For example, an isopach map of GPR Facies A (tight thrombolite) reveals variability in thickness, continuity and distribution throughout the survey area (Figure 5.17). Relative to GPR Facies B (Figure 5.16), this GPR facies is more patchily distributed, has a smaller range in thickness and shows no large-scale updip to downdip trends in abundance. Bodies of GPR Facies A appear to be largely discontinuous, with lateral extents of a few meters (less than 20 m) as is evident in profiles from the 3D grids (Figures 5.18, 5.19).

Whereas variations in distribution of GPR facies were evident in adjacent profiles in the coarse 2D grid (20 m by 20 m line spacing) that covered the entire survey area, the two 3D grids with 5 m line spacing illustrate an even more intimate level of detail of changing geometries of GPR facies. Three-dimensional grid data reveal significant lateral and vertical changes in GPR facies within distances of 5 m or less (Figures 5.18, 5.19). These abrupt changes, most evident in the distribution of the GPR Facies A (tight

thrombolite bodies), clearly illustrate the pronounced spatial variability that is common in this system, both in updip and downdip areas.

The conventional approach for subdivision and analysis of strata is on the basis of sequences. In this study, however, mapping in 3D reveals that GPR facies cut across stratigraphy in many instances (Figure 5.20) and the horizon representing the upper sequence boundary (Sequence Boundary 4) was discontinuously mappable (e.g., its location is ambiguous in some areas). Although not emphasized in previous GPR studies, this relationship is perhaps not surprising, given the observation that GPR facies are related to rock textures, which in turn reflect a complicated combination of depositional and diagenetic influences, as discussed above. The greatest permittivity contrasts may not occur at the sequence boundaries.

At the largest scale, volumetric analysis suggests that of the three main GPR facies (A-C), Facies A makes up 1.4% of the preserved part of the TCC between the modern-day surface and the base of Sequence 3. This likely represents a minimum estimate, as a grid with 20 m line spacing may have missed some of the small lateral bodies represented by GPR Facies A. Facies B composes 51.1%, and the rest of the survey is made up of Facies C (47.5%). Variability is present at a finer level of detail as well. Although GPR facies cut across sequence boundaries, volumetric analysis by sequence can provide information that is important for developing conceptual and quantitative models, especially populating reservoir simulation models. Volumetric analysis shows that Sequence 3 composes 83.8% of the survey area volume. It reaches a maximum thickness of 12.9 m and thins toward the east, where the minimum thickness is 6.0 m (Figure 5.21).

Sequence 3 is present over the entire survey area and is the best-preserved sequence imaged in this survey, although erosion has likely removed some of the uppermost part, especially in the western (updip) portions where it is exposed at the modern-day surface. The sequence has a stepped morphology; the relatively isopachous western (updip) and eastern (downdip) portions are separated sharply by a significant change in thickness in the central part of the survey area that trends north-south.

Within this sequence, GPR Facies A composes only a small amount (0.7%) of the total volume of this sequence and is found only in the updip parts of the survey area (Figure 5.22). The updip part of the survey area is dominated by GPR Facies B, whereas GPR Facies C is more common downdip where it frequently occurs stratigraphically above GPR Facies B (Figures 5.23, 5.24). Volumetrically, GPR Facies B comprises 55.6% of Sequence 3 and GPR Facies C makes up 43.2%. Isopachs of GPR Facies B and C show one or more possible linear to sub-linear trends. In areas with these trends, GPR facies boundaries are near-vertical, a character not ubiquitous throughout the survey area (Figure 5.25; see discussion below). Because GPR Facies A constitutes a volumetrically insignificant portion of this sequence, the facies proportion map for this sequence compares only GPR Facies B and C (Figure 5.26). This map clearly illustrates that the ratio of GPR Facies B to GPR Facies C is greater in the western (updip) portion of the survey area, whereas the opposite is true downdip. Thus, patterns of GPR facies proportions follow paleotopographic trends.

Sequence 4 is present only in the downdip portions of the survey area, where it reaches a maximum preserved thickness of 6.1 m (Figure 5.27). Modern erosional truncation has likely played a role in the present-day thickness distribution of this

sequence, removing it from the updip areas and perhaps some of the downdip areas as well, and it is not known how much was eroded. Nonetheless, within this sequence, distribution of GPR Facies A (Figure 5.28) makes up a larger proportion of Sequence 4 compared to Sequence 3 (4.9% compared to 0.7%). Similarly, distribution of GPR Facies B does not show clear cut linear trends or systematic changes in abundance in the sequence, although it composes a smaller volumetric proportion than in Sequence 3 (33.1% in Sequence 4 compared to 55.6% in Sequence 3; Figure 5.29). GPR Facies C composes 58.6% of Sequence 4 and appears to have a greater thickness in the central to eastern (downdip) part of the survey site (Figure 5.30). However, this apparent trend must be considered carefully, as a possible reason for this pattern of distribution may be due to the thicker preserved sequence in those areas. Because the top of the sequence has been eroded by an unknown amount, facies proportion maps were not generated for this sequence.

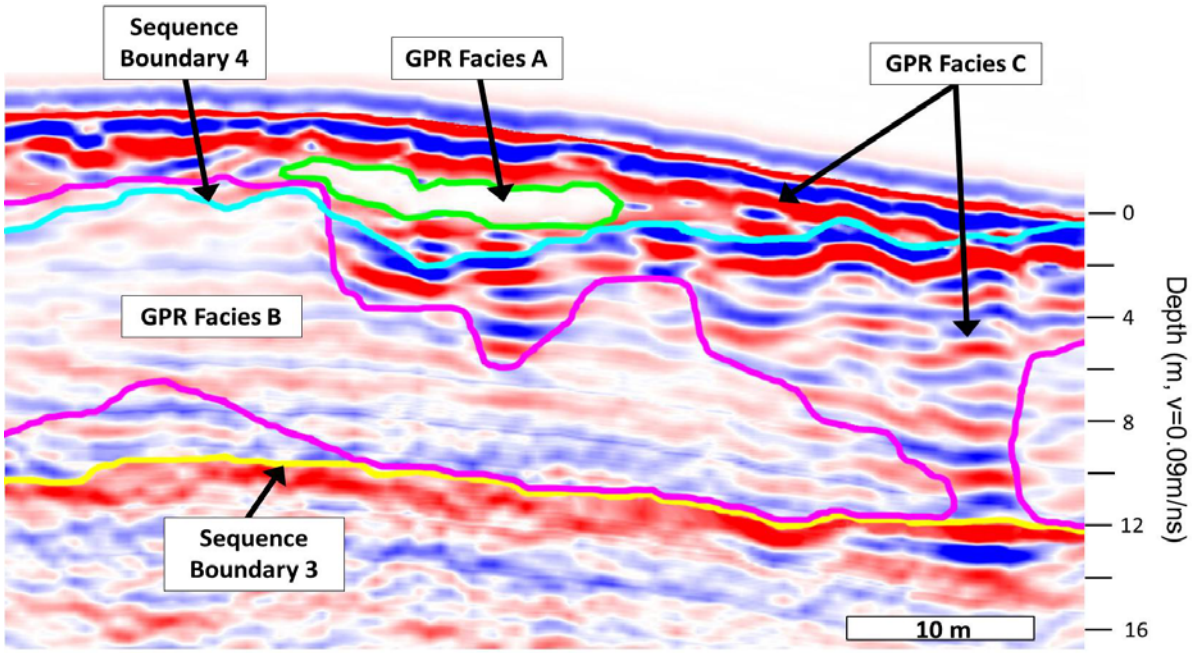

Figure 5.12. Representative 50 MHz profile illustrating the different GPR facies. Note GPR Facies B and C cut across Sequence Boundary 4. Note individual reflectors cut across the boundary between GPR Facies B and C, suggesting that these boundaries are digenetic rather than depositional as discussed below.

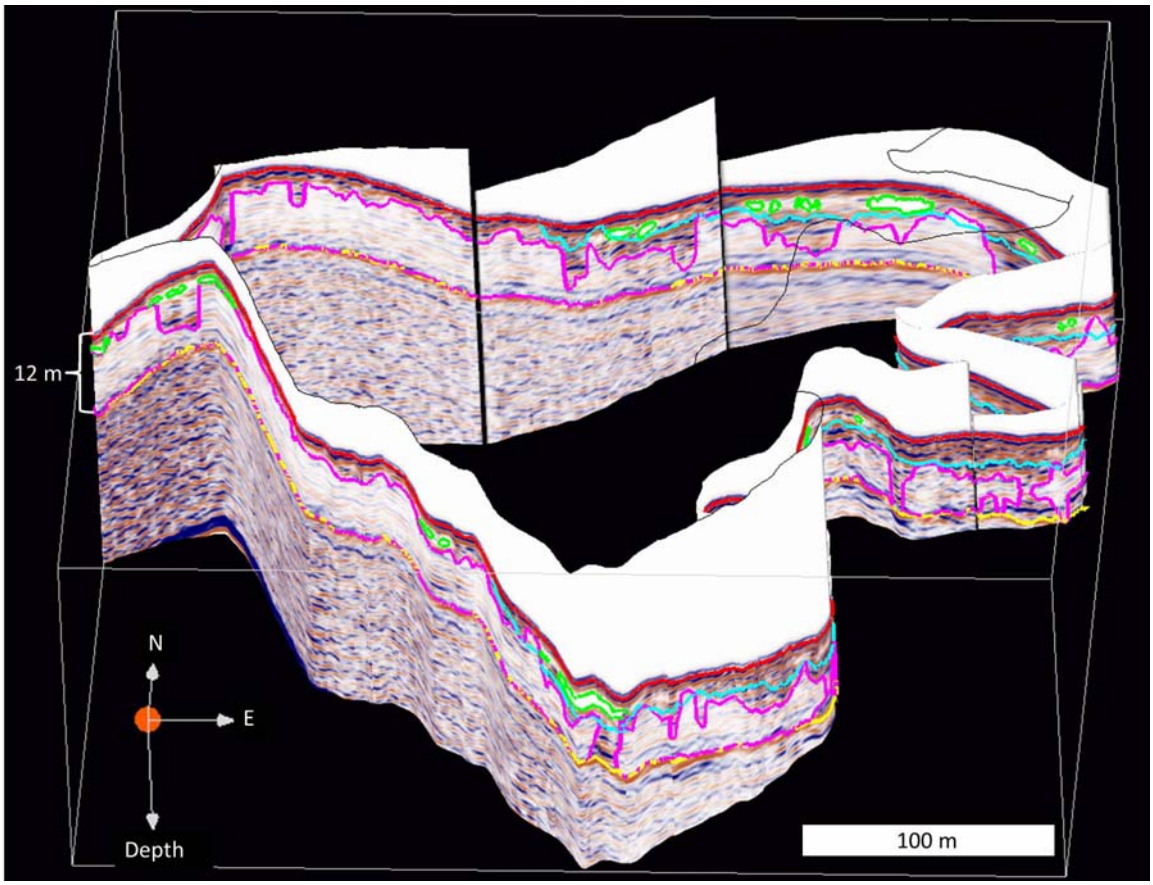

Figure 5.13. GPR profiles (50 MHz) along the perimeter of the survey area. The modern-day ground surface is highlighted in red, Sequence Boundary 4 in blue and Sequence Boundary 3 in yellow. These surfaces were identified through correlations of semi-continuous to continuous reflections to the outcrop. GPR facies were identified through analysis of GPR signal character. GPR Facies A is highlighted in green, GPR Facies B is outlined in pink and GPR Facies C comprises the rest of the profiles. Note in some areas that the boundaries between GPR facies appear near-vertical. Also of interest is the observation of the large-scale trend that GPR Facies B is thicker and more laterally continuous in the western part of the survey area than the eastern part and is commonly overlain by GPR Facies C. Also note the patchy distribution of GPR Facies A. On this 3D perspective plot the scale is accurate for the foreground but varies in the distance.

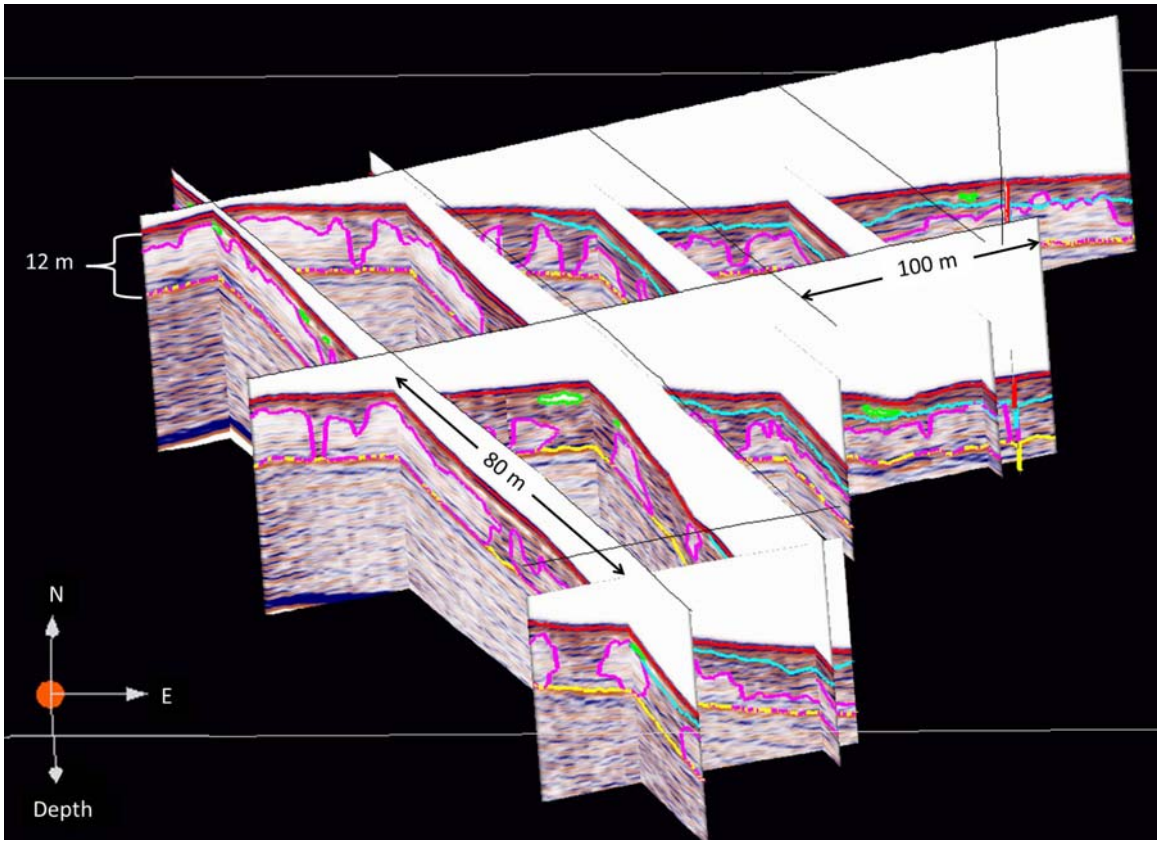

Figure 5.14. 50 MHz profiles from the interior of the survey area (2D grid) show the distribution of GPR facies. Color codes are the same as in Figure 5.12. Note that GPR Facies B (outlined in pink), correlating to weak reflections, is thicker in the western (updip) part of the survey area. Note several of the boundaries between GPR facies B and C are near-vertical to steeply sloping.

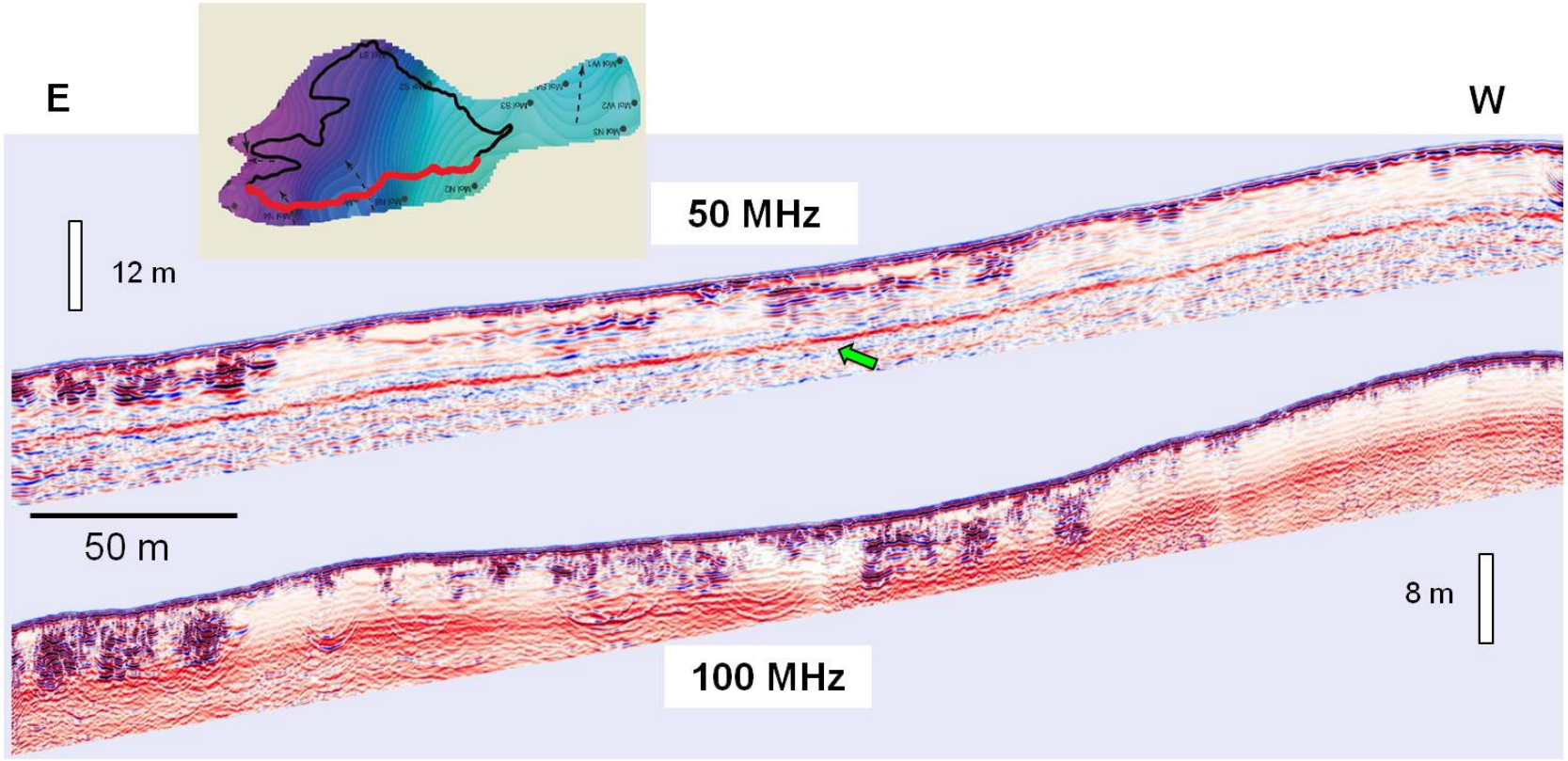

Figure 5.15. Large-scale changes in GPR character illustrated by 50 MHz and 100 MHz profiles from the northern perimeter of survey area. Red line on inset denotes location of transect in relation to paleotopographic and present-day surface. The western part of the survey area is approximately 30 m higher (blue shades) than the eastern end of the survey area (purple colors are lower elevations). Topographic corrections have been applied to the profiles. Note the updip portion of the survey area is dominated by weak reflections (GPR Facies B), whereas the downdip areas tend to have more variability in radar signature. Also, notice the strong, continuous reflection that corresponds to Sequence Boundary 3 in the 50 MHz profile (green arrow). Some of the boundaries between GPR facies B and C in the 100 MHz profile appear to be near-vertical to steeply sloping, giving the appearance of V-shaped geometric bodies of GPR Facies C.

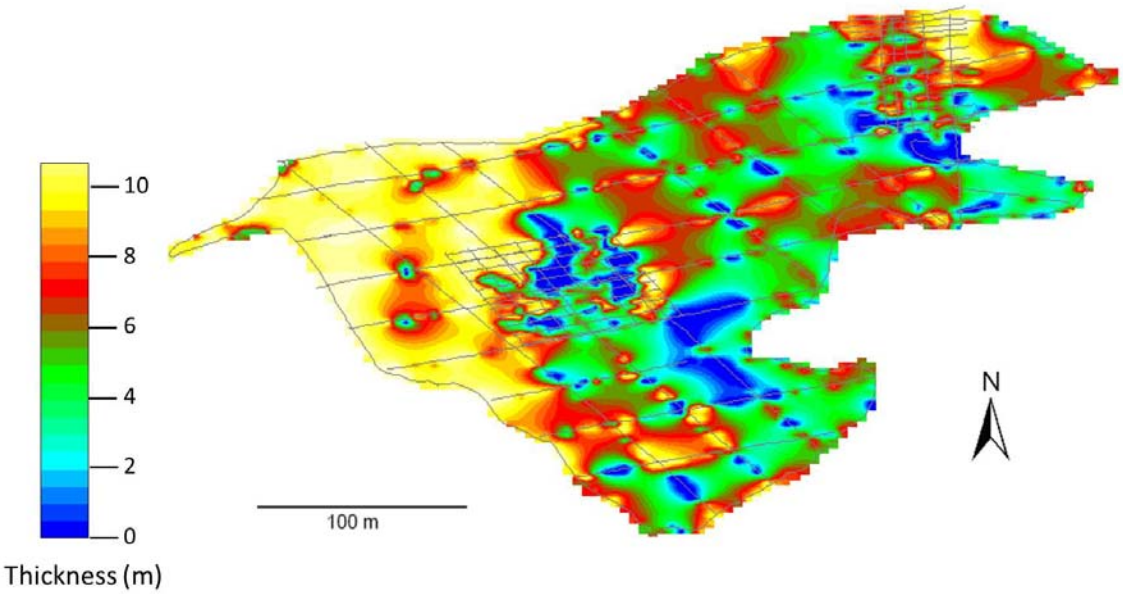

Figure 5.16. Isopach map of distribution and thickness of GPR Facies B (weak reflections correlating to intermediate porosity) between surface and base of Sequence 3 in 50 MHz data. Note that the distribution of this GPR facies is most prevalent and thickest in the updip (western) part of the survey area (red-yellow colors) and thins to absent (blue-green colors) towards the downdip (eastern) areas.

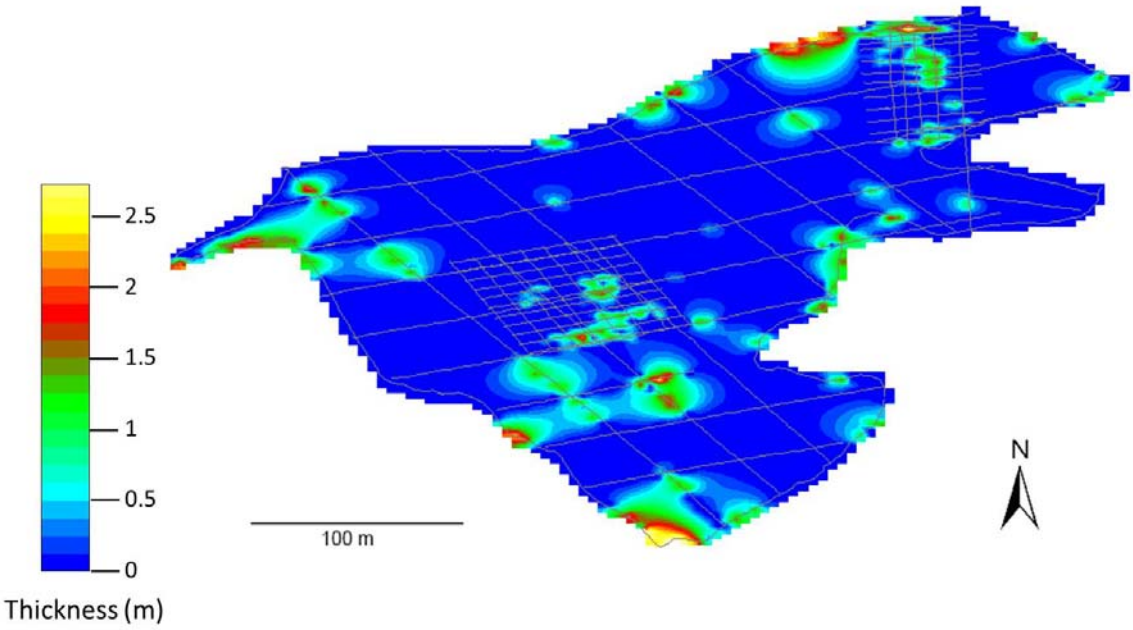

Figure 5.17. Isopach map of distribution and thickness of GPR Facies A (areas exhibiting absence of internal reflections, these correlate to tight thrombolite units) between surface and base of Sequence 3 in 50 MHz data. Note distribution is heterogeneous throughout the survey area and that it is a minor component volumetrically (1.4%). This likely represents a minimum estimate, as a grid with 20 m line spacing may have missed some of the small lateral bodies represented by GPR Facies A.

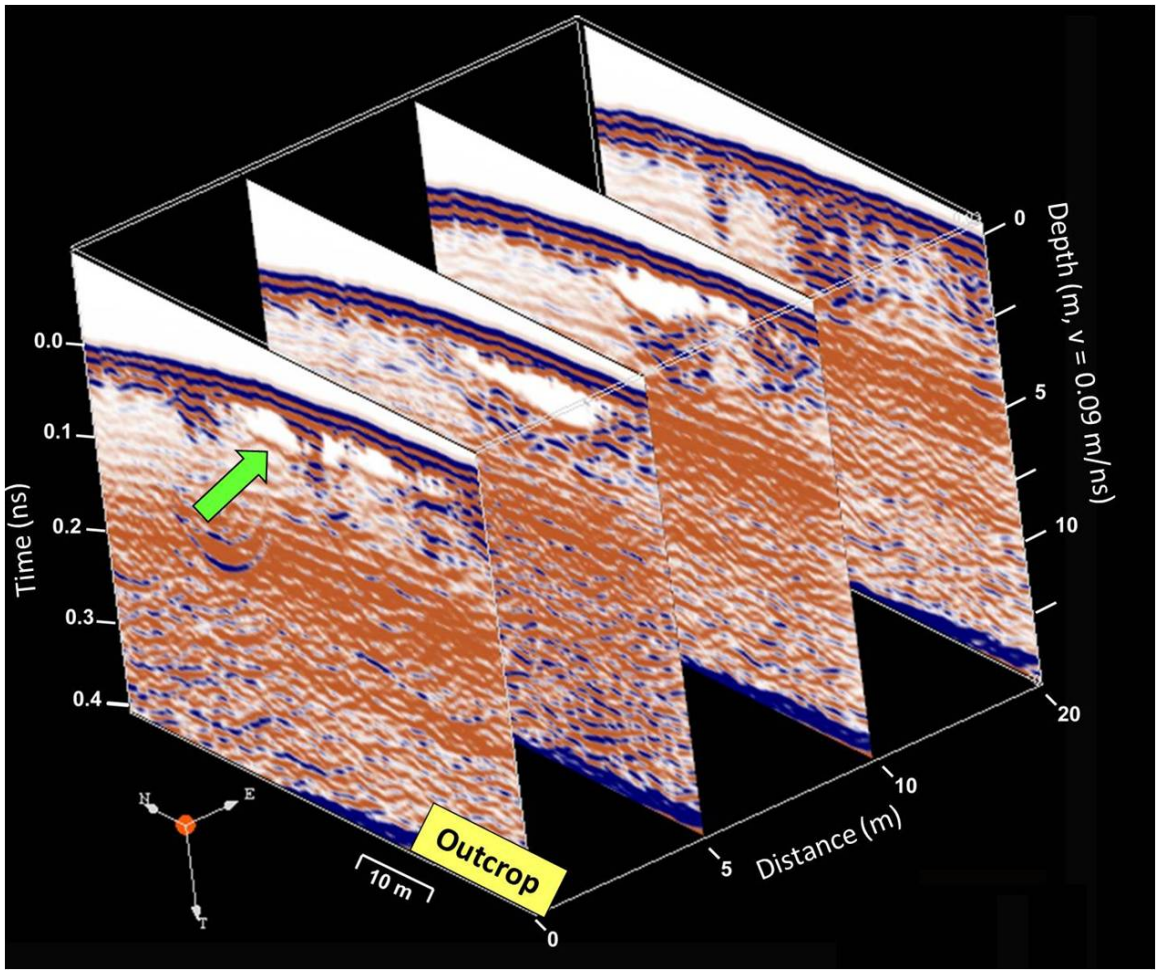

Figure 5.18. Three-dimensional data reveal changes in GPR facies away from outcrop exposures (left to right). These 100 MHz profiles are from Grid B, located in the downdip part of the survey area (see Figure 6). Note the changing geometry of GPR facies between the succession of parallel GPR profiles 5 m apart. The most notable change is in Facies A (green arrow), which is characterized as bright white zones in the GPR data; note how it is discontinuous away from the outcrop. Comparison of profiles with adjacent outcrops and thin sections shows that Facies A here represents tight thrombolite bodies.

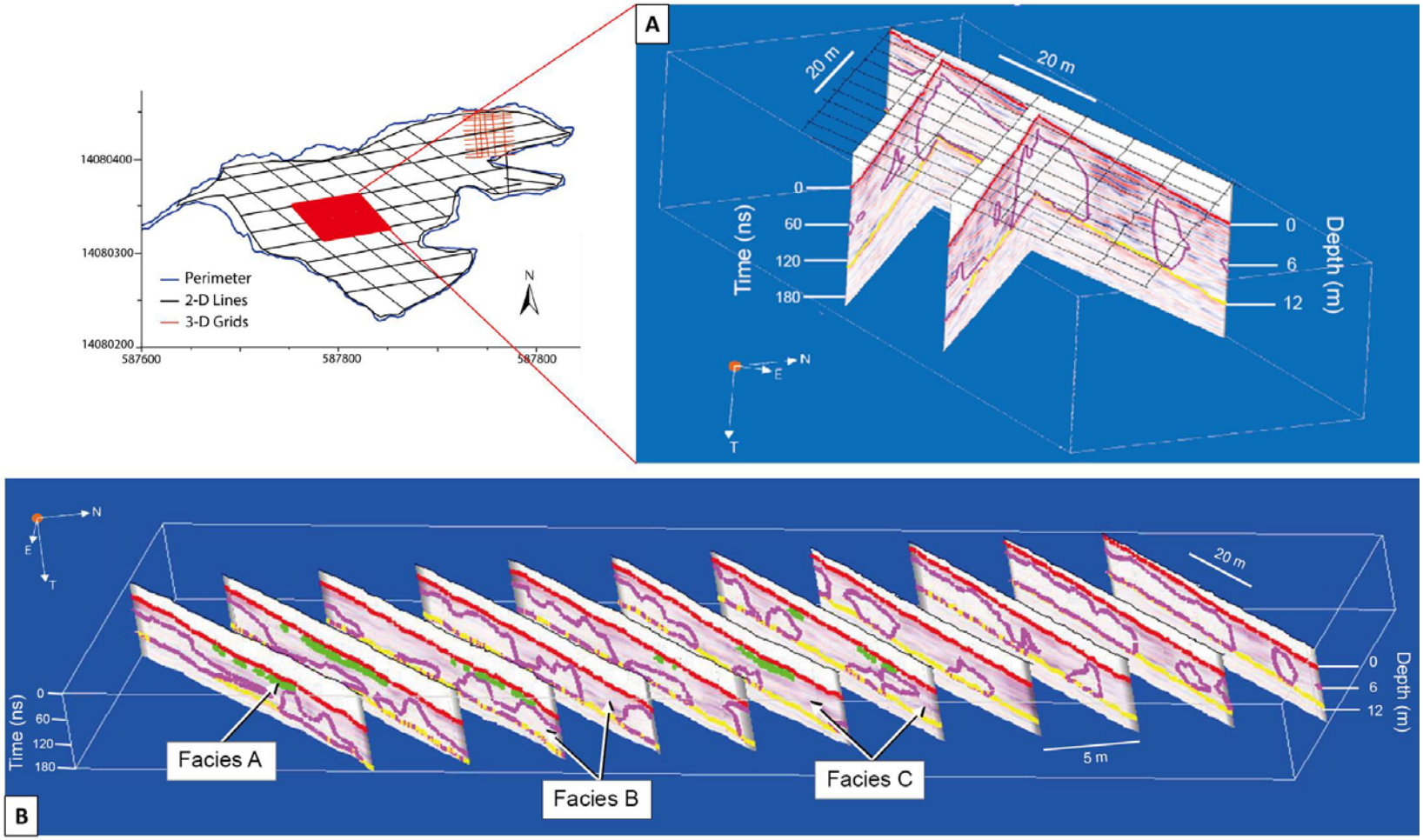

Figure 5.19. Larger-scale changes in GPR facies, expressed in 50 MHz profiles from the updip part of the survey area (Grid A, Figure 6). Facies A is outlined in green, Facies B in purple, and the rest of the profiles are composed of Facies C. The surface is highlighted in red and the base of Sequence 3 in yellow A) Intersecting GPR profiles facilitated interpretation and mapping geometries of GPR facies. B) A series of parallel lines with 5 m line spacing illustrates that abrupt changes in geometries and distribution of GPR facies occur in a short lateral distance (5 m or less). GPR facies mapped in 3D can provide information on volumetrics and spatial distribution of data.

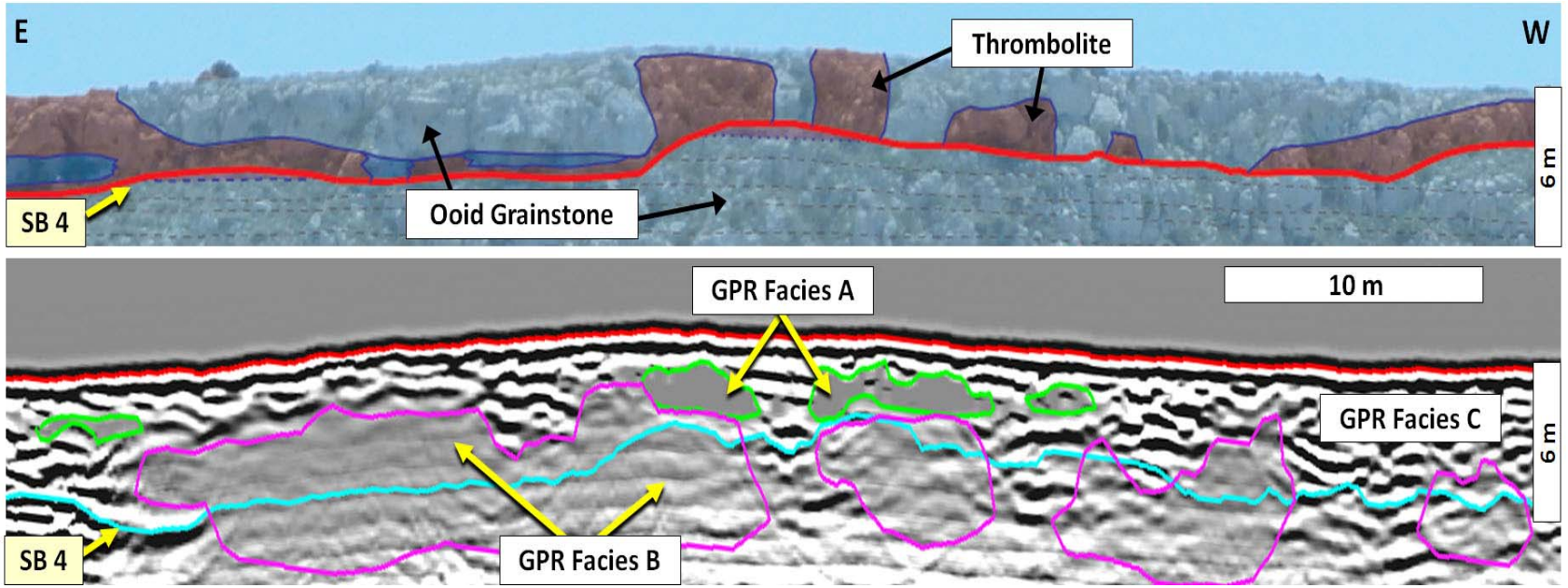

Figure 5.20. Relationship between GPR facies, sequence boundary and depositional facies. A) Outcrop photomosaic (Lipinski, 2009). Thrombolite units are colored brown, ooid grainstone is blue and sequence boundaries are red. B) Corresponding GPR profile (100 MHz) with interpretation of GPR facies. GPR Facies A is outlined in green, GPR Facies B is outlined in pink, GPR Facies C makes up the rest of the profile and Sequence Boundary 4 is highlighted in blue. Note that Sequence Boundary 4 cuts across GPR Facies B and C.

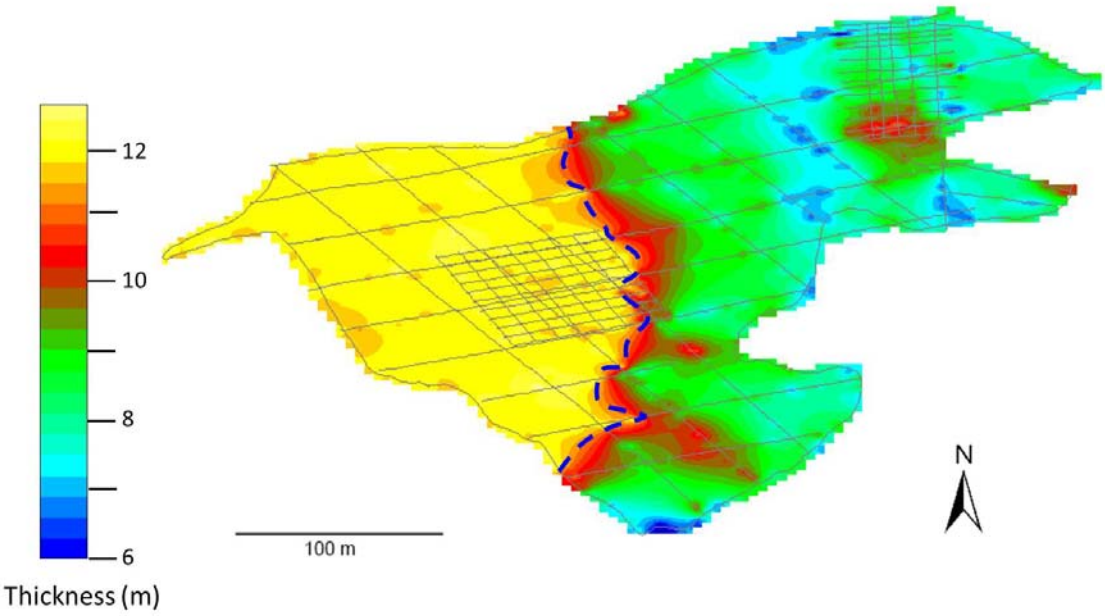

Figure 5.21. Isopach map of Sequence 3 (50 MHz data). Note that the sequence has a stepped morphology with a rapid change in thickness in the central part of the survey area, whereas the western (updip) and eastern (downdip) parts are relatively constant thickness. The thickest part of the sequence is approximately 12 m (yellow) in the western (updip) part of the survey area. Blue dashed line denotes location where Sequence 4 terminates. Note that this thickness change occurs in the same general area of a fault interpreted by Lipinski (2009; Figure 5). GPR data reveal no unambiguous evidence of a fault; instead, this thickness change is interpreted to represent paleotopographic variability (see discussion, 6.1).

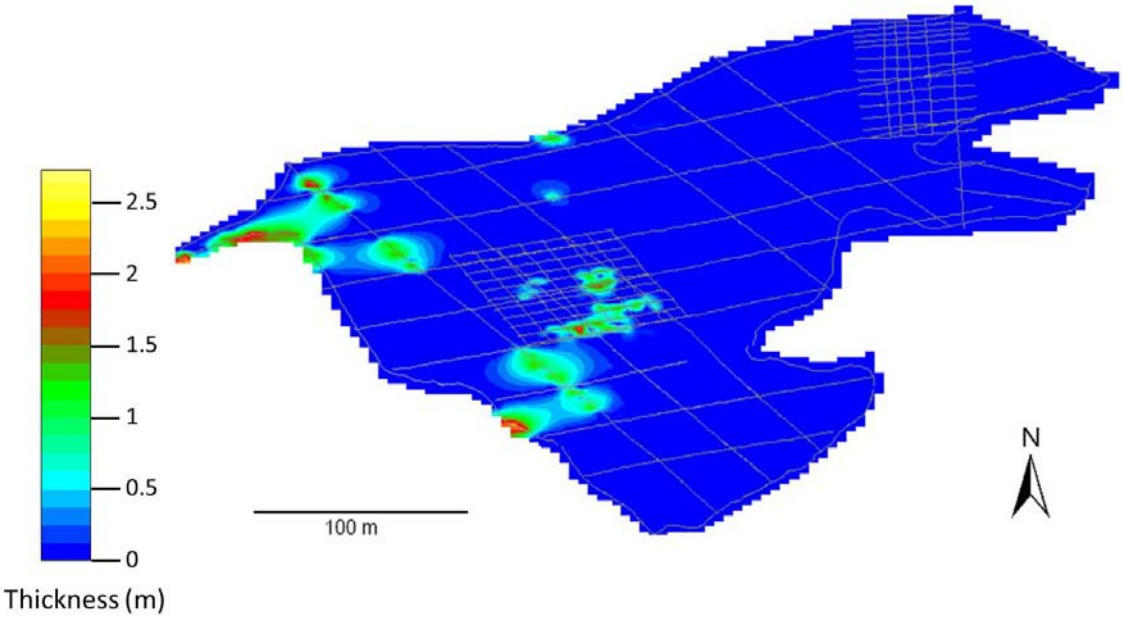

Figure 5.22. Isopach map of GPR Facies A in Sequence 3 (50 MHz data). This GPR facies is only present in the western (updip) portion of Sequence 3 and where present, distribution is sporadic.

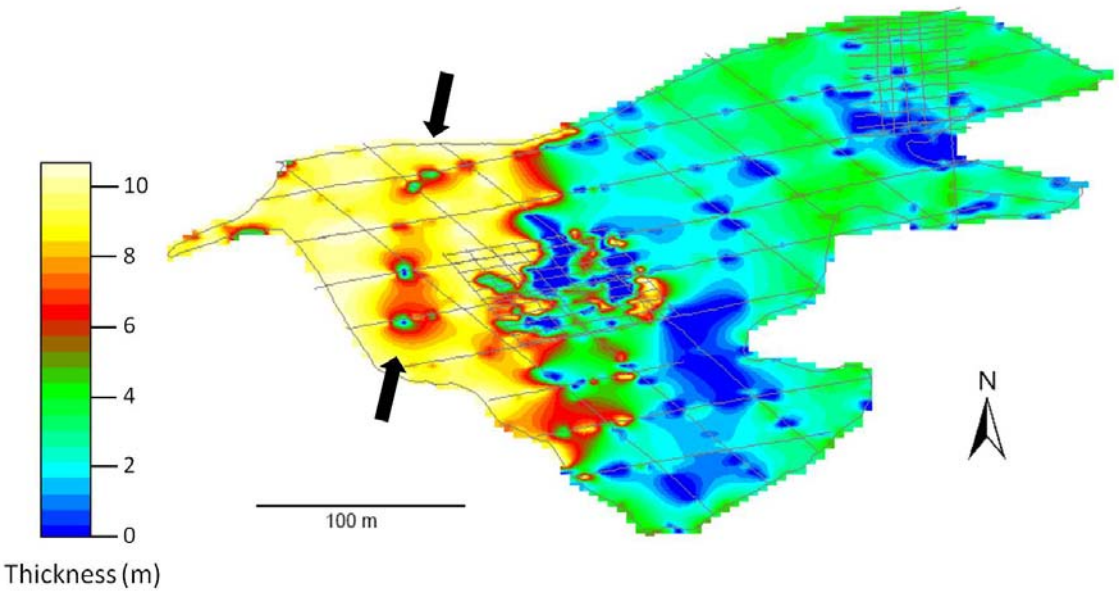

Figure 5.23. Isopach map of GPR Facies B in Sequence 3 (50 MHz data). Note that GPR Facies B is thickest and most continuous in the western (updip) part of the survey area. Distribution of this GPR facies is sparser and thinner to absent to the east. Black arrows point to one of the apparent linear to sub-linear trends; a line across this area is illustrated in Figure 5.24.

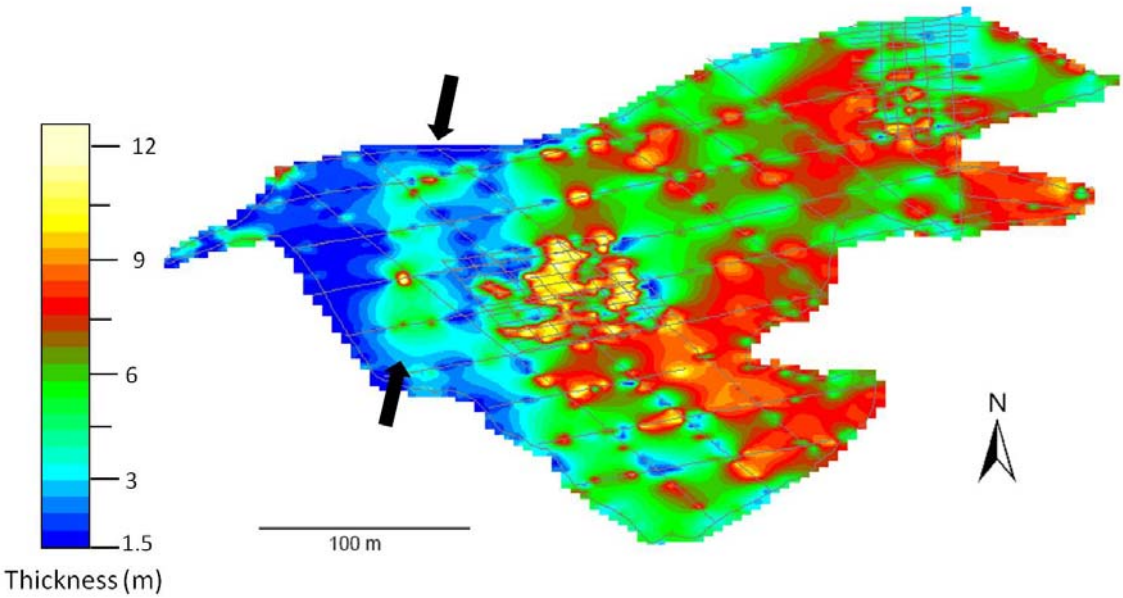

Figure 5.24. Isopach map of GPR Facies C in Sequence 3 (50 MHz data). Distribution shows that this GPR facies is thinnest in the western (updip) part of the survey area but is variable throughout the survey area. Black arrows point to an apparent linear to sub-linear trend; a line across this area is illustrated in Figure 5.24.

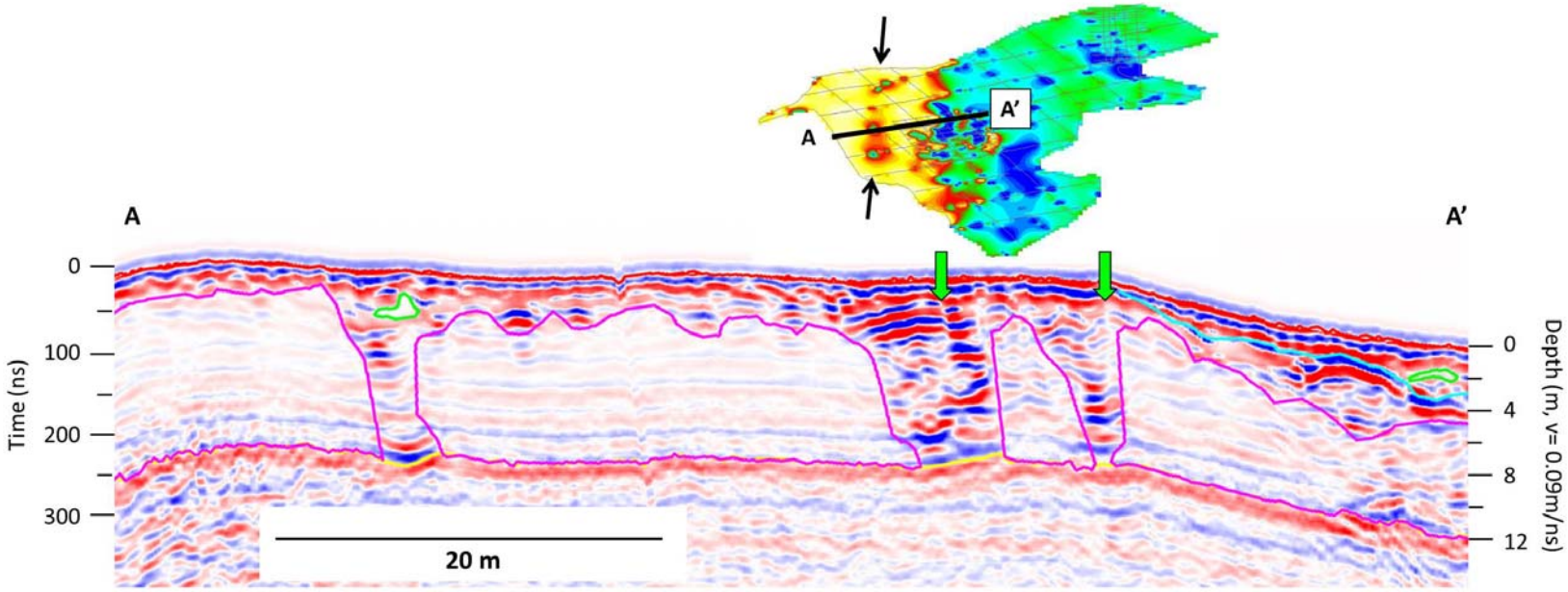

Figure 5.25. 50 MHz profile from the interior of the survey area (location of profile A- A' shown in inset map) that intersects a possible linear trend in the western (updip) part of the study site. Note the near-vertical boundaries between GPR facies in this profile. Green arrows point to reflectors that appear to be offset, exhibiting a sharp, vertical pattern that is likely caused by a fracture.

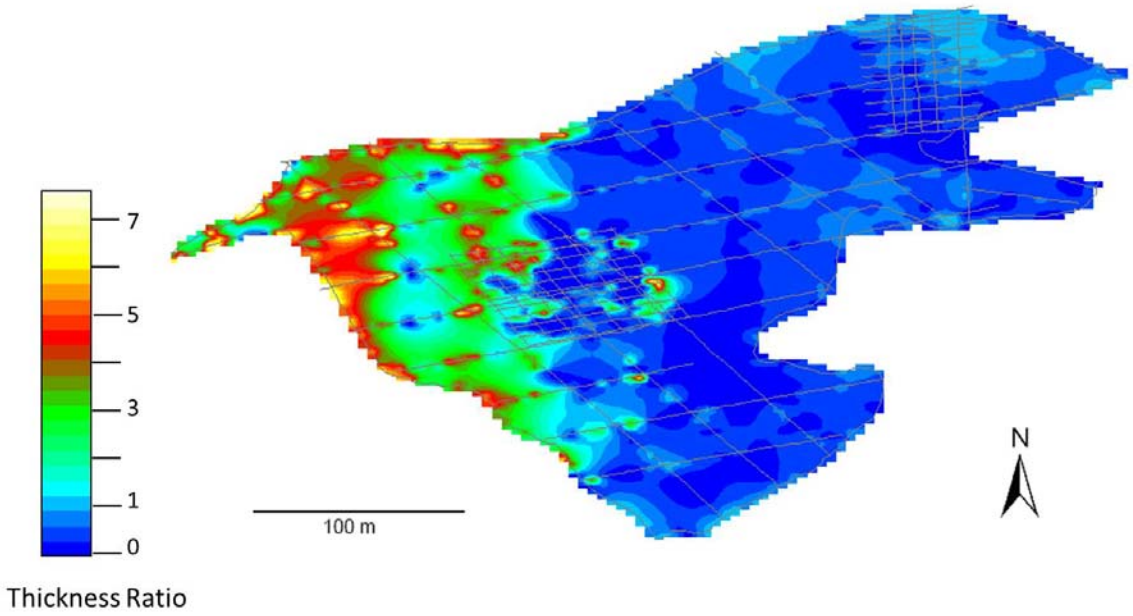

Figure 5.26. Map of the ratio of the thickness of GPR Facies B to GPR Facies C in Sequence 3 (50 MHz data). In this map, a value greater than 1 means that the thickness of GPR Facies B is greater than GPR Facies C at that location, whereas a value less than 1 means the opposite. Note that the thickness ratio of GPR Facies B to GPR Facies C is much higher (up to 7 times more likely in some areas) in the western (updip) portion of the survey area. This map illustrates the changing probabilities of encountering different GPR facies across the study area.

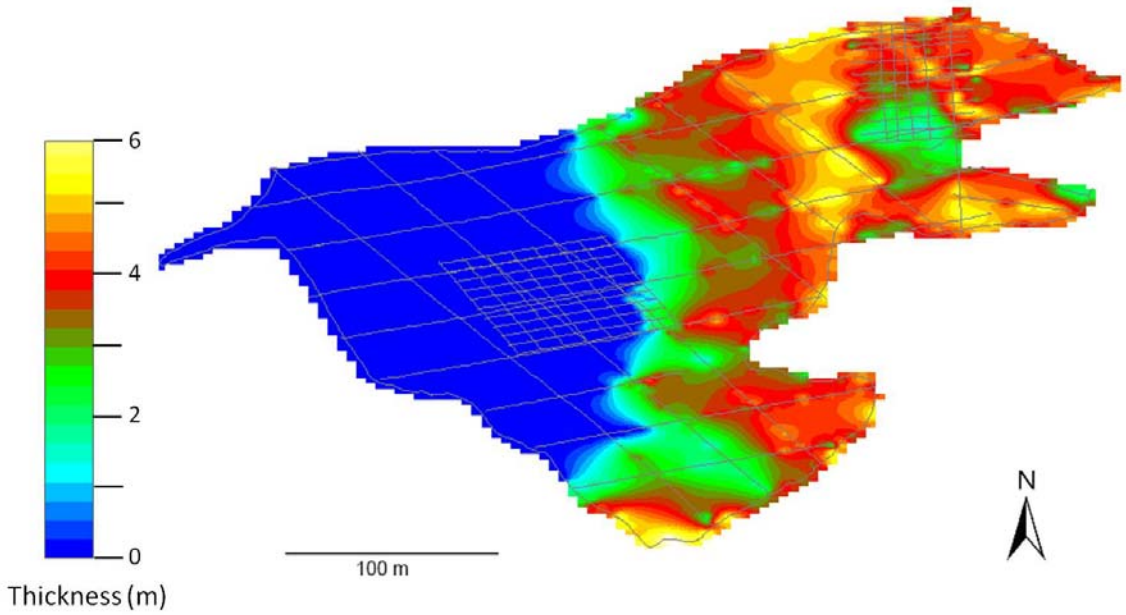

Figure 5.27. Isopach map of Sequence 4 (50 MHz data). Note the thickest parts of the sequence are found downdip.

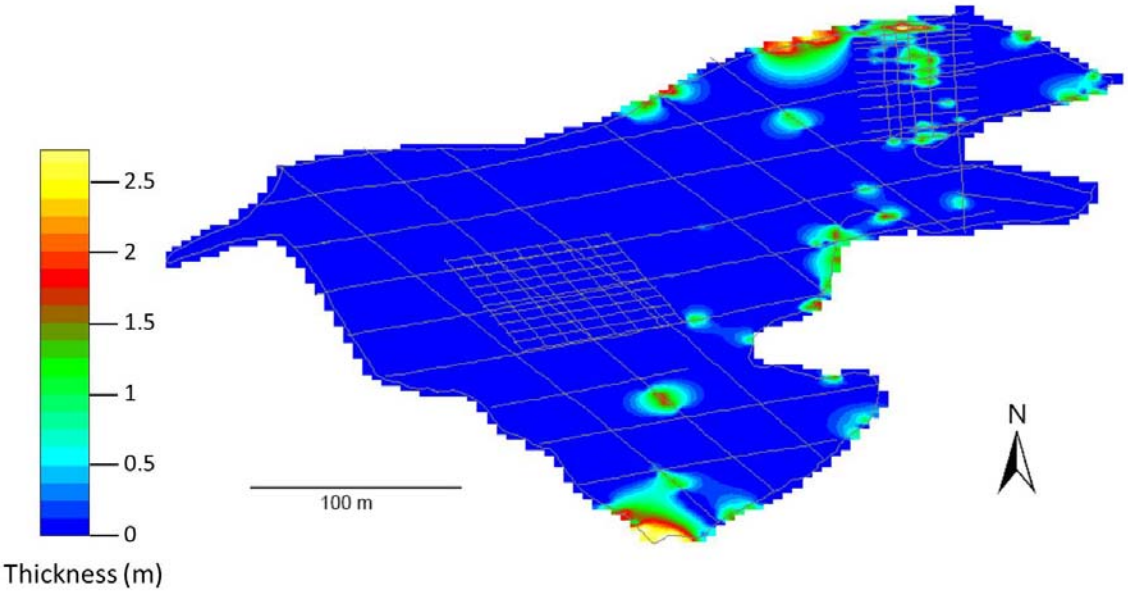

Figure 5.28. Isopach map of GPR Facies A, corresponding to tight thrombolite bodies, in Sequence 4 (50 MHz data). Note distribution is intermittent throughout the sequence and the maximum thickness of these bodies is less than 3 m.

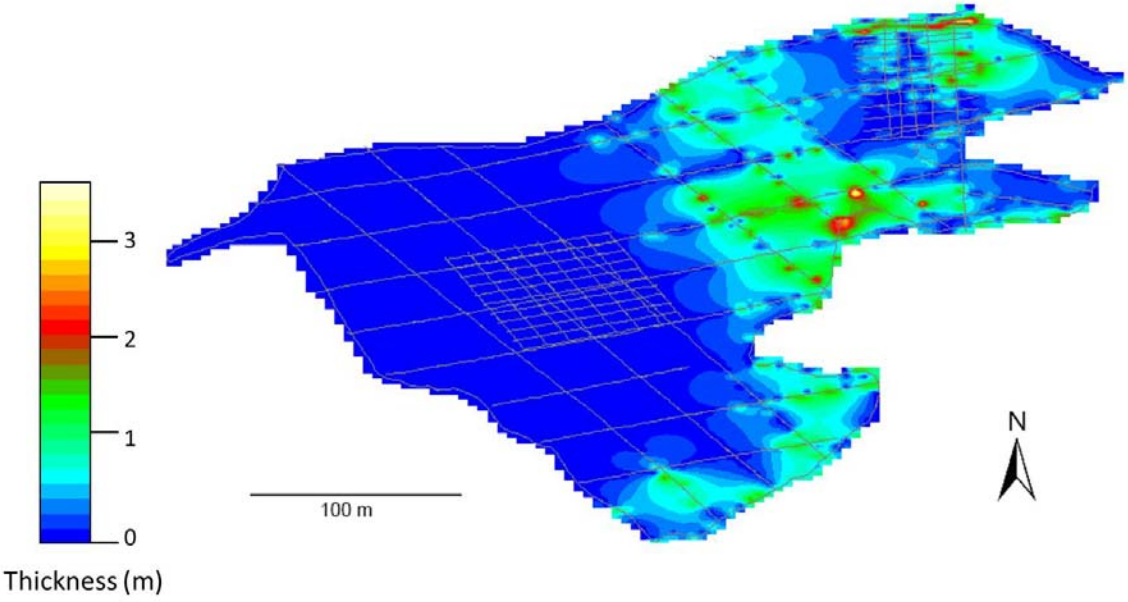

Figure 5.29. Isopach map of GPR Facies B in Sequence 4 (100 MHz data). Where present, the thickness of this GPR facies is approximately 1 m in most areas, but can reach a thickness of 3 m locally. Distribution of this GPR facies does not appear to follow any evident linear trends.

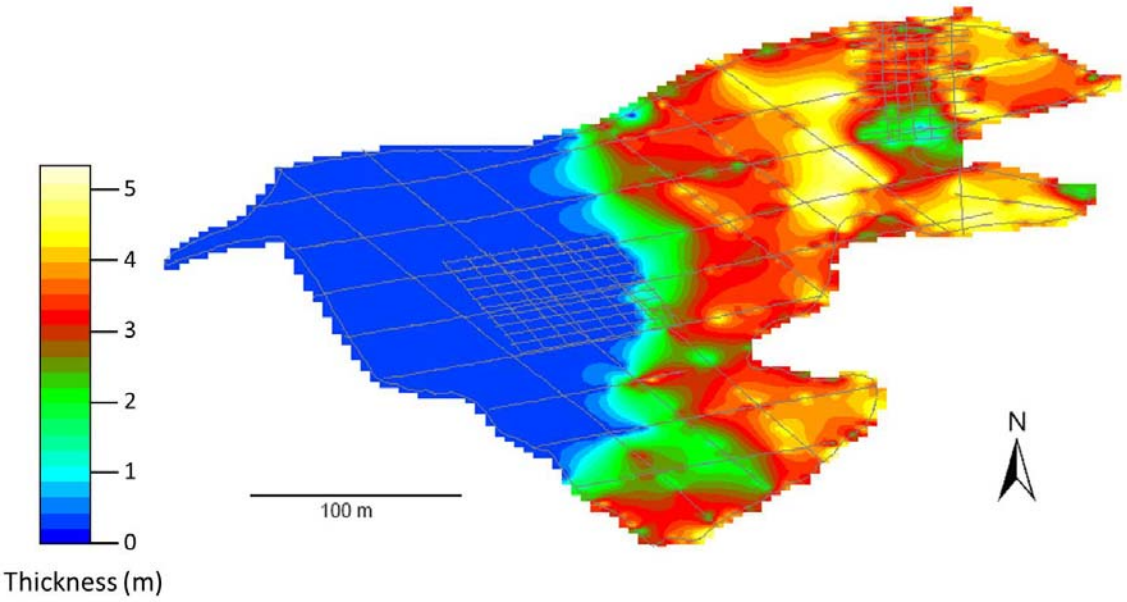

Figure 5.30. Isopach map of GPR Facies C in Sequence 4 (100 MHz data). GPR Facies C is the most dominant GPR facies in Sequence 4 and reaches a maximum thickness of approximately 5 m. Note the thickest portions of GPR Facies C occur in the central to eastern (downdip) part of the survey site.

CHAPTER 6: DISCUSSION

A fundamental challenge in applied sedimentology and stratigraphy is "predicting the anatomy of sedimentary rocks in the subsurface, in particular the distribution of porosity (and its derivative, permeability)" (Schlager, 2000). To address this important unknown, subsurface imaging techniques such as GPR have provided valuable insights into the 3D variability in stratigraphic architecture of both carbonate and siliciclastic successions. This study aimed to explore GPR's utility in examining the anatomy of a microbialite-oolite carbonate complex with a well-constrained depositional and diagenetic framework.

6.1: Interpretation of Relations between GPR Facies and Geology

GPR data collected in this study clearly illustrate that GPR facies cut across individual reflections and stratigraphy and show that they are not always directly or uniquely related to distinct depositional facies (Figures 5.7, 5.19). This lack of relation may be considered surprising given the successful imaging of sedimentologic features in other carbonate successions (Grasmuek and Weger, 2002; Nielson et al., 2004; Jorry and Bievre, 2011). Instead, in this Upper Miocene succession, changes in GPR facies correspond most closely to changes in porosity and porosity variability, which may or may not be related to depositional features (Figures 5.8, 5.10, 5.19). Instead, within the upper two sequences that were imaged within the TCC, porosity within the sequences is controlled by the complex inter-relations of both depositional and diagenetic history.

For example, trough cross-bedded ooid grainstone has marked variability in grain size, shape and sorting at several scales, from individual laminae to bed sets. Some of these variations likely are controlled by original, depositional processes (Rankey and

Reeder, 2011). The initial porosity can be enhanced or degraded by diagenetic processes as well (Cantrell and Walker, 1985; Evans and Ginsburg, 1987; Cantrell, 2006). These superimposed signatures lead to highly variable porosity within individual oolitic units, which may result in rock fabric bodies that cross-cut stratigraphy. High and variable porosity leads to numerous interfaces with marked dielectric contrasts, resulting in strong reflections in the GPR data (GPR Facies C), whereas lower and less variable porosity leads to weaker reflections (GPR Facies B).

In contrast, many of the tight thrombolite units have only small changes in porosity, resulting in very weak or absent reflections in the GPR data (GPR Facies A). Given the depositionally unstratified, mottled nature of thrombolites (Kennard and James, 1986; Planavsky and Ginsburg, 2009) and the small variation in porosity within these bodies, it is likely that tight thrombolites include few interfaces with contrast sufficient to cause significant internal reflections.

Nonetheless, the succession is not all pure carbonate, and this factor has an influence on the GPR signal, as suggested by the reflector corresponding to Sequence Boundary 3 (GPR Facies D). This strong, continuous reflector likely is caused by a large dielectric constant contrast related to a change in mineralogy across the interface between Sequence 3 into the upper portion of Sequence 2, where volcaniclastic minerals are concentrated. Additionally, weathering of the volcaniclastic minerals to clay minerals may cause the unit to retain moisture. Presence of water in this unit, even a small amount, would cause a significant reflection and rapid attenuation of the radar data due to increased electrical conductivity.

A less distinctive reflection that was fairly continuous in profiles of all frequencies was located at a depth of 0 m to 6 m. This reflection correlated well with Sequence Boundary 4 at the top of Sequence 3 on the outcrop, where a volcaniclastic-rich ooid grainstone caps the sequence. This reflection is likely not as well expressed as Sequence Boundary 3 for several reasons. First, this unit is much thinner than the volcaniclastic-rich ooid grainstone capping Sequence 2, however, with an average thickness of approximately 15 cm, half the thickness of the comparable unit that corresponds with the reflection representing Sequence Boundary 3. A second difference between this volcaniclastic-rich ooid grainstone and that at the top of Sequence 2 is that the capping unit is discontinuous. Together, the variable thickness and continuity are likely responsible for the highly variable and discontinuous nature of the GPR reflection representing Sequence Boundary 4.

An interesting finding is that the GPR facies are not distributed uniformly throughout the study area. For example, GPR Facies B is abundant and thick in the updip parts of the survey area, and less continuous and thinner downdip. Analysis of outcrop and thin section data reveal that updip areas, which have an abundance of GPR Facies B, typically have lower porosity than downdip areas. This change to lower overall porosity in updip areas is consistent with higher amounts of calcite cement that postdates TCC deposition in updip areas (Z. Li, personal communication). Thus, this large-scale trend of GPR facies distribution is interpreted to reflect primarily a diagenetic overprint. Evidence is that contacts between GPR Facies B and C commonly are subvertical in places linear, which is inconsistent with most depositional contacts, cut across sequence boundaries, and many reflectors are continuous across the facies boundaries.

Several other intriguing aspects of the GPR data warrant discussion. The first aspect concerns the nature and origin of the step-like morphology evident in the isopach of Sequence 3. The abrupt change in thickness in the central part of the survey site (Figure 5.21) may have formed from one of several different processes. One possibility is that the change in thickness observed in Sequence 3 may be a result of post-depositional erosional truncation following deposition of Sequence 3 but before deposition of Sequence 4. Based on Pleistocene and Holocene analogs, many erosional terraces are produced during sea-level rise (Blanchon and Jones, 1995). During slow sea-level rises or stillstands, wave energy and intertidal bio-eroders commonly truncate beds and form notches or step-like terraces (Sarg, 1988; Blanchon and Jones, 1995; Webster et al., 2009). Evidence consistent with this interpretation would include truncation of underlying beds at the change in thickness, a distinct flat-to-gently dipping surface with possible marine encrusters or borings, as well as coarse rubble and debris immediately downdip from the truncation. As it represents erosion of lithified strata, this rubble and debris likely would include a different diagenetic history than surrounding sediments as well. No evidence of these features is observed on outcrops (Lipinski, 2009) and GPR data include only ambiguous evidence for truncation, which cannot be correlated between adjacent GPR lines.

Alternatively, another possibility for the step-like morphology is that the change in thickness is constructional, related to depositional relief. If this were the cause, the succession might include evidence for offlapping patterns or shallow water facies and higher energy deposits passing abruptly downdip to lower energy, thinner deposits (e.g., Sarg, 1988; Hanford and Loucks, 1993; Schlager, 2005). Further support for a

constructional origin could include continuous evidence of subaerial exposure across paleotopography from updip areas to downdip areas. Although no unambiguous evidence of offlapping patterns or lateral facies changes are apparent on outcrops or in the GPR data, fenestral ooid grainstone caps Sequence 3 throughout the study area (Lipinski, 2009). This observation indicates that the sequence was not truncated.

The step-like geometry in Sequence 3 may be a result of a combination of different processes. As Lipinski (2009) demonstrated, deposition of sequences within the TCC was influenced by a complex interplay among sea level change, paleotopography, and less than optimal carbonate production. Nonetheless, in the absence of a higher resolution grid or data set, the details of the nature and origin of this geometry remain ambiguous. Furthermore, a more focused examination of the outcrop may provide insights into the origin of this thickness change and may prove to be useful for reconstruction of sea-level history of the Upper Miocene.

Although high-resolution data (0.31 m resolution in the 100 MHz data) successfully imaged small-scale variability in GPR facies changes throughout the survey area, some features visible on outcrop were not necessarily easily discernable on all profiles. For example, numerous fractures ranging from 0.1 to 1 cm are visible on the outcrops, but were difficult to trace away from the outcrop, even when GPR profiles were collected within 1 to 2 m from the outcrop. Some fractures observed on the outcrop were open (filled with air) and some were filled with calcite cement. Although the probability that air-filled fractures would be easier to detect than those filled with carbonate minerals that have similar dielectric properties as the surrounding units, GPR was unable to image them in this survey. Fractures, especially fractures with near-vertical orientations as those

found in the survey area, are difficult to detect on GPR profiles. Discontinuity analysis of multi-polarization and true 3D data with closely spaced inlines and crosslines can image fractures, however (Tsoflias et al., 2004; Grasmuek et al., 2004; Guidry et al., 2007). As fracture characterization was not the purpose of this study, true 3D data were not acquired, so the absence of imaging of fractures in these data does not imply their absence.

Nonetheless, fractures may influence GPR signatures indirectly. In the data, near-vertical transitions between GPR facies that appear to follow linear trends in some areas. Although many boundaries between GPR facies are inclined at 10 to 60 degrees (Figures 5.11, 5.19), many others are near-vertical (Figure 5.24). Mapping these near-vertical GPR facies changes between adjacent lines highlights linear to sub-linear trends, as is seen in the western (updip) portion of the survey area (Figures 5.22, 5.23). Although near-vertical boundaries associated with depositional facies are present in the study site (e.g. some thrombolite bodies are columnar in form and have near-vertical boundaries between them and adjacent ooid granistone) many of the near-vertical changes in GPR facies cannot be easily associated with depositional features for several reasons. A first reason relates to the thickness of the GPR facies changes. If the most pronounced boundaries (12 m high) were caused by a thrombolite-ooid grainstone facies transition, the thickness of the thrombolite would have to be nearly three times the thickness of thrombolite bodies observed on the outcrop, which reach a maximum thickness of only 4 m. A second line of evidence against a depositional origin of the abrupt, near-vertical changes in some GPR facies is that they appear to be traceable across numerous GPR lines that have a spacing of 20 m. Thus, thrombolite bodies would have to extend laterally for more

than 100 m, an attribute not observed on the outcrop. Third, these vertical facies changes are found in Sequence 3 in areas where outcrop shows thrombolite to be nearly absent. The height, lateral extent, calibration to outcrop, and overall morphologies of these near-vertical changes in some GPR facies suggest that they are more likely a result of post-depositional processes rather than depositional processes.

Broadly comparable linear features have been described in association with fractures and faults in other studies (e.g., Guidry et al., 2007). Fractures and faults have been shown to be an important control on fluid flow, and therefore, can strongly influence diagenetic alteration. There are no major faults in the survey area; one minor fault occurs in the area but it does not correspond to any of the near-vertical GPR facies changes. Numerous fractures cut the strata in the study area and may be responsible for the near-vertical, linear to sub-linear trends. The linear trends of near-vertical changes in GPR facies likely do not represent individual fractures, as these likely would not be evident on the 2D lines (cf. Guidry et al., 2007). Instead, the GPR facies boundaries may represent zones of diagenetic alteration related to fractures. A true 3D GPR survey (Grasmuek et al., 2004; Guidry et al., 2007) would be required to improve constraints on the nature and origin of these features.

Caves are another feature visible on outcrop that were not apparent in the GPR data. The perimeter of the survey area had small caves with lateral dimensions of 0.5 to 2 m with heights ranging up to 2 m. The majority of the caves extended less than 1.5 m into the interior of the survey area and decreased in size with increasing distance away from the outcrop face. It was expected that if caves were present in the interior of the survey area, that they would be evident in the GPR data. Analysis of the GPR data, however,

illustrate that no cavities or caves larger than 30 cm (smallest size feature that can be resolved with highest frequency antennas, 100 MHz) are present in the interior of the survey area. Specifically, the data showed no prominent diffraction hyperbolas, a common result when GPR signals pass through air-filled voids (Sigurdsson and Overgaard, 1998). The lack of diffraction hyperbolas suggests that the survey area contains only small-scale cavities, with dimensions below the resolution of the data.

6.2: Implications

Over the past several decades, numerous studies have demonstrated the usefulness of GPR as a tool for imaging stratigraphic features in a multitude of depositional environments, ranging from eolian to marine, carbonate to siliciclastic systems (McMechan et al., 1998; Jol et al., 2003; Hugenholtz et al., 2007; Jorry and Bievre, 2011). Studies in carbonate successions have focused on imaging stratigraphic features at several scales, from thick, relatively homogenous carbonate packages (Pratt and Maill, 1993; Liner and Liner, 1995), to complex, heterogeneous carbonate sequences (Dagallier et al., 2000; Grasmuek et al., 2004; Neal et al., 2008; Aspiron et al., 2009; Jorry and Bievre, 2011). Although these studies exemplify the wide range of applications of GPR in carbonate strata, the utility of GPR to image changes in porosity and diagenetic variability has not been emphasized.

Although this study demonstrates that some GPR signatures are closely related to depositional features, it is variations in porosity, both depositional and diagenetic in origin, that form the dominant influence on reflection characteristics in this succession.

Most GPR facies transitions correlate more closely with variations in porosity than with depositional facies and features, showing that GPR imaging can be markedly influenced by diagenetic complexity. For example, the contacts between GPR Facies B and C commonly cut across Sequence Boundary 4 (Figures 21, 25, 33) and may represent any of the major depositional facies (ooid grainstone, thrombolite or stromatolite) in the survey area. Some reflectors are continuous across these contacts. The cross-cutting relationships between GPR facies and depositional features provide evidence of diagenetic influence.

Large-scale patterns of distribution of GPR facies provide further evidence of diagenetic overprinting evident in GPR data. For example, GPR Facies B is most continuous and thickest in the updip part of the survey area, whereas extent of this facies is patchier and less thick downdip. Examination of outcrop and thin sections reveals that the depositional facies in updip areas have lower porosity resulting from more calcite cementation, as discussed above. Dissertation research focusing on the diagenetic history of La Molata by Zhaoqi Li also provides evidence for overall lower porosity and greater amounts of calcite cement updip compared to downdip areas.

In sum, these results show that at least in some successions GPR represents an underappreciated, but potentially powerful, tool for mapping diagenetic overprinting and complexity in carbonate strata as suggested by Franseen et al. (2007).

These types of insights on spatial changes in porosity can be valuable analogs for understanding, predicting, and modeling variability in the subsurface. Construction of subsurface reservoir models requires assigning properties (facies, porosity) away from known points such as wells (Knight et al., 1997; Lipinski, 2009). Commonly, spatial

variability is constrained by wells, which may be tens to hundreds (or even more) of meters apart. As revealed in this study, there is marked variability at a much finer scale that could be used as input for a reservoir model.

Similarly, reservoir models are developed by defining sequences and surfaces from well or seismic data. Within this framework, facies probabilities are used to distribute depositional facies, each of which include a predefined range of petrophysical properties (porosity and permeability). The properties at any given point are sampled by various methods from the overall population of petrophysical property values. The GPR data collected for this study directly image the petrophysical properties that are utilized in reservoir modeling (changes in porosity). As such, utilizing the trends in these types of data allow the removal of the intermediate step of assigning lithofacies, thereby reducing uncertainty.

If these strata formed part of a subsurface reservoir, the distribution of high quality reservoir bodies (porous units) would likely be more variable than a simple, layered stratigraphic model might imply. For instance, the observation that GPR facies readily cross-cut sequence boundaries indicates that sequence boundaries likely would not influence fluid flow through the system. At the largest scale, downdip areas that have porous grainstone and vuggy thrombolite boundstone units would likely be better reservoir flow units than the lower porosity units found updip. At a finer scale, dense thrombolite boundstone units and low porosity ooid grainstone bodies could form baffles or even barriers to flow, whereas vuggy thrombolite boundstone and porous ooid grainstone would likely form flow units. Nonetheless, individual boundaries are not constrained by stratigraphy or layering, but instead appear to be strongly influenced by a

complex diagenetic overprinting. High-resolution studies such as this can provide data and conceptual models for understanding and effectively exploiting analogous subsurface heterogeneous reservoirs.

CHAPTER 7: SUMMARY AND CONCLUSIONS

GPR data of differing frequencies were acquired in 2D and 3D to provide characterization of the stratigraphic architecture of two sequences in an Upper Miocene microbialite-oolite carbonate reservoir analog. GPR reflections and facies correlate to variations in stratigraphy and porosity evident through calibration to well-documented, adjacent outcrops.

Lower-frequency data (25 and 50 MHz) are useful in identifying large-scale features, such as sequence boundaries and large-scale variations in porosity. The lower frequency data imaged the upper two sequences to a maximum depth of approximately 12 m, where a volcaniclastic-rich ooid grainstone unit attenuates the signal. Higher frequency data (100 MHz) resolve finer-scale lithofacies geometries and porosity changes within and among sequences; some GPR facies cross-cut sequence boundaries. The 100 MHz data imaged to a depth of approximately 6 m. Integration of data of different frequencies allows recognition of heterogeneity at multiple scales.

Results of this study illustrate that although GPR can image stratigraphic features such as sequence boundaries and tight thrombolite bodies, reflections are primarily influenced by porosity variations within the strata. Three of the GPR facies, recognized on the basis of reflection signatures (strong, weak, or no internal reflections), are linked

predominantly to porosity variations in facies. Each GPR facies has been identified and delineated in each frequency data set.

A large-scale trend, observable in GPR data of all frequencies, was that GPR Facies B, which correlates to units of intermediate porosity, was most dominant in the western (updip) portion of the survey area. This finding is in agreement with other research that shows updip units have overall lower porosity and a greater amount of calcite cement than downdip units, suggesting a diagenetic control on porosity and GPR facies distribution. Furthermore, in many instances, GPR facies cut across individual reflections and sequence boundaries. Additionally, boundaries between GPR facies B and C are commonly near-vertical and define linear trends in map view, suggesting the influence of fractures. These results indicate that GPR data captured porosity characteristics associated with both depositional and post-depositional processes. Although GPR has traditionally been used to image stratigraphic features, this study indicates GPR can image diagenetic features as well. As such, GPR can be a valuable tool for imaging porosity heterogeneity and developing conceptual models that portray 3D variations in stratigraphy and porosity. Resultant insights may be important for comprehensive understanding of porosity development and distribution in this system and subsurface carbonate reservoir analogs.

CHAPTER 8: RECOMMENDATIONS FOR FUTURE WORK

One suggestion for the design of a future survey that would likely be more successful at capturing complex GPR facies geometries and distribution is one in which GPR profiles are collected in a more densely spaced grid (at least 5 m by 5 m line

spacing) covering the entire survey area. A main goal of this study was to image heterogeneity, both depositional and diagenetic, throughout the TCC. The two 3D grids clearly illustrate that a grid spacing of 20 m was insufficient to capture the rapidly changing geometries and distribution of GPR facies. The 3D grids with 5 m by 5 m line spacing were much more effective at capturing abrupt changes in geometries of GPR facies, elucidating their complex distributions. Data from the 3D grids suggest that abrupt changes in geometries of GPR facies may occur throughout the entire survey area, however, the 20 m by 20 m line spacing of the 2D grid was unable to fully capture such variation. Therefore, a future study with more closely spaced lines would likely image the variability and changing geometries of GPR facies more effectively. Of particular interest would be a dense 3D grid located over the area in which an abrupt change in thickness occurs in Sequence 3. Closely spaced lines from this area may provide evidence useful for determining the origin of the thickness change.

Another suggestion to better constrain relations between GPR signatures and depositional facies would be collection of more closely spaced rock samples. A denser sampling may allow more accurate quantification of porosity and variations in porosity that could be quantitatively correlated to magnitude of reflection amplitude.

An additional approach to investigate the role of porosity variation on GPR signals could be to image other areas with similar depositional and diagenetic histories but more simple successions, such as ones composed almost entirely of either oolite or microbialite units, to test whether or not the GPR response was just as complex. This approach would likely contribute to a better understanding of factors influencing GPR signatures.

Successfully imaging all four sequences of the TCC might require a different geophysical approach. An unanticipated outcome of this survey was the severe attenuation of GPR signal as EM waves encountered the volcaniclastic-rich ooid grainstone layer at the base of Sequence 3 (depth of approximately 12 m). Although this unit was known prior to conducting the survey, the influence it had on the radar data was unexpected. One way to image below this unit would be to conduct a near-surface seismic survey over the area. Acoustic waves would likely not attenuate as rapidly when they encounter the electrically conductive unit. Depending on the survey design, a high-resolution seismic survey would be capable of resolving meter-scale features to a depth of 50 m.

REFERENCES

Annan, A.P., 2005, Ground-Penetrating Radar: *in* Butler, D.K., ed., Near Surface Geophysics: Society of Exploration Geophysicists Investigations in Geophysics 13, p. 357-438.

Aspiron, U. and Aigner, T., 2000, An initial attempt to map carbonate buildups using ground-penetrating radar: an example from the Upper Jurassic of SW Germany: Facies, v. 42, p. 245-252.

Aspiron, U., Westphal, H., Nieman, M. and Pomar, L., 2009, Extrapolation of depositional geometries of the Menorcan Miocene carbonate ramp with ground-penetrating radar: Facies, v. 55, p. 37-46.

Berkhout, A.J., 1984, Seismic resolution: A quantitative analysis of resolving power of acoustical echo techniques: Geophysical Press, London and Amsterdam, Netherlands, 228 p.

Blanchon, P. and Jones, B., 1995, Marine-planation terraces on the shelf around Grand Cayman: A result of stepped Holocene sea-level rise: Journal of Coastal Research, v. 11, p. 1-33.

Brachert, T.C., Betzler, C., Braga, J.C. and Martin, J.M., 1998, Microtaphofacies of a Warm-Temperate Carbonate Ramp (Uppermost Tortonian/Lowermost Messinian, Southern Spain): Palaios, v. 13, p. 459-475.

Braga, J.C., Martin, J.M. and Riding, R., 1995, Controls on Microbial Dome Fabric Development along a Carbonate-Siliciclastic Shelf-Basin Transect, Miocene, SE Spain: Palaios, v. 10, p. 347-361.

Bristow, C.S. and Jol, H.L., 2003, An introduction to ground-penetrating radar (GPR) in sediments: *in* Bristow, C.S. and Jol, H.M., eds., Ground-Penetrating Radar in Sediments, Geological Society of London Special Publication 211, p. 1-7.

Bristow, C.S., Chroston, P.N. and Bailey, S.D., 2000, The structure and development of foredunes on a locally prograding coast: insights from ground-penetrating radar surveys, Norfolk, UK: Sedimentology, v. 47, p. 923-944.

Bristow, C.S., Jones, B.G., Nanson, G.C., Hollands, C., Coleman, M. and Price, D.M., 2007, GPR surveys of vegetated linear dune stratigraphy in central Australia: Evidence for linear dune extension with vertical and lateral accretion: *in* Baker, G.S. and Jol, H.M, eds., Stratigraphic Analyses Using GPR, Geological Society of America Special Paper 432, p. 19-34.

Bristow, C., 2009, Ground penetrating radar in aeolian dune sands: *in* Jol, H.M., ed., Ground Penetrating Radar: Theory and Applications, Elsevier, Oxford, UK. p. 274-294.

Budd, D.A., Pranter, M.J. and Zulfiquar, R., 2006, Lateral periodic variations in the petrophysical and geochemical properties of dolomites: Geology, v. 34, p. 373-376.

Cantrell, D.L., 2006, Cortical fabrics of Upper Jurassic ooids, Arab Formation, Saudi Arabia: Implications for original carbonate mineralogy: Sedimentary Geology, v. 186, p. 157-170.

Cantrell, D.L. and Walker, K.R., 1985, Depositional and diagenetic patterns, ancient oolite middle Ordovician, Eastern Tennessee: Journal of Sedimentary Petrology, v. 55, p. 0518-0531.

Corbeanu, R.M., Soegaard, K., Szerbiak, R.B., Thurmond, J.B., McMechan, G.A., Wang, D., Snelgrove, S., Forster, C.B. and Menitove, A., 2001, Detailed internal architecture of a fluvial channel sandstone determined from outcrop, cores, and 3-D ground-penetrating radar: Example from the

Middle Cretacious Ferron Sandstone, East-Central Utah: American Association of Petroleum Geologists Bulletin, v. 85, p. 1583-1608.

Dabrio, C.J., Esteban, M., and Martin, J.M., 1981, The Coral Reef of Nijar, Messinian (Uppermost Miocene), Almeria Province, SE Spain: Journal of Sedimentary Petrology, v. 51, p. 521-439.

Dagallier, G., Laitinen, A.I., Malartre, F., Van Campenhout, I.P.A.M., and Veeken, P.C.H., 2000, Ground penetrating radar application in a shallow marine Oxfordian limestone sequence located on the eastern flank of the Paris Basin, NE France: Sedimentary Geology, v. 130, p. 149-165.

Daniels, D.J., 1996, Surface-penetrating radar: Electronics and Communication Engineering Journal, v. 8, p. 165-182.

Davis, J.L. and Annan, A.P., 1989, Ground-penetrating radar for high-resolution mapping of soil and rock stratigraphy: Geophysical Prospecting, v. 37, p. 531-551.

Dronkert, H., 1976, Late Miocene Evaporites in the Sorbas Basin and Adjoining Areas: Memorie della Societa Geologica Italiana, v. 16, p. 341-361.

Esteban, M., 1979, Significance of the Upper Miocene Coral Reefs of the Western Mediterranean: Palaeogeography, Palaeoclimatology, Palaeoecology, v. 29, p. 169-188.

Esteban, M., 1996, An overview of Miocene reefs from the Mediterranean area: General trends and facies models: *in* Franseen, E.K., Esteban, M., Ward, W.C. and Rouchy, J.-M., eds., Models for Carbonate Stratigraphy from Miocene Reef Complexes of the Mediterranean Regions: SEPM Concepts in Sedimentology and Paleontology Series 5, p. 3-54.

Esteban, M. and Giner, J., 1980, Messinian coral reefs and erosion surfaces in Cabo de Gata (Almeria, SE Spain): Acta Geologica Hispanica, v. 15, p. 97-104.

Evans, C.C. and Ginsburg, R.N., 1987, Fabric-selective diagenesis in the late Pleistocene Miami Limestone: Journal of Sedimentary Research, v. 57, p. 311-318.

Franseen, E.K., 1989, Depositional sequences and correlation of middle to upper Miocene carbonate complexes, Las Negras area, southeastern Spain, PhD Thesis, University of Wisconsin-Madison, Madison, WI, 374 p.

Franseen, E.K. and Mankiewicz, C., 1991, Depositional sequences and correlation of middle(?) to late Miocene carbonate complexes, Las Negras and Nijar areas, southeastern Spain: Sedimentology, v. 38, p. 871-898.

Franseen, E.K., Goldstein, R.H. and Whitesell, T.E., 1993, Sequence stratigraphy of Miocene carbonate complexes, Las Negras area, southeastern Spain: implications for quantification of changes in relative sea-level: *in* Loucks, R.G., and Sarg, J.F., eds., Carbonate Sequence Stratigraphy: Recent Developments and Applications, AAPG Memoir 57, p. 409-434.

Franseen, E.K. and Goldstein, R.H., 1996, Paleoslope, Sea-level and climate controls on Upper Miocene platform evolution, Las Negras area, Southeastern Spain: *in* Franseen, E.K., Esteban, M., Ward, W. C., and Rouchy, J.-M., eds., Models for Carbonate Stratigraphy from Miocene Reef Complexes of Mediterranean Regions, SEPM Concepts in Sedimentology and Paleontology Series 5, p. 159-176.

Franseen, E.K., Goldstein, R.H. and Farr, M.R., 1997, Substrate-slope and temperature controls on carbonate ramps: Revelations from Upper Miocene Outcrops, SE Spain: *in* James, N.P. and Clarke, A.D., eds., Cool-Water Carbonates, SEPM Special Publication 56, p. 271-290.

Franseen, E.K., Goldstein, R.H., and Farr, M.R., 1998, Quantitative controls on location and architecture of carbonate depositional sequences: Upper Miocene, Cabo de Gata, SE Spain: Journal of Sedimentary Research, v. 68, p. 283-298.

Franseen, E.K. and Goldstein, R.H., 2004, Build-and-fill sequences: Predictable patterns of creation and destruction of paleotopography in small-scale sequences: AAPG Search and Discovery Article #90026.

Franseen, E.K., Byrnes, A.P., Xia, J., and Miller, R.D, 2007a, Improving resolution and understanding controls on GPR response in carbonate strata: Implications for attribute analysis: The Leading Edge, v. 26, p. 984-993.

Franseen, E.K., Goldstein, R.H., and Minzoni, M., 2007b, Build-and-fill sequences in carbonate systems – An emerging picture: AAPG AAPG Search and Discover Article #90063

Franseen, E.K., Goldstein, R.H. and Esteban, M., 2010, Controls on porosity types and distribution in carbonate reservoirs: A guidebook for Miocene carbonate complexes of the Cabo de Gata area, SE Spain: American Association of Petroleum Geologists Education Program, p. 271-290.

Goldstein, R.H. and Franseen, E.K., 1995, Pinning points: a method providing quantitative constraints on relative sea-level history: Sedimentary Geology, v. 95, p. 1-10.

Grasmueck, M. and Weger, R., 2002, 3D GPR reveals complex internal structure of Pleistocene oolitic sandbar: The Leading Edge, v. 21, p. 634-639.

Grasmueck, M., Weger, R. and Horstmeyer, H., 2004, Three-dimensional ground-penetrating radar imaging of sedimentary structures, fractures, and archaeological features at submeter resolution: Geology, v. 32, p. 933-936.

Greaves, R.J., Lesmes, D.P., Lee, J.M. and Toksoz, M.N., 1996, Velocity variations and water content estimated from multi-offset, ground penetrating radar: Geophysics, v. 61, p. 683-695.

Guidry, S.A., Grasmeuck, M., Carpenter, D.G., Gombos., A.M., Bachtel, S.L. and Viggiano, D.A., 2007, Karst and early fracture networks in carbonates, Turks and Caicos Islands, British West Indies: Journal of Sedimentary Research, v. 77, p. 508-524.

Hanford, C.R. and Loucks, R.G., 1993, Carbonate depositional sequences and systems tracts; Responses of carbonate platforms to relative sea-level changes: *in* Loucks, R.G., and Sarg, J.F., eds., Carbonate Sequence Stratigraphy: Recent Developments and Applications, AAPG Memoir 57, p. 3-41.

Hickin, A.S., Bobrowsky, P.T., Paulen, R.C. and Best, M., 2007, Imaging fluvial architecture within a paleovalley fill using ground penetrating radar, Maple Creek, Guyana: *in* Baker, G.S. and Jol, H.M, eds., Stratigraphic Analyses Using GPR, Geological Society of America Special Paper 432, p. 133-154.

Hugenholtz, C.H., Moorman, B.J. and Wolfe, S.A., 2007, Ground penetrating radar (GPR) imaging of the internal structure of an active parabolic sand dune: *in* Baker, G.S. and Jol, H.M, eds., Stratigraphic Analyses Using GPR, Geological Society of America Special Paper 432, p. 35-46.

James, N.P., 1997, The cool-water carbonate depositional realm: *in* James, N.P. and Clarke, J.A.D., eds., Cool-water carbonates: SEPM Special Publication 56, p. 1-20.

Johnson, C.L., Franseen, E.K. and Goldstein, R.H, 2005, The effects of relative sea level and paleotopography on lithofacies distribution and geometries in heterozoan carbonates, Southeastern Spain: Sedimentology, v. 52, p. 513-536.

Jol, H.M., Lawton, D.C. and Smith, D.G., 2003, Ground penetrating radar: 2-D and 3-D subsurface imaging of a coastal barrier spit, Long Beach, WA, USA: Geomorphology, v. 53, p. 165-181.

Jorry, S.J. and Bievre, G., 2011, Integration of sedimentology and ground-penetrating radar for high-resolution imaging of a carbonate platform: Sedimentology, v. 58 (in press).

Kennard, J.M. and James, N.P., 1986, Thrombolites and stromatolites: Two distinct types of microbial structures: Palaios, v. 1, p. 492-503.

Knight, R., Tercier, P. and Jol, H., 1997, The role of ground penetrating radar and geostatisics in reservoir description: The Leading Edge, v. 16, p. 1576-1582.

Lipinski, C.J., 2009, Stratigraphy of Upper Miocene oolite-microbialite-coralgal reef sequences of the Terminal Carbonate Complex: Southeast Spain: Unpublished MS Thesis, University of Kansas Department of Geology, 116 p.

Liner, C.L. and Liner, M.L., 1995, Ground-penetrating radar- A near-face experience from Washington County, Arkansas: The Leading Edge, v. 14, p. 17-21.

Lines, L.R. and Newrick, R.T., 2004, Fundamentals of Geophysical Interpretation: Society of Exploration Geophysicists, Geophysical Monograph Series 13, 274 p.

Lopez-Ruiz, J. and Rodriguez-Badiola, E., 1980 La Region Volcanica Neogena del Sureste de Espana: Estudios Geologicos, v. 36, p. 5-63.

Martin, J.M., Braga, J.C. and Betzler, C., 2003, Late Neogene - Recent uplift of the Cabo de Gata volcanic province, Almeria, SE Spain: Geomorphology, v. 50, p. 27-42.

Martin, J.M. and Braga, J.C., 1994, Messinian events in the Sorbas Basin in southeastern Spain and their implications in the recent history of the Mediterranean: Sedimentary Geology, v. 90, p. 257-268.

Martinez, A. and Byrnes, A.P., 2001, Modeling dielectric-constant values of geologic materials-An aid to ground-penetrating radar data collection and interpretation: *in* Current Research in Earth Sciences: Kansas Geological Survey Bulletin 247, part 1. P. 1-16.

Martinez, A., Kruger, J.M. and Franseen, E.K., 1998, Utility of using ground-penetrating radar in near-surface, high-resolution imaging of Lansing-Kansas City (Pennsylvanian) Limestone reservoir analogs: Current Research in Earth Sciences, Kansas Geological Survey Bulletin 241, p. 43-59.

McMechan, G.A., Loucks, R.G., Zeng, X. and Mescher, P., 1998, Ground penetrating radar imaging of a collapsed paleocave system in the Ellenburger dolomite, central Texas: Journal of Applied Geophysics, v. 39, p. 1-10.

Montadert, L., Roberts, D.G., Auffret, G.A., Bock, W., DuPueble, P.A., Hailwood, E.A., Harrison, W., Letouzey, J. and Mauffret, A., 1978, Messinian events: seismic evidence: *in* Hsu, K.J. and Montadert, L., eds., Initial Reports of the Deep Sea Drilling: US Government Printing Office, Washington, v. 42, p. 1037-1050.

Montenant, C., Ott D'estevou, P. and Masse, P., 1987, Tectonic-sedimentary characters of the Betic Neogene basins evolving in a crustal transcurrent shear zone (SE Spain), Bulletin Du Centre De Recherches Elf Exploration Production Elf-Aquitaine, v. 11, p. 1-22.

Montenant, C. and Ott D' Estevou, P., 1990, Le basin de Nijar-Carboneras et le couloir de Bas-Andarax, *in* Montenant, C., ed., Les Bassins Neogenes Du Domaine Betique Oriental (Espagne): Institut Geologique Albert-de-Lapparent, Paris, Documents et Travaux Institut Geologique Albert-de-Lapparent, p. 129-164.

Neal, A., 2004, Ground-penetrating radar and its use in sedimentology: principles, problems and progress: Earth-Science Reviews, v. 66, p. 261-330.

Neal, A., Grasmueck, M., McNeill, D.F., Viggiano, D.A. and Eberli, G.P., 2008, Full-resolution 3D radar stratigraphy of complex oolitic sedimentary architecture: Miami Limestone, Florida, USA: Journal of Sedimentary Research, v. 78, p. 638-653.

Nielson, L., Boldreel, L.O. and Surlyk, F., 2004, Ground-penetrating radar imaging of carbonate mound structures and implications for interpretation of marine seismic strata: American Association of Petroleum Geologists Bulletin, v. 88, p. 1069-1082.

Pratt, B.R. and Miall, A.D., 1993, Anatomy of a bioclastic grainstone megashoal (Middle Silurian, southern Ontario) revealed by ground-penetrating radar: Geology, v. 21, p. 223-226.

Pranter, M.J., Zulfiquar, R. and Budd, D.A., 2006, Reservoir-scale characterization and multiphase fluid-flow modeling of lateral petrophysical heterogeneity within dolomite facies of the Madison Formation, Sheep Canyon and Lysite Mountain, Wyoming, U.S.A.: Petroleum Geoscience, v. 12, p. 29-40.

Rankey, G.C. and Reeder, S.L., 2011, Holocene oolitic marine sand complexes of the Bahamas: Journal of Sedimentary Research, v. 81, p. 97-117.

Reicherter, K.R. and Reiss, S., 2001, The Carboneras Fault Zone (southeastern Spain) revisited with Ground Penetrating Radar – Quaternary structural styles from high-resolution images: Netherlands Journal of Geosciences, v. 80, p. 129-138.

Rehault, J.P., Boillot, G. and Mauffret, A., 1985, The western Mediterranean basin: *in* Stanley, D.J. and Wezel, F.C., eds., Geologic Evolution of the Mediterranean Basin, Springer-Verlag, New York, p. 101-130.

Riding, R., Martin, J.M. and Braga, J.C., 1991, Coral-stromatolite reef framework, Upper Miocene, Almeria, Spain: Sedimentology, v. 38, p. 799-818.

Roberts, M.C., Niller, H.-P. and Helmstetter, N., 2003, Sedimentary architecture and radar facies of a fan delta, Cypress Creek, West Vancouver, British Columbia: *in* Bristow, C.S. and Jol, H.M., eds., Ground-Penetrating Radar in Sediments, Geological Society of London Special Publication 211, p. 111-126.

Rother, H., Jol, H.M. and Shulmeister, J., 2007, Stratigraphy and tectonic implications of late Pleistocene valley fill in the Hope Valley, Canterbury, South Island, New Zealand: *in* Baker, G.S. and Jol, H.M, eds., Stratigraphic Analyses Using GPR, Geological Society of America Special Paper 432, p. 155-168.

Rouchy, J.-M. and Saint Martin, J.-P., 1992, Late Miocene events in the Mediterranean as recorded by carbonate-evaporite relations: Geology, v. 20, p. 629-632.

Rust, A.C. and Russell, J.K., 2001, Mapping porosity variation in a welded pyroclastic deposit with signal and velocity patterns from ground-penetrating radar surveys: Bulletin of Volcanology, v. 62, p. 457-463.

Rytuba, J.J., Arribas, A., Jr., Cunningham, C.G., McKee, E.H., Podwysocki, M.H., Smith, J.G., Kelly, W.C. and Arribas, A., Sr., 1990, Mineralized and unmineralized calderas in Spain; Part II, Evolution of the Rodalquilar caldera complex and associated gold-allunite deposits: Mineralium Deposita, v. 25, p. S29-S35.

Sanz de Galdeano, C. and Vera, J.A., 1992, Stratigraphic record and palaeogeographical context of the Neogene basins in the Betic Cordillera, Spain: Basins Research, v. 4, p. 21-36.

Sarg, J. F., 1988, Carbonate sequence stratigraphy: *in* Wilgus, C., Ross, C.A. and Posamentier, H., eds., Sea-Level Changes: An Integrated Approach, SEPM Special Publication 42, p.155-181.

Schlager, W., 2000, The future of applied sedimentary geology: Journal of Sedimentary Research, v. 70, p. 2-9.

Schlager, W., 2005, Carbonate Sedimentology and Sequence Stratigraphy: SEPM Concepts in Sedimentology and Paleontology, v. 8, 200 p.

Sensors and Software, 2006, pulseEKKO PRO, User's Guide: Mississauga Ontario, Sensors and Software Inc., 161 p.

Serrano, F., 1992, Biostratigraphic control of Neogene volcanism in Sierra De Gata (southeast Spain): Geologie en Mijnbouw, v. 71, p. 3-14.

Sheriff, R.E., 1997, Seismic resolution a key element: American Association of Petroleum Geologists Search and Discovery Article #40036.

Shen, L.C., 1985, A laboratory technique for measuring dielectric properties of core samples at ultrahigh frequencies: Society of Petroleum Engineering Journal, v. 25, p. 502-511.

Shen, L.C., Savre, W.C., Price, J.M. and Athavale, K., 1985, Dielectric properties of reservoir rocks at ultrahigh frequencies: Geophysics, v. 50, p. 692-704.

Sigurdsson, T. and Overgaard, T., 1998, Application of GPR for 3-D visualization of geological and structural variation in a limestone formation: Journal of Applied Geophysics, v. 40, p. 29-36.

Stevens, C.W. and Robinson, S.D., 2007, The internal structure of relict lacustrine deltas, northern New York: *in* Baker, G.S. and Jol, H.M, eds., Stratigraphic Analyses Using GPR, Geological Society of America Special Paper 432, p. 93-102.

Trimble Users Guide, 2010, R8 GNSS, R6, 5800 User Guide, version 4.00, Revision A, http://trl.trimble.com/docushare/dsweb/Get/Document-449956/R8-R6-5800Receivers_4A_UG_7440.pdf

Tsoflias, G.P., Van Gestel, J-P., Stoffa, P.L., Blankenship, D.D. and Sen, M., 2004, Vertical fracture detection by exploiting the polarization properties of ground-penetrating radar signals: Geophysics, v. 69, p. 803-810.

Van den Bril, K., Gregoire, C., Swennen, R. and Lambot, S., 2007, Ground-penetrating radar as a tool to detect rock heterogeneities (channels, cemented layers and fractures) in the Luxembourg Sandstone Formation (Grand-Duchy of Luxembourg): Sedimentology, v. 54, p. 949-967.

Watney, W.L., 1980, Cyclic sedimentation of the Lansing and Kansas City groups (Missourian) in northwestern Kansas and southwestern Nebraska- A guide for petroleum exploration: Kansas Geological Survey Bulletin 220, 72 p.

Webster, J.M., Braga, J.C., Clague, D.A., Gallup, C., Hein, J.R., Potts, D.C., Renema, W., Riding, R., Riker-Coleman, K., Silver, E. and Wallace, L.M., 2009, Coral reef evolution on rapidly subsiding margins: Global and Planetary Change, v. 66, p. 129-148.

Whitesell, T.C., 1995, Diagenetic features associated with sequence boundaries in Upper Miocene carbonate strata, Las Negras, Spain: Unpublished MS Thesis, University of Kansas Department of Geology, 292 p.

Yilmaz, O., 2001, Seismic data analysis: Processing, inversion, and interpretation of seismic data: Society of Exploration Geophysicists Investigations in Geophysics 10, 2027 p.

Zeng, X., McMechan, G.A., Bhattacharya, J.P, Aiken, C.L.V., Xu, X., Hammon, W.S, III. and Corbeanu, R.M., 2004, 3D imaging of a reservoir analogue in point bar deposits in the Ferron Sandstone, Utah, using ground-penetrating radar: Geophysical Prospecting, v. 52, p. 151-163.